UNIVERSITÀ DEGLI STUDI DI TRENTO

Department of Physics

PhD in Physics

Experimental investigation of CO_2 valorization by plasma discharges

Supervisor:
Prof. Luca Matteo Martini

Co-supervisor:
Prof. Paolo Tosi

Author:
Sara Quercetti

XXXVI PhD cycle

Contents

Chapter 1

Introduction

1.1 Global warming

We are nowadays getting used to news reports stating that each passing month has been the warmest on record, and to extreme weather events that have now become nearly quotidian occurrences. The acceleration of global warming represents one of the most critical challenges humanity is facing in the 21st century.

Since the dawn of the Industrial Revolution, the intensive exploitation of fossil fuels has led to an unprecedented increase in atmospheric greenhouse gas (GHGs) concentrations, particularly carbon dioxide (CO_2). Analysis of ancient air bubbles trapped in ice cores reveals that CO_2 levels naturally oscillated between approximately 200 parts per million (ppm) during ice ages and 280 ppm during interglacial periods, while current measurements show a dramatic departure from this historical pattern. In 2023, atmospheric CO_2 concentrations had surpassed 420 ppm [1], marking an increase of nearly 50% from pre-industrial levels (see fig. 1.1).

This sharp rise in atmospheric CO_2 is primarily attributable to anthropogenic activities, particularly the combustion of fossil fuels. The Intergovernmental Panel on Climate Change (IPCC) has concluded with more than 95% certainty that human activities have been the dominant cause of observed warming over the past five decades [2]. The rate of increase is particularly alarming, being approximately 100 times faster than natural fluctuations observed over past geological eras.

The mechanism behind global warming involves the greenhouse effect: GHGs like CO_2 absorb infrared radiation emitted by Earth's surface and re-emit it in all directions, effectively trapping heat within the atmosphere. While this effect is essential for maintaining Earth's habitable average tem-

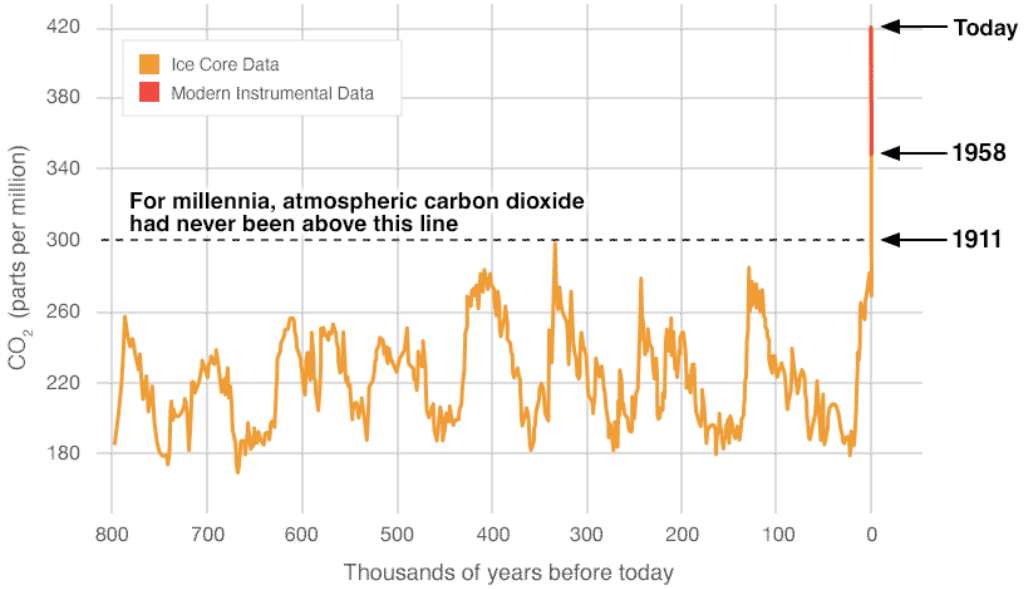

Figure 1.1: CO_2 concentration in the atmosphere in the last millennia. Figure reported from [1].

perature of approximately 14°C (without it, the average temperature would be around -6°C), the current unprecedented rate of increase in greenhouse gas concentrations is causing a positive radiative forcing that continues to enhance global temperatures.

The greenhouse effect involves multiple GHGs beyond CO_2, which is the primary contributor, responsible for about two-thirds of the total radiative forcing. Water vapor represents the most abundant greenhouse gas and plays a dominant role in the natural greenhouse effect. However, its impact on anthropogenic global warming is limited. This is due to its short atmospheric residence time of approximately 9 days, as it participates in a rapid hydrological cycle between the Earth's surface, oceans, and atmosphere, maintaining a relatively stable average concentration. In contrast, methane (CH_4) exhibits increasing atmospheric concentrations due to human activities. Despite its relatively low concentration of 1.8 ppm, CH_4 demonstrates remarkable infrared absorption efficiency, approximately 23 times greater than that of CO_2, making it a potent greenhouse gas. Its atmospheric lifetime of approximately 12 years, however, is considerably shorter than the effective residence time of excess CO_2.

The dynamics of CO_2 in the atmosphere present a more complex scenario. While individual CO_2 molecules have an atmospheric lifetime of roughly 5 years, this metric is misleading when considering anthropogenic emissions.

When a CO_2 molecule leaves the atmosphere, it typically undergoes exchange with oceanic carbon pools rather than being permanently removed from the system. Consequently, the elimination of excess anthropogenic CO_2 from the atmosphere-ocean system operates on centennial timescales, making its accumulation particularly problematic for climate dynamics [3]. Nitrous oxide (N_2O) and chlorofluorocarbons (CFCs) are additional significant contributors to the greenhouse effect, which are increasing due to human activities.

The consequences of this warming are already visible and concerning. Glaciers are melting at an alarming rate, threatening precious freshwater reserves. Sea levels are rising, putting coastal communities at risk. Furthermore, due to the significant heat capacity of oceans and various feedback mechanisms, the full impact of current emissions may not be fully realized for years or decades to come. The Earth's temperature has already increased by 1.1°C since the pre-industrial age, and even in an immediate zero-emission scenario, an additional warming of at least 0.5°C is expected in the next decades due to the system's thermal inertia.

Projections based on current GHG emission scenarios suggest a minimum increase in mean global surface temperature of 2°C by century's end, threatening the stability of numerous ecosystems and the viability of vulnerable species.

Moreover, several concerning feedback mechanisms could exponentially accelerate the warming process:

- Ocean saturation: oceans currently absorb approximately half of anthropogenic CO_2 emissions, but their absorption capacity may become saturated;
- Permafrost melting: rising temperatures could lead to the release of significant quantities of methane trapped in permafrost;
- Changes in albedo: melting of ice caps reduces Earth's reflective surface area, leading to increased heat absorption.

Faced with this scenario, the research and implementation of alternative energy sources become not just desirable, but absolutely necessary.

1.2 The energy challenge

Renewable energy sources (RES) offer remarkable potential for sustainable power generation. Solar energy alone provides an annual potential of 173000 TW [4], vastly exceeding the current global energy demands of approximately 20 TW [5]. However, the widespread implementation of renewable energy

faces several significant challenges that must be addressed for successful large-scale adoption.

The temporal variability of RES presents a fundamental challenge for grid integration. Daily and seasonal fluctuations in availability, coupled with unpredictable output patterns, make it difficult to maintain stable power supply and match generation with demand patterns. This intermittency necessitates the development of robust energy storage solutions and sophisticated grid management systems.

Spatial constraints further complicate the deployment of renewable energy infrastructure. The low energy density of renewable sources requires substantial land allocation for meaningful power generation. This spatial requirement is compounded by the geographical mismatch between regions with high renewable energy potential and areas of significant energy demand, necessitating comprehensive transmission infrastructure.

The integration of RES with existing power infrastructure presents additional technical challenges. Current electrical grids, designed primarily for centralized power distribution, require significant modifications to accommodate the decentralized nature of renewable energy generation. The development of smart grids, enhanced transmission networks, and efficient storage systems becomes crucial for successful integration.

A critical solution to these challenges lies in the development of efficient energy storage systems, which would enable the temporal decoupling of energy supply and demand, allowing surplus energy to be stored and utilized during periods of low production. Indeed, the current limitations in renewable energy storage technology represent a significant bottleneck in the development and expansion of green electricity infrastructure, explaining the intensive research focus in this domain.

The field of energy storage encompasses diverse technological approaches, including electrochemical storage systems (batteries), mechanical storage (pumped hydroelectric), thermal storage systems, hydrogen production through water electrolysis, and chemical storage through fuel synthesis. As research in this field progresses, it has become evident that a single universal storage solution is unlikely to emerge. Instead, different applications and sectors will require tailored storage strategies optimized for their specific requirements. For instance, mobile applications such as transportation and aviation demand storage solutions with high energy density, while maintaining acceptable efficiency levels.

Direct electrification utilizing decarbonized energy sources remains the preferred approach where feasible. However batteries, the primary electrical energy storage system, have significant limitations: both their gravimetric and volumetric energy density is very low, in addition to having very long

recharge times.

A more sophisticated approach to energy storage involves the utilization of renewable electrical power to drive chemical reactions that produce energy-rich fuels. Water electrolysis represents the archetypal example of this strategy, where electrical energy is converted and stored in the chemical bonds of hydrogen (H_2). However, while hydrogen exhibits exceptional gravimetric energy density, its volumetric energy density presents significant limitations. This characteristic restricts hydrogen's practical applications primarily to scenarios where storage volume is subordinate to mass considerations, as exemplified in aerospace applications. Enhancement of hydrogen's volumetric energy density through compression or liquefaction processes necessitates additional energy input, significantly increasing production costs and reducing overall system efficiency. Moreover, the implementation of a hydrogen-based economy would necessitate extensive modifications to existing energy infrastructure, presenting additional technological and economic challenges.

Nobel Prize George Olah proposed an alternative solution: harnessing renewable electricity to drive endothermic reactions for the synthesis of liquid carbonaceous fuels, commonly referred to as "solar fuels" or "e-fuels", using CO_2 as carbon source [6]. These fuels have properties similar to those of fossil fuels, but they are carbon neutral if synthesized by CO_2 recycling.

Solar fuels can be produced through various processes, including CO_2 hydrogenation to methanol (CH_3OH), which follows the reaction:

$$CO_2 + 3H_2 \rightarrow CH_3OH + H_2O \tag{1.1}$$

Methanol is a liquid fuel, easy to handle, stock and distribute. It is an excellent gasoline substitute for internal combustion engines and can also be used in fuel cells for the production of electricity. It is also the basis for further steps processes to obtain dimethyl ether, which can substitute diesel fuel.

Another significant process is the dry reforming of methane, producing synthesis gas through the reaction:

$$CO_2 + CH_4 \rightarrow 2CO + 2H_2 \tag{1.2}$$

The obtained mixture of carbon monoxide and hydrogen is named syngas and is the basis for the synthesis of liquid fuels through the Fischer-Tropsch process.

Also the CO_2 splitting

$$CO_2 \rightarrow CO + \frac{1}{2}O_2 \tag{1.3}$$

represents an interesting pathway for carbon dioxide valorization, since the CO can be used as feedstock for Fischer-Tropsch synthesis.

The produced fuels are compatible with existing infrastructure, eliminating the need for extensive system modifications. They exhibit superior energy density characteristics compared to both batteries and hydrogen. Methanol, for instance, provides approximately 20 MJ/kg compared to 0.6-0.9 MJ/kg for lithium-ion batteries. Furthermore, when combined with carbon capture technologies, these processes can contribute to CO_2 recycling, potentially creating a more sustainable anthropogenic carbon cycle.

These reactions are strongly endothermic. The traditional approach to drive them is by thermal processes, which have several drawbacks:

- temperatures of thousands Kelvin are needed to achieve good conversions, resulting in a considerable heat dissipation;
- they take place in huge plants and are not suitable for small scale distribution.

This technology is applicable where a significant amount of renewable energy is available. For instance, in Iceland, the Carbon Recycling International company exploits the cheap and widely locally available geothermal energy to produce H_2 by water electrolysis and to drive its conversion with CO_2 into methanol. In this way Iceland is able to exploit and export its cheap and clean renewable energy [7].

1.3 Non-thermal plasmas for CO_2 valorization

In thermochemical processes, the energy needed to foster chemical reactions is provided in the form of heat and it is indistinctly distributed among all the degrees of freedom of the molecules. Non-thermal plasmas (NTPs, also called non-equilibrium or cold plasmas) can promote high-energy chemistry maintaining a relatively low gas temperature, since the energy is selectively channeled in the degrees of freedom needed for the reactions rather than in the heating of the gas. Non-thermal plasmas can be generated by electrical discharges in the gas and, being powered by electricity, they are suitable to be coupled to renewable energy sources. Furthermore, plasmas can match the intermittency of RES thanks to the low inertia.

To ignite the discharge, the voltage applied must be high enough to allow free electrons in the gas to gain the energy needed to ionize the molecules they collide with while accelerated toward the anode. The ions are accelerated towards the cathode, where they produce secondary electron emission, establishing an avalanche effect which makes the plasma self-sustaining.

1.3.1 Non-equilibrium in plasmas

Thermodynamic equilibrium occurs when all degrees of freedom in a system share the same temperature, denoted as T_{eq}. This happens when energy is supplied to the system more slowly than it can be redistributed among the degrees of freedom. However, if energy cannot be fully redistributed, the idea of a single equilibrium temperature no longer applies. Non-equilibrium conditions can be created by either limiting energy redistribution processes (e.g., by lowering the operating pressure) or by increasing the rate of energy input to the system.

In the discharge, the energy of the electric field is mainly transferred to electrons due to their much smaller mass compared to ions. Furthermore, elastic collisions between electrons and heavy species are highly inefficient in redistributing the energy, due to the small mass ratio ($m_{el}/m_{ion,neut} \sim 10^{-4}$), so in a good approximation electrons just change their directions without losing kinetic energy. Instead, due to the similar masses, ions easily lose their kinetic energy through collisions with neutrals. The only energy that the ions can gain is the electric field acceleration between one collision and the other.

On the other hand, inelastic processes are strongly energy dependent. Once the electrons have gained enough energy, they can excite the internal degrees of freedom of neutrals and ions. Electronic, vibrational and rotational excitations, as well as ionization and molecule dissociation, can be selectively activated depending on the specific cross sections of each process and the electron energy distribution function (EEDF).
Although the definition of temperature relies on the existence of an equilibrium condition, in plasma physics it is common to label with a temperature the mean energy of each degree of freedom of the system. In non-thermal plasmas a temperature hierarchy is then established [8]:

$$T_{el} > T_{vib} > T_{ion} \sim T_{rot} \sim T_{gas} \tag{1.4}$$

where $T_{el}, T_{vib}, T_{ion}, T_{rot}$ and T_{gas} are the electronic, vibrational, ion, rotational and gas temperature respectively, with typical orders of magnitude $T_{el} \sim 10^4 - 10^5$ K,$T_{vib} \sim 10^3 - 10^4$ K and $T_{gas} \sim 300$ K.
Under these non-equilibrium conditions, the electron kinetics is determined by solving the Boltzmann equation, obtaining non-Maxwell electron distribution functions and non-Boltzmann vibrational distribution functions. A description of possible non-Maxwellian solutions of the Boltzmann equation in non-equilibrium plasmas is found in [8].

1.3.2 CO_2 reduction in plasmas

The non-equilibrium can be exploited to perform strongly endothermic reactions, e.g. CO_2 dissociation, at relatively low temperature.
Depending on the electron energy distribution function, three different dissociation pathways can occur, as schematically shown in figure 1.2:

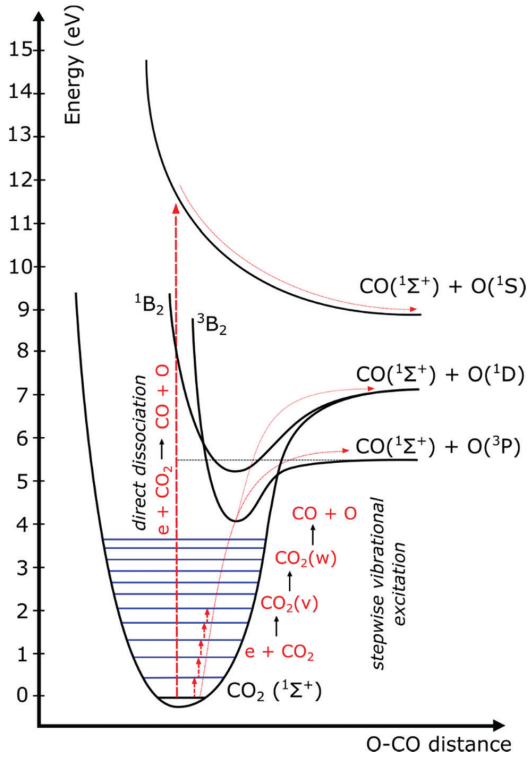

Figure 1.2: Potential energy curve of CO_2 and different dissociation pathways. Figure reported from [9].

- direct electron impact dissociation

$$e^- + CO_2(v = 0) \rightarrow CO + O + e^- \tag{1.5}$$

- electron impact dissociation from vibrationally excited levels

$$e^- + CO_2(v > 0) \rightarrow CO + O + e^- \tag{1.6}$$

- vibrational excitation

$$\begin{aligned} CO_2(v > 0) + CO_2(w > v) \rightarrow & CO_2(v - 1) + CO_2(w + 1) + \Delta\epsilon_{vw} \\ \rightarrow & CO + O + CO_2 \end{aligned} \tag{1.7}$$

where v amd w are vibrational states and $\Delta\epsilon_{vw}$ is a positive energy defect excess due to anharmonicity of the potential well.

The depth of the ground state is 5.5 eV. Direct electron impact dissociation 1.5 needs an electron energy > 7 eV to promote the molecule from the ground state to the first dissociative state [9], with an energy excess that limits the energy efficiency. If the electron impact occurs from excited vibrational levels 1.6, a reduced energy excess is required to reach a dissociative state. Process 1.7, the so-called *vibrational ladder climbing*, is instead the most efficient CO_2 splitting mechanism, since ideally only the minimum energy equivalent to the depth of the ground state is required. Once low vibrational levels have been populated by low energy electrons, collisions among vibrationally excited CO_2 molecules progressively populate higher vibrational levels eventually leading to dissociation [9]. The exchange of vibrational quanta, regulated by the vibration-to-vibration (VV) energy transfer, favours the population of higher vibrational levels thanks to the anharmonicity of the potential well [8], i.e. the fact that the energy spacing between adjacent vibrational levels decreases with the vibrational number. Hence, VV collisions tend to increase the highest vibrational level and decrease the lowest one instead of balancing them. This mechanism works for the asymmetric stretching vibration of CO_2, but not for the symmetric stretch or bending modes [10].

The VV energy transfer has to compete with the vibration-to-translation (VT) energy transfer, i.e. all collisional processes in which one or more vibrational quanta are lost in favour of kinetic energy. VT collisions depopulate high vibrational levels and are particularly temperature dependent, increasing at increasing T and establishing a positive feedback since they further heat the gas [8, 10, 11].

The effectiveness of the three mentioned dissociation pathways varies based on the kinetic energy of the electrons which is, in turn, influenced by the conditions of the discharge. The discharge properties can be tuned to selectively activate the desired channels. Figure 1.3 shows the fraction of electron energy transferred to the different processes varying the reduced electric field E/n, i.e. the ratio of electric field in the plasma over the neutral gas density.

Different kinds of discharge configurations for CO_2 valorization are investigated. They mainly differ for the kind of supplied power, reactor designs and working pressure. A comprehensive overview of the most frequently used discharge types is available in [9], where three types of NTPs are mostly discussed: dielectric barrier discharges (DBDs) [12, 13], microwave (MW) [14, 15], and gliding arc (GA) discharges [16, 17]. Additionally, other discharge types such as radiofrequency (RF) [18], corona [19] and glow dis-

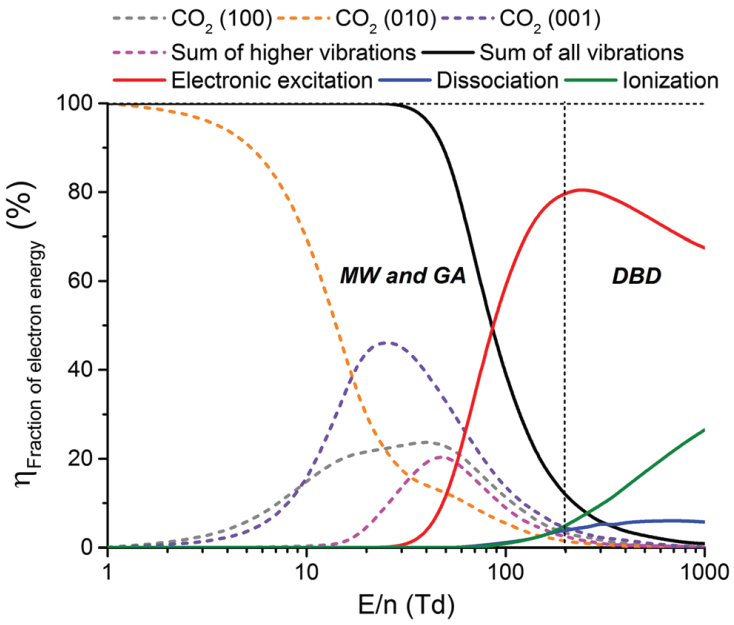

Figure 1.3: Fraction of electron energy transferred to different channels of excitation, ionization and dissociation of CO_2 as a function of the reduced electric field E/n. Figure reported from [9].

charges [20] are widely studied.

Among the many types of electrical discharges used in this field, nanosecond repetitively pulsed (NRP) discharges are a promising niche. These discharges are characterized by their transient nature, caused by rapid high-voltage pulses. This feature, combined with their ability to operate at atmospheric pressure, makes them particularly effective for generating non-equilibrium plasmas.

1.3.3 Nanosecond Repetitively Pulsed discharges

NRP discharges are a promising form of cold plasma for CO_2 valorization. Their ability to operate at atmospheric pressure is particularly advantageous because it eliminates the need for low-pressure control mechanisms. Typically, atmospheric pressure environments limit the degree of non-equilibrium due to the high frequency of collisions, which accelerates the relaxation and quenching processes. Despite these limitations, the rapid variation of the high-voltage signal in NRP discharges — characterized by voltage amplitudes of several kV, rise times of a few nanoseconds and full width at half

maximum (FWHM) of approximately 10 ns — enables the achievement of a high non-equilibrium.

Du et al. [21] used quantum cascade laser (QCL) absorption spectroscopy to investigate ro-vibrational excitation of CO_2 and CO_2 density in the afterglow of a nanosecond discharge in a 10% CO_2 mixture in He at 145 mbar, with a pulse width of 150 ns. They found that both gas temperature and vibrational temperature keep increasing in the early afterglow, reaching a peak at 3 μs. Non-thermal features are observed, with peak temperatures of $T_{v3} \approx 970$ K for the asymmetric stretch, $T_{v1,2} \approx 440$K for combined symmetric stretch and bending mode and $T_{rot} \approx 330$ K for the rotational temperature. The increase in gas temperature is moderate, favoring the CO_2 dissociation as reverse recombination process and the deexcitation of higher vibrational states are reduced. After the peak, an exponential decay of the vibrationally excited CO_2 population is observed, mainly attributed to VT transfer with He and deexcitation at the wall.

Collisional energy transfer laser induced fluorescence (CET-LIF) [22, 23] has been used by Martini et al. [24] to obtain time-resolved information on gas composition in the first microseconds after the pulse in a NRP discharge at atmospheric pressure. They found that a few microseconds after the discharge pulse, CO_2 is highly dissociated ($\sim$60%) with a temperature around 2500 K. In about 100 μs, the temperature decreases at about 1500 K while the dissociation towards a value $\sim$12%, the same obtained from then analysis of the effluent gas from gas chromatography. Modeling by Heijkers et al. [25] well reproduce these experimental results. The study reveals that electron impact dissociation from vibrationally excited CO_2 is the dominant conversion mechanism in NRP discharges, contributing approximately 70% of total dissociation. From high vibrational levels, also the dissociation from collision with an O atom (CO_2+O$\rightarrow$CO+O_2) or another molecule (CO_2+M$\rightarrow$CO+O+M) play a relevant role, as can bee seen from figure 1.4. However, several processes limit overall CO_2 conversion. Firstly, three-body recombination

$$CO + O + M \rightarrow CO_2 + M \tag{1.8}$$

in the afterglow significantly counteracts the conversion achieved during pulses. VT relaxation also causes rapid thermalization of the vibrational distribution function, reducing the population of higher vibrational levels crucial for efficient dissociation. These limitations result in a substantial drop in CO_2 conversion from over 50% at pulse termination to below 20% after 150 μs in the afterglow. The results of these studies suggest that efforts to improve the conversion should focus on avoiding the recombination instead of trying to dissociate more. The model showed that implementing

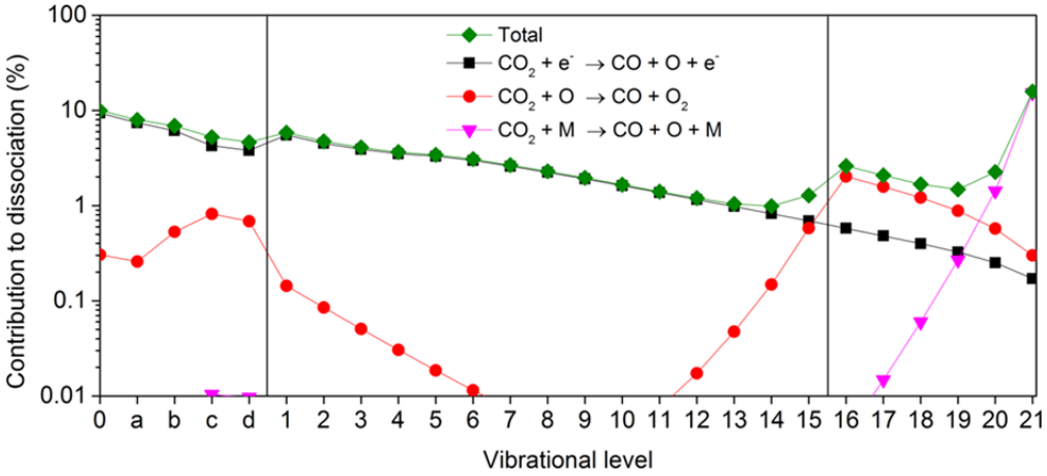

Figure 1.4: Contribution of the CO_2 ground state and the various vibrational levels to the total dissociation, as well as to the most important dissociation mechanisms. On the ascissa axis, "0" stands for the ground state,"a-d" represent four effective symmetric mode levels at low energy, while "1-21" are the asymmetric mode vibrational levels up to the dissociation limit of 5.5 eV. Figure reported from [25].

enhanced cooling strategies could mitigate these limiting processes, potentially improving overall conversion and energy efficiency in NRP discharges.

The interpulse time T_p plays a crucial role in the characteristics of NRP discharges. As the frequency of pulses increases, a memory effect is established. The memory effect is primarily caused by residual ions, free electrons, excited metastable species, and other long-lived active species that persist in the discharge gap between pulses, that can significantly influence subsequent discharges. At higher pulse repetition frequency, the accumulation of these species becomes more pronounced, leading to an overall lowering of the breakdown voltage compared to single pulse or low-frequency repetitive pulses [26, 27]. The gas heating and expansion from previous pulses can also play a role in facilitating the breakdown, lowering the impedance and increasing the conduction of the plasma channel [28].

In [29, 30] the effect of decreasing interpulse time (down to $\sim 10\mu$s) was clearly seen both from the electric I/V characteristics and from the imaging of the discharge. In fig. 1.5 we can see the I/V characteristics of the second pulse in a burst with different T_p and the relative images of the discharges with an exposure time that captures three pulses of the same burst. While for large interpulse time each pulse is spatially independent, for shorter T_p

they start to be more and more correlated until they completely follow the same channels of the first one. Decreasing T_p has also the effect of lowering the breakdown voltage and increasing the current. This denotes a higher number of free electrons but with lower energy, a condition that favour a vibrationally enhanced dissociation mechanism for CO_2. Indeed, high burst frequency improve the efficiency for CO_2 conversion [29] and dry reforming of methane (DRM) [30], with also improvements in the selectivity of CO and H_2.

Time-resolved optical diagnostics have been used to deepen the insight on the mechanisms taking place in the different kinds of plasma pulses. Ceppelli et at. [32] performed optical emission spectroscopy (OES) in the different regions of *type I* pulses, the ones with high interpulse time long enough so that each pulse is independent of the previous one, and *type II*, the pulses in a burst with short interpulse time, when a strong memory effect is established. In *type I* pulses, two different phases are recognized. The early breakdown phase is dominated by electron impact processes, with EEDF characterized by high energy electrons but relatively low electron density. It is followed by a spark regime when the plasma is re-ignited by successive power reflections in the transmission lines at much lower voltage, characterized by high ionisation degree and electron density but lower electron energy. Instead, *Type II* pulses show a sudden transition to the spark regime. Spectroscopic emission in the different regions and types of pulses revealed that CO_2 dissociation primarily occur in the later stages of the spark regime and possibly even after the discharge current has dropped. This suggests a long-lasting mechanism, potentially related to CO_2 vibrational excitation. This behaviour has been confirmed by the work of Montesano et al. [33], who carried out LIF spectroscopy measurements in the nanosecond timescale after the discharge pulse. They observed a delay of hundreds of nanoseconds between the discharge breakdown, i.e. the period when most of the energy is deposited, and when most of the CO_2 dissociation occurs. Furthermore, they saw that shortening the interpulse time in a burst lead to increments in the process efficiency, with less energy injected into the discharge to achieve similar conversions.

Post et al. [34] developed a novel pulsed power source capable of nanosecond pulses with burst frequencies up to 1 MHz and tested it in atmospheric pressure nanosecond pulsed discharge in pure CO_2. They used ex-situ FTIR absorption spectroscopy to analyse the effluent gas composition and the in-situ QCL absorption spectroscopy to measure the CO_2 vibrational temperature. The obtained CO_2 conversion and efficiency increase with bursts of 1MHz with respect to single pulses. Furthermore, they could qualitatively assess a more dense population of asymmetric stretch vibrational states.

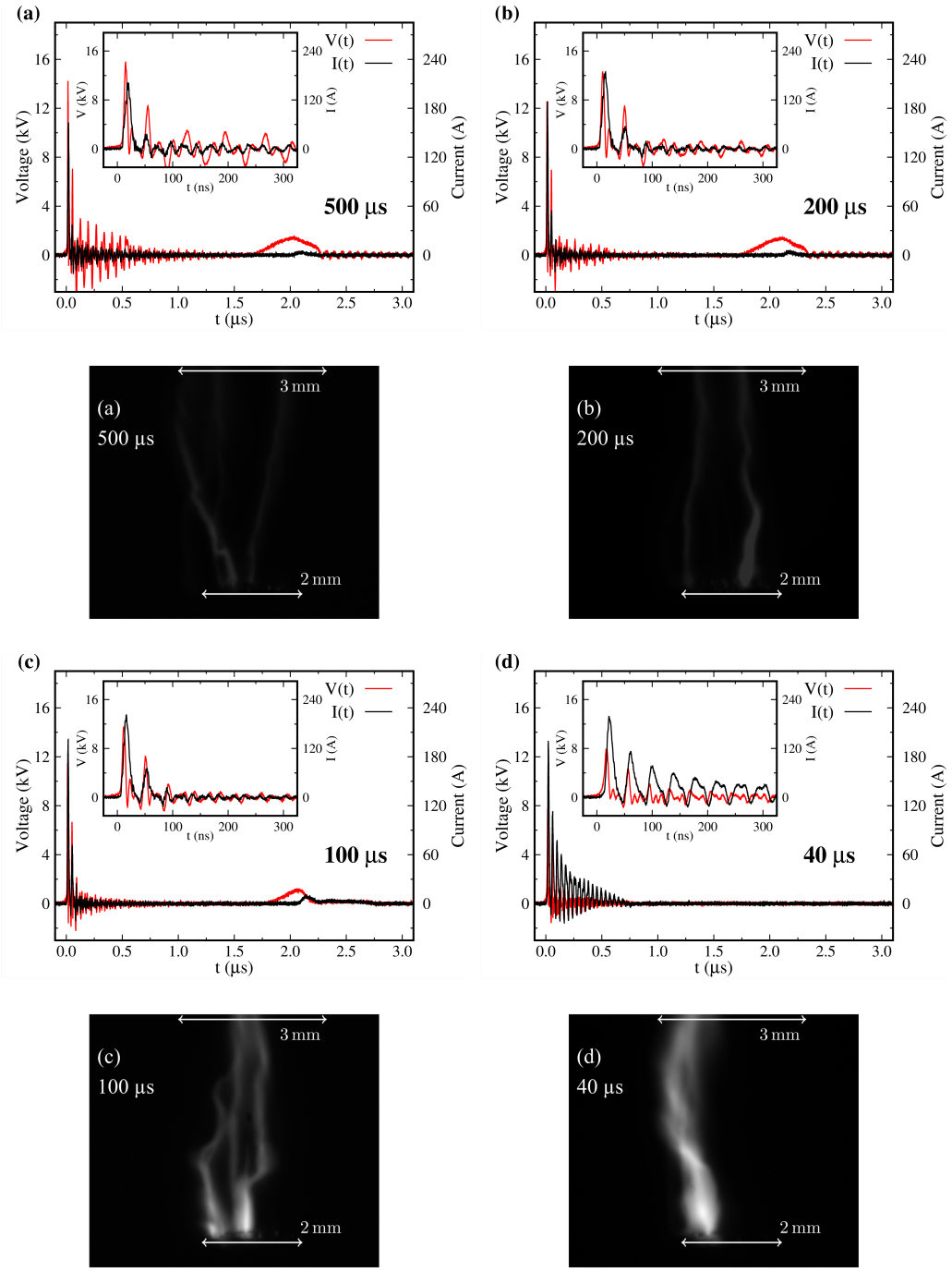

Figure 1.5: I/V characteristics (first and third row) of the second pulse in a burst of nanosecond pulses, and commutative images (second and fourth row) of a sequence of three pulses at different inter-pulse times: (a) 500 μs, (b) 200 μs, (c) 100 μs and (d) 40 μs. Anode (top arrow) and cathode (bottom arrow) sizes and positions are reported in the images. Figure reported from [31].

Other studies have shown that specific conditions and reactor design greatly influence the behaviour of NRP discharges. In the work from Richards et al. [35] a NRP at high repetition rate (100 kHZ) has been studied in a 5% CO_2 - N_2 mixture at 100 torr in plane-to-plane configuration and the vibrational population of the molecules has been measured. They observed vibrational excitation of both N_2 and CO_2 asymmetric stretch mode, but uncorrelated with the time-resolved rate of CO generation, suggesting that CO_2 dissociation via the vibrational excitation is a minor channel at their conditions. Kinetic modeling comparison indicates that CO is generated predominantly via the quenching of the excited electronic states of N_2 by CO_2.

Works from Bak et al. [36] and Yong et al. [37] studied NRP discharges at high pressure. In [36] nanosecond pulses with a repetition rate of 30 kHZ have been applied to CO_2 at a pressure in a range from 2.4 to 5.1 bar. For increasing pressure they found higher conversion but lower efficiency, attributed to the decreased electric field and electron energy per molecule. In [37], the pressure range has been extended from 5 to 12 bar. Here, the reduced electric field is much higher due to higher voltage and shorter gap. The efficiency exhibit low sensitivity to the variation of operating parameters (pressure, pulse energy and processing time) and seems only dependent on the specific energy input (SEI). Kinetic modeling showed the predominance of electron impact dissociation during the breakdown phase, while the vibrational mechanism are highly dominated by VT relaxation and do not contribute to dissociation.

1.4 Limiting factors for CO_2 conversion and possible improvements

The discharge parameters significantly impact the complex physical and chemical processes in CO_2 plasma, determining the main dissociation mechanisms and influencing subsequent reactions involving products. These reactions can lead to additional dissociation or back reactions, the main limiting factors for the final CO_2 conversion. Once the CO_2 molecule is dissociated, it generates an atomic oxygen, which is highly reactive and unstable and undergoes additional reactions. On the one hand, it can react with another CO_2 molecule and dissociate it. On the other hand it can oxidize CO back to CO_2 or quench the vibrational excitation of CO_2. Otherwise, two O atoms recombine into O_2. Therefore, atomic oxygen plays a crucial yet intricate role in the dynamics and efficiency of CO_2 plasma conversion [38].

Thanks to their simplicity, stability, well-known physics and diagnostic

accessibility, glow discharges are the most used for fundamental research and modeling, so many studies are available for this type of plasma, mainly at pressures in the range 0.2-5 torr [10,38–43]. In these low pressure conditions, CO_2 is mainly dissociated by direct electron impact and the recombination of atomic oxygen into O_2 molecules is more efficient than the reaction with CO giving back CO_2. However, the rates for these reactions are strongly temperature dependent and the rate of recombination with CO increases much more for highest temperatures (i.e. with the highest pressures), reaching the same order of magnitude [38]. Atomic oxygen can also react with vibrationally excited CO_2, giving CO and O_2. The rate of this process is very low in the conditions of these studies but it can increase with the vibrational excitation of CO_2 and contribute to the different behavior of O atom as function of the energy density [38].

Anyway, in this kind of discharge, the main recombination mechanisms involve molecular oxygen rather than atomic oxygen. The reaction

$$CO(a) + O_2 \rightarrow CO_2 + O \tag{1.9}$$

where CO(a) is the first electronically excited state of CO (entirely denoted as $CO(a^3\Pi_r)$), has been identified as the most significant recombination pathway. This state contribute to back-reactions, although to a lesser extent, also with CO:

$$CO(a) + CO \rightarrow CO_2 + C \tag{1.10}$$

On the other hand, for gas mixtures where CO_2 is still very abundant, CO(a) can also contribute to further dissociation reacting with CO_2:

$$CO(a) + CO_2 \rightarrow 2CO + O \tag{1.11}$$

This highlights the importance of electronically excited states in the kinetics of CO_2 discharges, which are often overlooked due to their low density and challenging detection [40, 41, 43, 44]. CO(a) is significantly populated in the studied conditions because it is the main product of CO_2 dissociation by direct electron impact with electron energies above 10 eV, the main dissociation process in this kind of plasma [44]. Electronically excited states carry a significant amount of energy which may influence relevantly the chemistry in the discharge. While atomic oxygen, as a very reactive species, is often believed to be the main contributor to back-reactions and many strategies have been developed to induce its recombination to O_2, we must take into account that, in conjunction with excited reaction partners, also O_2 is a relevant oxidation species [44].

Oxygen atoms, although not primarily responsible for recombination, play a complex role in the plasma dynamics. They can efficiently quench

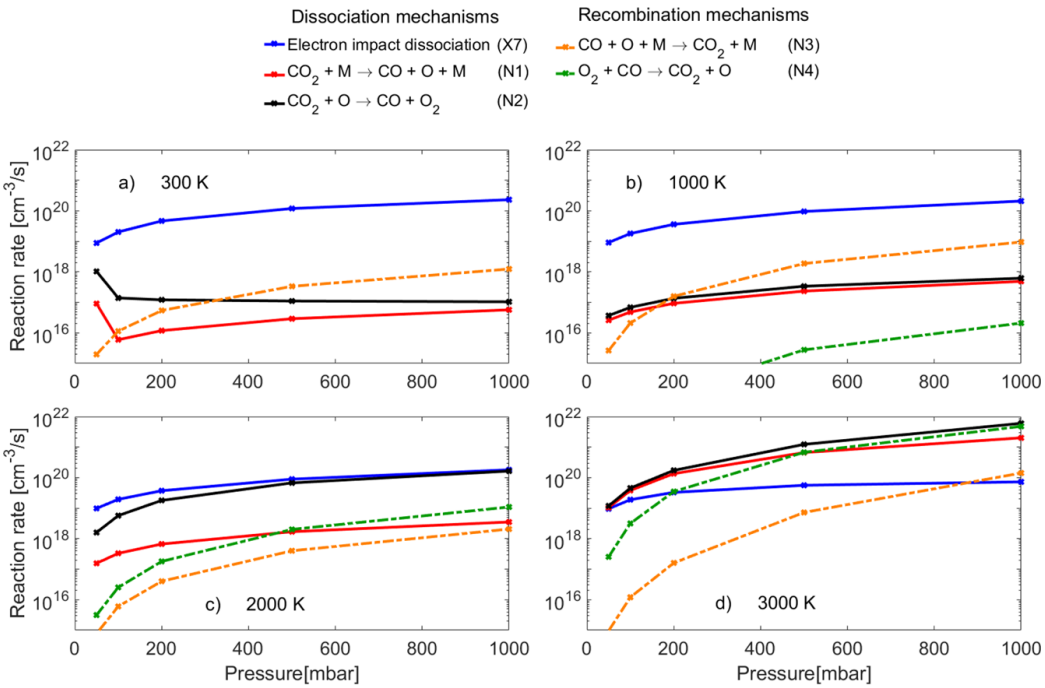

Figure 1.6: Reaction rates of the three main dissociation mechanisms and two main recombination mechanisms in MW CO_2 discharge as a function of pressure. The power deposition density increases linearly with pressure. Each panel corresponds to a different gas temperature: 300 K (a), 1000 K (b), 2000 K (c), and 3000 K (d). Figure reported from [11].

the vibrational excitation of CO_2, acting as a significant sink of vibrational energy [10, 42]. Additionally, these V-T relaxations contribute in heating the gas, establishing a positive feedback that further enhances vibrational quenching. Exploiting the fact that, in glow discharges, atomic oxygen density is dominated by surface recombination processes [38], Morillo-Candas et al. [39] demonstrated this quenching effect through experiments using large specific surface materials to enhance O atom recombination, while leaving unaltered all other plasma parameters. This results in increased vibrational excitation of CO_2 and CO.

In microwave (MW) discharges with high enough power density, vibrational excitation becomes the main contributor to CO_2 dissociation and therefore high efficiencies can be achieved [45]. However, the performances of this kind of plasma drastically drop at atmospheric pressure, which is a limitation for applications. Berthelot and Bogaerts [11] studied a model to simulate the mechanisms in a CO_2 microwave discharge varying the pressure from 50 mbar to 1 bar. The main dissociation pathway is vibrational

excitation followed by VV energy transfer and subsequent neutral-neutral reactions (CO_2+M→CO+O+M and CO_2+O→CO+O_2). The optimal conditions that maximize conversion and efficiency is found to be at 300 mbar. Increasing gas pressure and temperature critically affects the process, increasing detrimental VT relaxation and promoting the main recombination process (CO+O+M→CO_2+M and O_2+CO→CO_2+O), whose rates increment is much more pronounced than that of dissociation mechanism, as can be seen from figure 1.6. The model also shows that cooling in the afterglow mitigates this effects at higher pressures, significantly improving the efficiency, while it does not have any effect at low pressures where recombination processes are almost negligible [11].

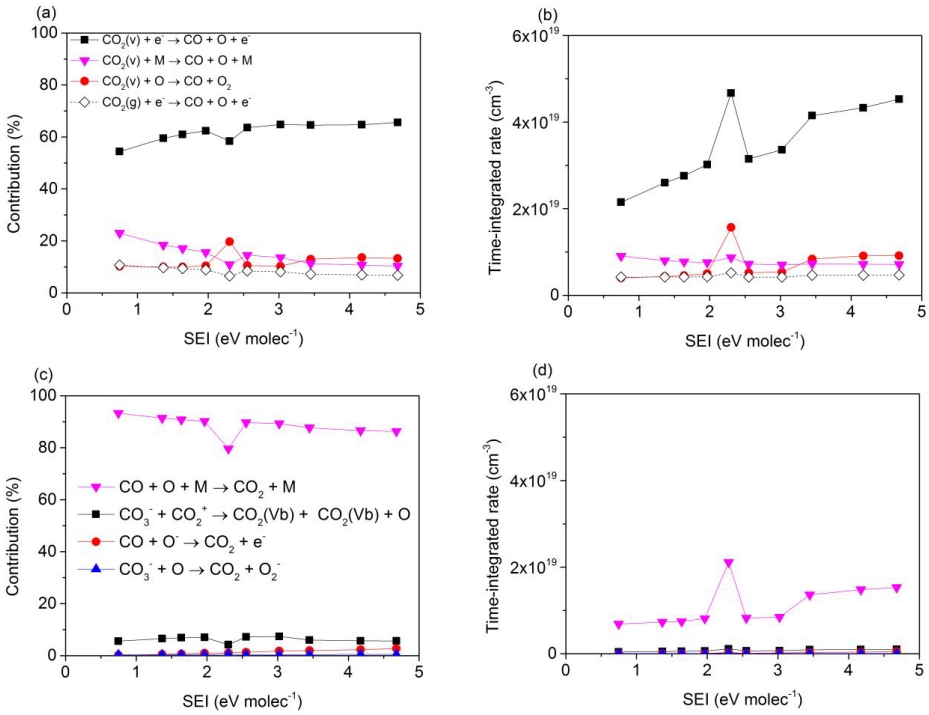

Figure 1.7: Contribution of the most important dissociation (a) and formation (c) mechanisms of CO_2, and their corresponding time-integrated rates (b, d) as a function of SEI. Figure reported from [46].

Returning to our nanosecond pulsed discharge, the modeling from Heijkers et al. [25] revealed that the high CO_2 dissociation, reached with the help of vibrationally excited levels drastically drops in the afterglow due to the back-reaction (1.8). The contribution of the main dissociation and

recombination processes is illustrated in figure 1.7. Another important limitation is related to VT relaxations, which cause the thermalization of the vibrational distribution function in the afterglow. Furthermore, both recombination processes and VT relaxations significantly contribute to heating, with a self-accelerating effect that further induces more recombination and VT relaxation. The simulation has been exploited to test the possible effect of external cooling in the afterglow, as a possible solution to improve conversion and energy efficiency. While dissociation is still dominated by electron impact dissociation from CO_2 vibrational levels, with accelerated cooling the dissociation from collision with another molecule M gradually becomes more important. The reasons are, firstly, the lower VT rate, that allows a higher population of high asymmetric stretch vibrational levels, the ones that majorly bring to dissociation by other molecule or oxygen atom collisions (see fig.1.4. Secondly, the drop in the 3-body recombination reaction rate ($CO + O + M \rightarrow CO_2 + M$), thus increasing the net contribution of the dissociation pathway upon collision with molecules. This explains the better dissociation and efficiency obtained in the simulation, with an increment up to a factor of 2.2 for 10 times higher cooling.

1.4.1 Techniques to enhance conversion and efficiency

The findings of various studies indicate that two actions can improve the conversion and efficiency in CO_2 utilization: rapid cooling in the afterglow to prevent the reverse reaction by lowering temperature-dependent rates, and separating the products to eliminate atomic or molecular oxygen from the gas mixture before recombination. Removing oxygen species from the effluent gas is also beneficial for obtaining an O_2-free effluent gas (ideally pure CO) directly usable in industrial applications, such as the Fischer-Tropsch process.

The effect of the addition of water-cooled quenching nozzles in the effluent of a CO_2 MW plasma torch has been experimentally investigated by Hecimovic et al. [47] at pressures from 100 to 900 mbar and simulated by Alphen et al. [48] by 3D fluid dynamic model and quasi-1D chemical kinetics. A huge enhancement in the conversion and efficiency has been obtained at high pressure, especially for low flow rates, with conversion improvements up to a factor seven, from 5% without nozzle to 35% with quenching nozzle. The performances at sub-atmospheric pressure have been brought to values similar to the low pressure ones, making it much more suitable for industrial applications. The main effect of the nozzles is to force the mixing of the hot treated gas swirling in the center of the reactor with the cold and untreated CO_2 in the periphery [48]. Due to the tangential gas injection, these two regions are kept separate and, without the nozzle, a very weak heat transfer

subsist among them, and the only cooling present is due to convective cooling from the gas stream, which is more significant at higher flow rates. For this reason the quenching nozzle is much more effective for low flow rates. Furthermore, the nozzle walls (being water-cooled) induce additional conductive cooling.

A recent work from Wang et al. [49] combined 2D modeling and experimental study to investigate the recombination mechanisms and the effect of cooling in a CO_2 atmospheric pressure plasmatron. They developed an innovative in-situ gas sampling method to map the 2D spatial distribution of the gas composition along the afterglow and used it to validate the fluid dynamics and reaction kinetics model of the main dissociation and recombination processes taking place in the discharge and afterglow. They also developed a plasmatron reactor with a two-stage cooling system to validate the performance enhancement predicted by the simulation. The cooling was implemented with two water jackets around the reactor walls, both filled with flowing water at $\sim$298 K, the upstream one closer to the plasma region and the downstream one. Figure 1.8 show their reactor and how the blue flame visible in the afterglow without cooling, presumably indicative of strong CO recombination, almost completely disappear with cooling, leaving unchanged all the discharge power [49]. They obtained an enhancement in both CO_2 conversion and efficiency up to a factor 3, especially for low flow rates. Furthermore, thanks to the segmented cooling system, the effect of quenching in just one of the two regions could be tested, showing that the upstream stage is the most effective one. This underscores the importance of early quenching in inhibiting recombination processes in the afterglow.

Attempts of enhancing the conversion by oxygen removals are also reported. Mori et al. [50] investigated CO_2 dissociation in a hybrid reactor combining dielectric barrier discharge (DBD) and solid oxide electrolyser cell (SOEC). While in the DBD reactor alone the CO_2 conversion saturates with residence time, it continues to increase monotonically in the hybrid system due to oxygen removal by the SOEC suppressing reverse reactions. CO_2 conversions up to 90% have been reached at the effluent of the hybrid reactor. An analytical model using first-order reaction kinetics successfully reproduces experimental results for both systems. The model also shows that CO_2 splitting occurs primarily through reactions with reactive oxygen species rather than direct electron impact. So, in the hybrid system, both forward and reverse reaction rates are reduced due to oxygen removal.

Hollow fiber membranes have been tested [51, 52] in MW discharge reactors similar to the one used by Hecimovic at al. [47] at atmospheric pressure. These LCCF membranes are characterized by their exclusive permeability toward oxygen, good thermal properties, and high tolerance against

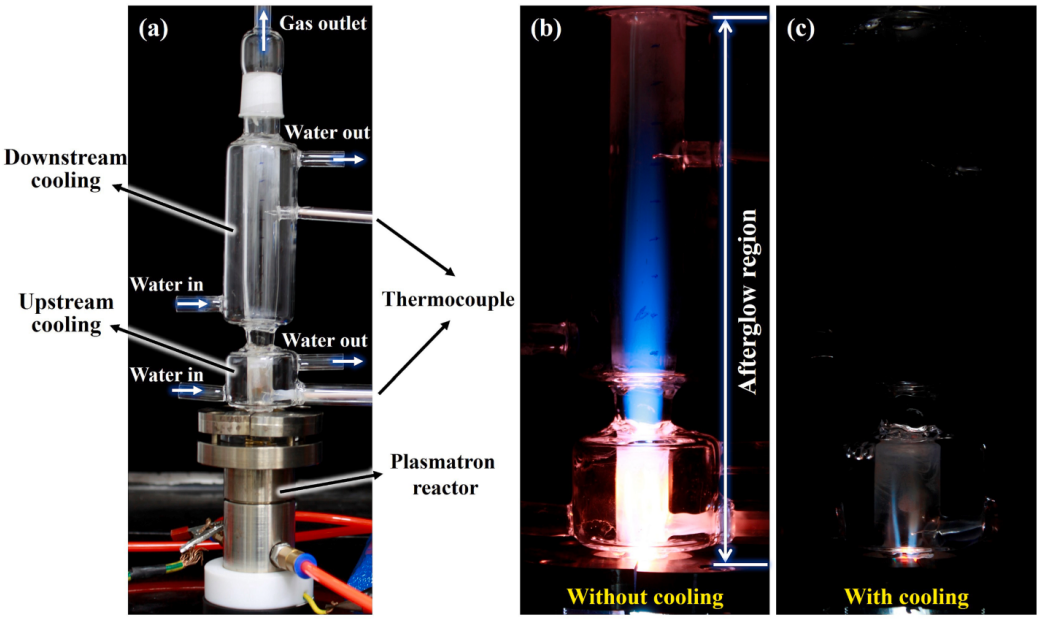

Figure 1.8: Picture of the plasmatron reactor with afterglow quenching (a), and photograph of the afterglow region without cooling (b) and with cooling implemented (c). Figure reported form [49].

CO_2. The permeation rates are governed by oxygen partial pressure across the membranes and temperature exceeding 700 °C are required to activate them. Their performances in the plasma environment is very promising. The amount of permeated O_2 from the membrane in air plasma was higher than that with air in a conventional oven at comparable temperatures, due to the presence of oxygen atoms that permeate more easily in the membrane. However, the reactor used for these experiments was designed to study the behaviour of the membranes instead of optimizing the CO_2 conversion, which did not show any enhancement due to oxygen removal. This is probably caused by further stainless-steel pieces inside the reactor that, if not properly cooled, act as heat reservoir enhancing recombination [52].

A plasma-assisted chemical looping (PACL) process for CO_2 conversion has been investigated by Delikonstantis et al. [53] for a nanosecond repetitively pulsed discharge. As we already saw in section 1.3.3, in NRP discharges CO_2 is highly dissociated ($\sim$60%) in the first microseconds, before back-reactions make the dissociation drop to values $\sim$12% [24]. A nanostructured CeO_2/Fe_2O_3 oxygen scavenger material, prereduced by H_2 plasma, placed downstream to the plasma, captures the produced oxygen species, thereby suppressing recombination processes. A 3-fold higher conversions

(∼29%) than state-of-the-art plasma technologies is achieved at the reactor outlet. The oxidized material must be periodically reactivated by feeding pure H_2 instead of CO_2, in a plasma environment producing H_2O.

These studies show the great potential for developing techniques that prevent the recombination. They illustrate how freezing the products before they can undergo back-reaction can significantly improve the conversion of CO_2 into plasma and the energy efficiency of the process. These findings clearly warrant further research and development to advance the use of plasma-assisted CO_2 conversion for industrial applications. In the process of CO_2 dissociation, oxygen is generated as a byproduct and must be eliminated. Atomic oxygen, which is formed when CO_2 splits, is a very reactive radical. When it combines to form O_2, or when we capture and remove it, we are essentially discarding its enthalpy. An idea is to utilize it by causing it to react with other chemical species to produce additional valuable products.

An example of this concept can be found in the work from Girard-Sahun et al. [54], who tackled the removal of O/O_2 from the products by placing a carbon bed downstream of a gliding arc plasmatron reactor. Through the process of carbon gasification, carbon interacts with O atoms or molecular oxygen and further CO is produced. The carbon bed significantly enhanced CO_2 conversion, nearly doubling it from 7.6% to 12.6%, while also increasing energy efficiency from 27.9% to 45.4% and increasing the CO concentration in the exhaust by a factor of three and nearly eliminating O_2. However, time-resolved measurements reveal that the performances are only enhanced in the first minutes, followed by a drop to values below the ones without carbon bed. Modeling revealed that the onset of oxygen complexes led to deactivation of the carbon bed over time, which starts to produce CO_2 instead of CO. The model showed that limiting this oxygen coverage, such as by providing additional heating to the carbon bed, could sustain the enhanced performances over time.

1.5 This thesis

This thesis deals with two main topics regarding nanosecond repetitively pulsed discharges for CO_2 valorization.

The recombination of CO with oxygen represents a crucial limitation for plasma-based CO_2 valorization. Chapter 2 investigates an innovative approach to harness atomic oxygen productively, rather than treating it as an unwanted byproduct. We explored the interaction between CO_2 plasma products and ethylene (C_2H_4) introduced in the post-discharge region of a NRP discharge. The aim is to exploit oxygen from CO_2 splitting for the

production of ethylene oxide (C_2H_4O), simultaneously preventing its recombination with CO and improving the final CO_2 conversion. Ethylene oxide is a valuable chemical feedstock with widespread industrial applications and its production using oxygen from CO_2 dissociation would significantly enhance the total process efficiency. Through systematic variation of C_2H_4 injection parameters, we obtained remarkable results. While ethylene oxide formation was not detected, we observed a non-monotonic effect on CO_2 conversion, revealing intriguing kinetics in CO_2/C_2H_4 plasmas. Notably, CO_2 conversion can be both enhanced or decreased based on the ethylene addition. These findings open new avenues for understanding and optimizing plasma-chemical processes for CO_2 valorization.

In chapter 3, the issue of measuring energy in a nanosecond discharge is addressed. The energy dissipated in the plasma is a crucial parameter for evaluating the process efficiency and comparing it with other experiments or methodologies. When the high voltage pulses have a duration of 10 ns or lower, measuring the applied voltage becomes non-trivial due to issues related to commercially available HV probes, which have high parasitic capacitance and narrow bandwidth [55]. Therefore, custom techniques need to be developed and characterized. One example is the Back Current Shunts (BCS) technique. We tested the suitability of BCS for our discharge and compared the results with the energy measured using commercial current and HV probes. Our measurements reveal that the conventional probe method significantly overestimates energy deposition compared to the BCS technique, primarily due to the probe's influence on system impedance. This assessment provides crucial guidance for choosing appropriate measurement techniques based on specific research requirements, whether prioritizing absolute accuracy or practical experimental considerations.

Chapter 4 presents the main conclusions and future perspectives of these studies.

Chapter 2

Effects of C_2H_4 addition

The reasons of this study are inspired by the work of Xu et al. [56]. They obtained an enhancement in CO_2 conversion in a RF plasma jet by making it interact with liquid alkenes, which reacted with atomic oxygen yielding epoxidation processes. Epoxides are key building blocks and important intermediates in organic synthesis, widely used in the preparation of several products including pharmaceuticals, polymers, adhesives and paints [57]. Traditional epoxidation methods rely on stoichiometric oxidants such as peracids (e.g. m-chloroperoxybenzoic acid) or halogen-based oxidants, which, while effective, generate substantial amounts of hazardous waste and suffer from poor atom economy, leading to environmental concerns and increased production costs [58]. Sequestration of atomic oxygen by the alkene prevents its back-reaction with CO, increasing CO concentration in the plasma afterglow by up to 70%. At the same time, atomic oxygen is not thrown away but exploited as a green oxidant in further reactions that lead to valuable products. The concept is schematized in figure 2.1.

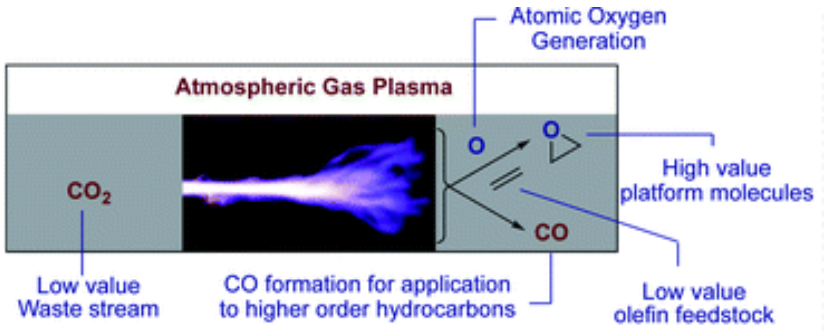

Figure 2.1: Scheme of epoxidation with atomic oxigen from CO_2 plasma reduction. Figure reported from [56].

We want to investigate whether this approach is reproducible in our NRP discharge. To do it, we decide to use ethylene (C_2H_4), the simplest alkene, with the aim of producing ethylene oxyde (C_2H_4O).

Ethylene oxide is a crucial industrial chemical with widespread applications and significant economic importance. As one of the most produced organic compounds globally, it serves as a key intermediate in the synthesis of numerous products essential to modern life. The primary use of C_2H_4O is in the production of ethylene glycol, an essential component in polyester fibers, antifreeze formulations and polyethylene terephthalate (PET) plastics. Additionally, C_2H_4O is employed in the manufacture of surfactants, detergents, thickeners, solvents, plasticizers, and various other specialty chemicals. Its high reactivity makes it valuable in the production of sterilizing agents for medical equipment and pharmaceuticals [59]. The global demand for ethylene oxide continues to grow, driven by increasing consumption of polyester fibers and PET in emerging economies, as well as the expansion of healthcare and personal care industries worldwide. For its production, 10-15 Mt of CO_2 are released every year [60]. The ability to synthesize this valuable product using atomic oxygen derived from CO_2 dissociation, while simultaneously preventing its recombination, would represent a significant dual benefit in terms of both resource utilization and process efficiency.

The effect of adding small amounts of ethylene in a CO_2 NRP discharge or immediately after the plasma have been investigated. To the best of our knowledge, CO_2 plasma discharges with addition of C_2H_4 had never been tried before.

Several works from the group of Chavadej, Suttikul et al. [61–66] study ethylene epoxidation in non-equilibrium plasmas, using DBD and corona discharges in O_2 and C_2H_4. They investigate the effect of many different parameters in order to maximize the C_2H_4O selectivity and yield and the process efficiency: applied voltage, input frequency, residence time, O_2/C_2H_4 feed molar ratio etc. They also found that a separate feed of C_2H_4 and O_2, with ethylene added at different positions in the inter-electrode gap, result in better ethylene epoxidation performances than the mixed feed of C_2H_4 together with oxygen. Indeed, while oxygen needs to be activated in the plasma, lowering the ethylene residence time leads to a decrease in opportunity of C_2H_4 molecules to be activated by generated electrons: as a result, all undesired reactions including C_2H_4 cracking, dehydrogenation, oxidation, and coupling reactions are lowered.

In this work, measurements have been performed by adding ethylene in different amounts or configurations and comparing the results to the case of just CO_2 dissociation in absence of other species.

In this chapter, after the definition of the used performance parameters,

the experimental set up and methods will be presented, followed by the experimental results and discussion.

2.1 Performance parameters

The performance parameters taken into account for the studied processes are defined in the following.

Specific Energy Input

In plasma chemistry, the Specific Energy Input (SEI) is a crucial parameter to asses the efficiency of a process. It quantifies the amount of energy applied to a system per unit of gas or reactant processed. It is typically expressed in kJ L^{-1}, kJ mol^{-1} or eV $molecule^{-1}$. It can be calculated by:

$$\begin{aligned} \mathrm{SEI(kJ\,L^{-1})} =& \frac{\mathrm{P(kW)}}{\Phi(\mathrm{L\,min^{-1}})} \cdot 60\,\mathrm{s\,min^{-1}} = \\ =& \frac{\mathrm{E_p(kJ)} \cdot \mathrm{f_p(Hz)}}{\Phi(\mathrm{L\,min^{-1}})} \cdot 60\,\mathrm{s\,min^{-1}} \end{aligned} \tag{2.1}$$

where P(kW) is the power dissipated in the discharge, Φ(L min^{-1}) is the flow of the reactants entering the reactor, E_p(kJ) is the energy per pulse and f_p(Hz) is the pulse repetition frequency.

To express the SEI in other units, the applied conversions are:

$$\mathrm{SEI(kJ\,mol^{-1})} = \mathrm{SEI(kJ\,L^{-1})} \cdot 22.4\,\mathrm{L\,mol^{-1}} \tag{2.2}$$

$$\mathrm{SEI(eV\,molecule^{-1})} = \mathrm{SEI(kJ\,L^{-1})} \cdot \frac{6.24 \cdot 10^{21}\,\mathrm{eV\,kJ^{-1}} \cdot 22.4\,\mathrm{L\,mol^{-1}}}{6.022 \cdot 10^{23}\,\mathrm{molecule\,mol^{-1}}} \tag{2.3}$$

Conversion of reactants

The conversion of reactants is the percentage of a reactants molar flow entering the reactor that is converted:

$$\mathrm{C_X(\%)} = \frac{\dot{n}_X^{in} - \dot{n}_X^{out}}{\dot{n}_X^{in}} \cdot 100 \tag{2.4}$$

where $\dot{n}_X^{in}$ and $\dot{n}_X^{out}$ are the input and output molar flow of the reactant species X, respectively.

Selectivity

The selectivities of the products are parameters that denote how the atoms of the converted reagents redistribute among the products. The selectivity of an atomic species on a certain product is defined as the percentage of those atoms from the converted reactants that goes in the composition of that specific product. This quantity is computed for each atomic species in the gas mixture (C, O and H) on each produced molecular species containing that atom.

As an example, the selectivity of C in the hydrocarbon C_xH_y is defined as:

$$S^{C}_{C_xH_y} = \frac{x \cdot \dot{n}^{out}_{C_xH_y}}{C_{CO_2} \cdot \dot{n}^{in}_{CO_2} + 2 \cdot C_{C_2H_4} \cdot \dot{n}^{in}_{C_2H_4}} \tag{2.5}$$

Balance

The last parameters that we take into account are the balances of the elements in the gas mixture: C, O and H. They refer to the accounting of all atoms of a specific element across inputs and outputs of the reaction and are defined as the ratio of the sum of the atoms of that element in the output stream over that of the input stream. The balances are needed for the mass conservation verification and check the consistency of the analytical method.

$$B_C(\%) = \frac{\dot{n}^{out}_{CO_2} + 2 \cdot \dot{n}^{out}_{C_2H_4} + \dot{n}^{out}_{CO} + \sum_{C_xH_y} (x \cdot \dot{n}^{out}_{C_xH_y}) + \dot{n}^{out}_{H_2CO}}{\dot{n}^{in}_{CO_2} + 2 \cdot \dot{n}^{in}_{C_2H_4}} \cdot 100 \tag{2.6}$$

$$B_H(\%) = \frac{4 \cdot \dot{n}^{out}_{C_2H_4} + \sum_{C_xH_y} (y \cdot \dot{n}^{out}_{C_xH_y}) + 2 \cdot \dot{n}^{out}_{H_2CO} + 2 \cdot \dot{n}^{out}_{H_2CO}}{4 \cdot \dot{n}^{in}_{C_2H_4}} \cdot 100 \tag{2.7}$$

$$B_O(\%) = \frac{2 \cdot \dot{n}^{out}_{CO_2} + \dot{n}^{out}_{CO} + \dot{n}^{out}_{H_2CO} + \dot{n}^{out}_{H_2O}}{2 \cdot \dot{n}^{in}_{CO_2}} \cdot 100 \tag{2.8}$$

2.2 Experimental set-up and methods

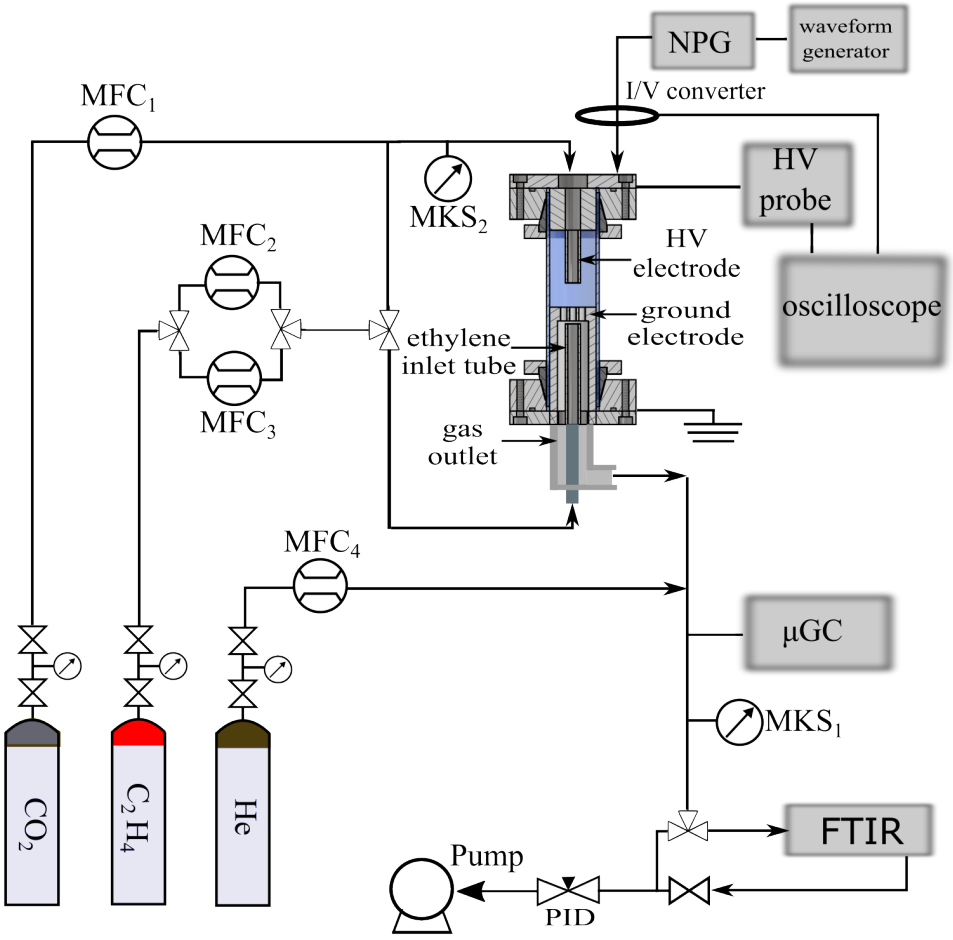

Figure 2.2: Setup scheme.

A scheme of the experimental setup is shown in figure 2.2. The discharge takes place in the reactor in flowing gas at atmospheric pressure, is generated by the Nanosecond Pulse Generator (NPG). Current and voltage are acquired by probes and their signals are recorded by means of a digital oscilloscope. The outlet gas is analyzed using both a Micro Gas Chromatographer (μGC) and a FTIR Spectrometer. A paper filter is placed in the line between the reactor and the analytic instruments. The experiment is carried out at atmospheric pressure and room temperature. In the following, the details of each part will be exposed.

2.2.1 The reactor

The reactor has a pin to plate configuration, where the electrodes are respectively also the inlet and outlet of the gas. The anode is a sintered tungsten tube with an outer diameter of 3 mm and an inner diameter of 2 mm. The cathode is a stainless steel cylinder of 9 mm external diameter and 6 mm internal diameter; on its top, seven 1.5 mm holes let the gas flow out. The electrodes are screwed on stainless steel flanges where electric contacts are attached. The reactor wall is a quartz tube of 13 mm outer diameter and 10 mm inner diameter. The inter-electrode gap has been kept constant to 5 mm.

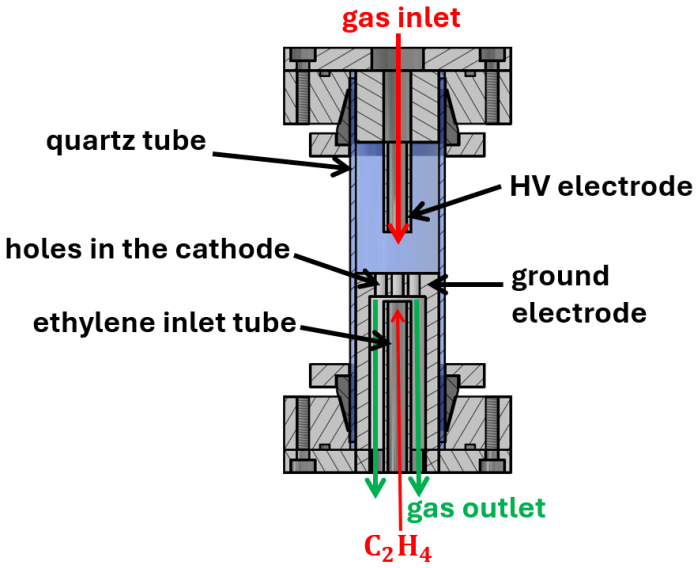

Figure 2.3: Scheme of the reactor.

2.2.2 C_2H_4 addition methods

Ethylene is added either from the anode together with CO_2, varying the C_2H_4 flow while keeping a constant CO_2 flow, or under the cathode, trying to avoid its entrance in the reactor and to make it interact only with the discharge products as they exit the rector.

For ethylene addition under the cathode, a tube concentric to the cathode cylinder with 3 mm outer diameter and 2 mm inner diameter is used as the C_2H_4 inlet. CO_2 flows from the anode and the plasma products flow out from the cathode where they find C_2H_4.

Different tubes for C_2H_4 inlet under the cathode have been tried, to study the effects of varying how far from the discharge zone and in which direction

Figure 2.4: Tubes for ethylene input downwards under the cathode. From left to right, the slits depth is 10, 8, 5, 3 and 1 mm.

the ethylene flow is added and to try to prevent it from entering the reactor:

- a simple tube towards the cathode, which has been shifted up and down at different distances from the cathode surface;
- five different tubes with closed ends and 2 slits pointing downwards at 45° with respect to the cathode; in the different tubes, the slits are at a distance of 1, 3, 5, 8 and 10 mm from the top of the tube, which always touches the cathode in order to avoid of parasitic discharges between the cathode and the ethylene tube. These tubes are shown in figure 2.4.

2.2.3 Gas handling system

The gas species used in the experiment are CO_2 (99.998% purity), C_2H_4 (99.95% purity) and helium (99.999% purity). The latter is added downstream the reactor and used as internal standard for the μGC measurements, as will be explained in section 2.2.5. The flows are controlled by mass flow controllers (MFC), MKS 1179A. MFC_1 for CO_2 has a full scale (FS) of 500 sccm. Ethylene can be sent to two different MFC depending on the needed flow: MFC_2 with FS 500 sccm for flows $\geq$10 sccm and MFC_3 with FS 10 sccm for lower flows. MFC_4 with FS 5 sccm is used for He. MFCs are calibrated on nitrogen, therefore the Gas Correction Factor (GCF) must be taken into account for different species: GCF_{CO_2}=0.7, $GCF_{C_2H_4}$=0.622 and GCF_{He}=1.45. The accuracy of the MFCs is $\pm$(0.5% of reading + 0.2% of FS).

After the helium stream is added to the gas flow from the reactor, the gas can be either sampled by the μGC or sent in the FTIR spectrometer. A rotary pump guarantees the continuous flow of the gas. The pressure is monitored by two strain gauges at the input of the reactor and after the μGC and is controlled and stabilized at 985$\pm$8 mbar by an proportional valve and a proportional-integral-derivative (PID) controller. This operating pressure has been chosen to be slightly higher than the maximum ambient pressure of our lab, located at 400 m a.s.l. in Povo (Trento), in order to avoid contamination by air in the line in case of small leaks.

2.2.4 Electrical characterization

The HV generator is a Megaimpulse NPG 18/3500, which provides a HV pulse up to 18 kV on a matched load, with FWHM $<$ 10 ns and rising time $<$ 4 ns. The percentage of the maximum power to be delivered can be adjusted with a knob. The frequency of the discharge pulse can be set up to 3500 Hz and triggered by an external signal, which we set using a waveform generator (Agilent 33220A). The nanosecond pulse generator is connected to the reactor by a 3 m long PK 75-7-15 cable provided by the producer.

Voltage and current are measured respectively with a high-voltage probe (Tektronick P6015A, bandwidth = 75 MHz) and a current trasformer (Magnelab CT-C1.0-BNC, bandwidth =200 Hz-500 MHz). V(t) and I(t) signals are acquired by a digital oscilloscope Teledyne Lecroy HDO 9104, with bandwidth of 1 GHz and a sampling rate of 20 GSa s^{-1}. The current signal is attenuated by means of a 20 dB BNC attenuator at the oscilloscope port. An example of the acquired signals is shown in figure 2.5. The peaks successive to the first one are due to reflections that occur at the reactor due to

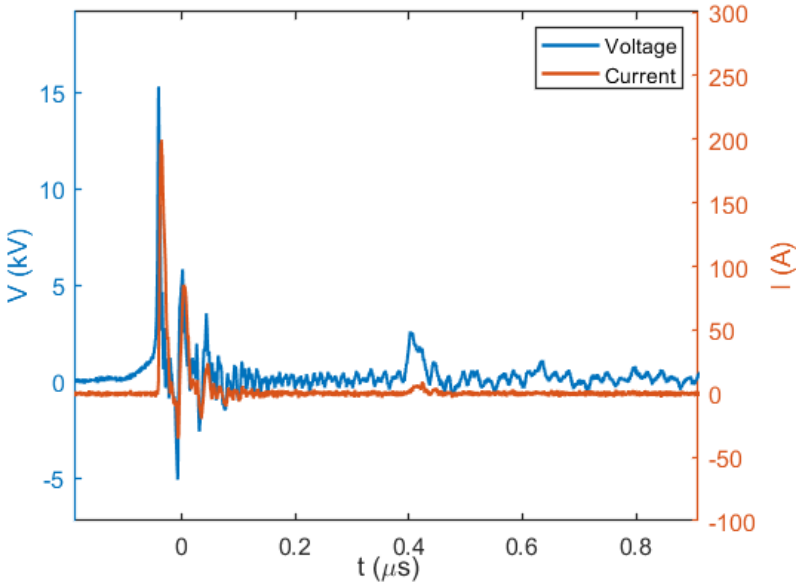

Figure 2.5: Example of voltage and current signals.

the impedance mismatch with the transmission line: the signal is partially reflected back and forth the 3 m long cable. The bump at around 400 ns that appears in fig. 2.5 is due to a re-trigger of the NPG and it is able to re-ignite the discharge.

The acquisition system introduces a spurious delay τ between current and voltage signals,due to several factors: compensation circuit of the HV probe, spacing between voltage and current probes, the amplification stage of the oscilloscope and length of the cables. This delay must be taken into account when the energy of the pulse is calculated:

$$\mathrm{E_{pulse}} = \int_{\mathrm{T_{pulse}}} \mathrm{V(t)} \cdot \mathrm{I(t+\tau)dt} \tag{2.9}$$

where $\mathrm{T_{pulse}}$ is the duration of the pulse signal.

The delay τ can be estimated by a discharge inhibition method: the reactor is filled with Freon 13, a substance characterized by a breakdown voltage high enough to prevent the discharge. In this condition the load is assumed to be purely reactive and the energy calculated by eq. 2.9 must be zero. Therefore, shifting I(t) with respect to V(t) to set to zero the resulting $\mathrm{E_{pulse}}$, the delay τ can be determined. The resulting values is

$$\tau = 3.89 \pm 0.03\,\mathrm{ns} \tag{2.10}$$

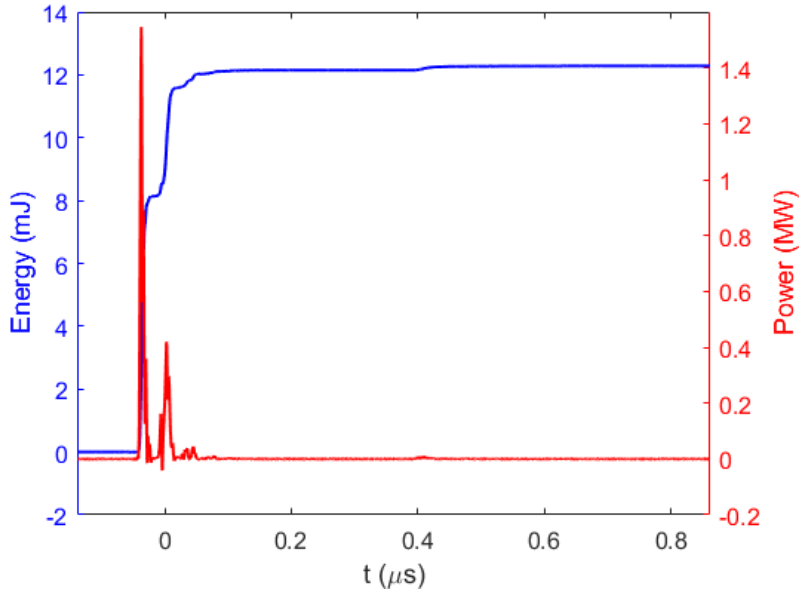

Figure 2.6: Instantaneous power and cumulative energy computed for the pulse shown in figure 2.5.

Furthermore, from the signals acquired in absence of discharge, the capacitance C of the system (reactor + probes) can be estimated. Indeed, assuming a purely capacitive load, the measured current I(t) corresponds to the displacement current $I_{disp}(t)$:

$$I(t) = I_{disp}(t) = C \cdot \frac{dV(t-\tau)}{dt}. \tag{2.11}$$

From the fit of the measured current on the derivative of the measured voltage as in eq. 2.11, the obtained capacitance is C=6.4±0.1 pF.

The I/V signal acquisition was automated using a custom LabView routine which collects 30 discharge samples from the oscilloscope. The pulse energy (E_{pulse}) was calculated for each voltage-current signal pair, allowing for the determination of the average value and associated standard deviation:

$$E_{pulse} = \langle \sum_{i=0}^{29} \int_{T_{pulse}} V_i(t) \cdot I_i(t+\tau) dt \rangle \tag{2.12}$$

Figure 2.6 shows the instantaneous power and the cumulative energy dissipated in the discharge by the pulse. Despite the average power deposited is of the order of some tens of Watts, the instantaneous power can reach some MW. The first pulse is responsible for the highest amount of deposited energy

in the plasma. The second reflection also contribute with ∼25% of the total deposited energy, while from the third the contribution is almost negligible.

The deposited energy per pulse is used to calculate the specific energy input as in equation 2.1, taking into account also the accuracy of the mass flow controllers that regulate the flows.

2.2.5 The Micro Gas Chromatograph

The analysis of the effluent gases is mainly performed by means of a Micro Gas Chromatograph. Gas chromatography is an analytical technique widely used for separating and analyzing complex mixtures of volatile compounds. This method exploits the differences in the physical and chemical properties of analytes as they interact with a stationary phase within a column and a mobile gas phase. As the sample components travel through the column, they separate based on their unique affinities for the stationary phase, resulting in different retention times. These retention times, coupled with detector responses, allow for both qualitative identification and quantitative analysis of mixture components.

A specific variant of gas chromatography is the gas-solid chromatography, which utilizes a solid stationary phase, packed or coated within a column, and a gas carrier that pushes the sampled gas through it. The separation mechanism relies on the different adsorption of gaseous species on the surface of the solid adsorbent material, leading to varying retention times. This techinque is particularly effective for separating light gases, low molecular weight hydrocarbons, and other volatile compounds that may be challenging to analyze using liquid stationary phases.

The used instrument is an Agilent 990 MicroGC equipped with two columns: a MolSieve 5A with backflush and a PoraPlot U. The two columns are respectively 20 and 10 m long and the detectors are thermal conductivity detector (TCD), which measure the difference in thermal conductivity between the carrier gas and the analytes as they elute from the column, providing a response proportional to the concentration of the sample components. The MolSieve separates the lightest molecules, as He, H_2, O_2, CH_4 and CO, while the PoraPlotU can separate CO_2, C_2-hydrocarbons and propane. The employed gas carrier for the two columns is Argon.

A chromatogram is the output signal of the μGC and it is the TCD detector voltage signal as a function of time, with gaussian peaks centered at the retention time of the substance and whose area is directly related to the molecular fraction of the corresponding gas species. The response factor R_X of the TCD directly relates the area of the peak A_X to the molecular fraction

Column	MolSieve 5A	PoraPlot U
Injector heating (°C)	100	75
Column heating (°C)	110	75
Injection time (ms)	30	10 - 30
Column pressure (Psi)	35	28

Table 2.1: Settings of the Micro GC methods. The two different injection times for the PoraPlot U column refer to the two different methods alternately used in the measurements with ethylene.

m_X of the corresponding gas X:

$$A_X = R_x \cdot m_X \tag{2.13}$$

The determination of R_X requests a calibration curve of the TCD detector for each species X involved in the reaction. For the input species (CO_2, C_2H_4 and He) the calibration has been performed varying the proportion among the fluxes in the gas line. For the products, three auto-produced mixtures simulating the composition of the effluents after the plasma process have been used to generate the calibration curves of the TCD detector.

The settings of the two columns are reported in table 2.1. For the PoraPlot U column, two different methods have been alternately used for the measurements with ethylene: a shorter injection time (10 ms) is used to work in the linear regime for CO_2 quantification, a longer injection time (30 ms) is used to have a higher signal for low concentration products (C_2H_6, C_2H_2 and C_3H_8). The injection time is the only difference among the two methods.

Once calibrated, the μGC measurements output is the molar fraction of the species in the gas sample, defined as the flow of the species X over the total flow:

$$m_X = \frac{\dot{n}_X}{\dot{n}_{tot}} \tag{2.14}$$

The molar fraction must be related to the quantities defined in section 2.1, first of all the conversion of the reactants C_X defined in equation 2.4, which depends on the input and output molar flow of a species:

$$\begin{aligned} C_X(\%) =& \frac{\dot{n}_X^{in} - \dot{n}_X^{out}}{\dot{n}_X^{in}} \cdot 100 = \\ =& \frac{\dot{n}_X^{off} - \dot{n}_X^{on}}{\dot{n}_X^{off}} \cdot 100 \end{aligned} \tag{2.15}$$

where the notation in/out are replaced by off/on respectively, indicating the μGC measurements in the absence (off) or presence (on) of the discharge.

However, when a reaction occurs, the output flow is generally not the same as the input one:

$$\dot{n}_{tot}^{in} \neq \dot{n}_{tot}^{out} \tag{2.16}$$

Let us consider for example the CO_2 splitting:

$$xCO_2 \rightarrow (x-\alpha)CO_2 + \alpha CO + \frac{\alpha}{2}O_2 \tag{2.17}$$

The initial amount of moles (x) differs from the final one ($x+\frac{\alpha}{2}$). Therefore, C_{CO_2} cannot be calculated by simply considering the outcomes of the μGC measurement with the discharge off and on, because $m_{CO_2}^{on}$ refers to a different total molar flow. To clarify this point, let us consider a typical situation in this kind of measurements.

EXAMPLE

Let us assume a CO_2 flow with discharge off:

$$\Phi_{CO_2} = 100\,\text{sccm}$$

and a CO_2 conversion

$$C_{CO_2} = 20\%.$$

The total output flow with the discharge on would be

$$\Phi_{tot}^{on} = (1 - C_{CO_2}) \cdot \Phi_{CO_2}^{off} + \Phi_{CO}^{on} + \Phi_{O_2}^{on} =$$

$$= (1 - C_{CO_2}) \cdot \Phi_{CO_2}^{off} + C_{CO_2} \cdot \Phi_{CO_2}^{off} + \frac{C_{CO_2}}{2} \cdot \Phi_{CO_2}^{off} = 110\,\text{sccm}$$

The molar fraction given by the μGC refers to this total flow with discharge on, therefore it would be:

$$m_{CO_2}^{on} = \frac{\Phi_{CO_2}^{on}}{\Phi_{tot}^{on}} = \frac{80\,\text{sccm}}{110\,\text{sccm}} = 72.7\%$$

If we calculate the conversion by replacing $\dot{n}_X^{on/off}$ with $m_X^{on/off}$ in eq. 2.15 we would obtain

$$C_{CO_2} = (1 - 0.727) \cdot 100 = 27.3\%.$$

The initial assumption was $C_{CO_2} = 20\%$, hence an error of about 30% came out by this simulation using just the molar fractions to calculate the conversion.

To overcome this issue, it is necessary to explicit the variation of the moles with the reaction:

$$\begin{aligned} C_{CO_2} =& \frac{\dot{n}^{off}_{CO_2} - \dot{n}^{on}_{CO_2}}{\dot{n}^{off}_{CO_2}} = \\ =& \frac{m^{off}_{CO_2} \cdot \sum_i \dot{n}^{off}_i - m^{on}_{CO_2} \cdot \sum_i \dot{n}^{on}_i}{m^{off}_{CO_2} \cdot \sum_i \dot{n}^{off}_i} = \\ =& \frac{m^{off}_{CO_2} - m^{on}_{CO_2} \cdot \frac{\sum_i \dot{n}^{on}_i}{\sum_i \dot{n}^{off}_i}}{m^{off}_{CO_2}} = \\ =& \frac{m^{off}_{CO_2} - m^{on}_{CO_2} \cdot \xi}{m^{off}_{CO_2}} \end{aligned} \tag{2.18}$$

where the index i runs over all the species in the mixture and the factor $\xi = \frac{\sum_i \dot{n}^{on}_i}{\sum_i \dot{n}^{off}_i}$ accounts for the mole variation occurring with the reactions in the discharge.

A method to quantify ξ is by introducing an internal standard (IS): a constant flux of a different gas species is added after the reactor and before the μGC sampling point. For this purpose, helium is used in this work. The area A_{IS} of the IS in the chromatogram depends on its concentration in the mixture via the response factor of the TCD:

$$A_{IS} = R_{IS} \cdot m_{IS} = R_{IS} \cdot \frac{\dot{n}_{IS}}{\dot{n}_{IS} + \sum_i \dot{n}_i} \tag{2.19}$$

The ratio of the areas with plasma off and plasma on will be:

$$\begin{aligned} \frac{A^{off}_{IS}}{A^{on}_{IS}} =& \frac{R_{IS} \cdot \frac{\dot{n}_{IS}}{\dot{n}_{IS} + \sum_i \dot{n}^{off}_i}}{R_{IS} \cdot \frac{\dot{n}_{IS}}{\dot{n}_{IS} + \sum_i \dot{n}^{on}_i}} = \\ =& \frac{\dot{n}_{IS} + \sum_i \dot{n}^{on}_i}{\dot{n}_{IS} + \sum_i \dot{n}^{off}_i} \end{aligned} \tag{2.20}$$

Let us now express $\sum_i \dot{n}^{on}_i$ as as function of the quantities that are known or can be measured by the μGC:

$$\sum_i \dot{n}^{on}_i = \frac{A^{off}_{IS}}{A^{on}_{IS}} \left(\dot{n}_{IS} + \sum_i \dot{n}^{off}_i \right) - \dot{n}_{IS}. \tag{2.21}$$

The correction factor ξ can be expressed as

$$\xi = \frac{\frac{A^{off}_{IS}}{A^{on}_{IS}} \left(\dot{n}_{IS} + \sum_i \dot{n}^{off}_i \right) - \dot{n}_{IS}}{\sum_i \dot{n}^{off}_i} \tag{2.22}$$

If the amount of internal standard $\dot{n}_{IS}$ is much smaller than the total species entering the reactor

$$\dot{n}_{IS} << \sum_i \dot{n}^{off}_i \tag{2.23}$$

then equation 2.22 simplifies to:

$$\xi = \frac{\sum_i \dot{n}_i^{on}}{\sum_i \dot{n}_i^{off}} \simeq \frac{A_{IS}^{off}}{A_{IS}^{on}} \tag{2.24}$$

Hence, the correction factor ξ to be applid to the molar fractions of the output gas can be obtained by the ratio of the areas of the IS with discharge off and on.

2.2.6 Fourier Transform Infrared Spectroscopy

Fourier Transform Infrared (FTIR) spectroscopy is an analytical technique for the characterization of gaseous mixtures that provides valuable insights into the composition of a gas with a non-intrusive method for real-time monitoring and analysis.

FTIR spectroscopy is based on the interaction of infrared radiation with molecular vibrations. When exposed to infrared light, molecules absorb specific frequencies that correspond to their ro-vibrational modes. The resulting spectrum provides a unique "fingerprint" of the molecular composition of the sample. In plasma chemistry, FTIR spectroscopy is particularly useful due to its ability to identify multiple gaseous species simultaneously, offering high sensitivity and spectral resolution and providing quantitative information on gas concentrations.

In this work, FTIR spectroscopy is used *ex-situ*, i.e. in the analysis of the effluent gas after it exits the plasma reactor, once stable products are reached. Among the plasma chemistry community, *in-situ* FTIR spectroscopy is also commonly used [38–42, 44]: it consists in directly measuring the gas within the reactor, allowing the detection of both stable molecules and transient species and enabling time-resolved monitoring of the reactions taking place. This technique is particularly valuable for studying reaction kinetics and understanding transient phenomena in the plasma. By adjusting the path of the IR beam, different regions of the plasma can be probed, providing also some spatial resolution of the gas in the reactor.

Differently from gas chromatography, FTIR spectroscopy does not need a calibration. Thanks to the ro-vibrational spectra, molecular species can be recognized and this allows the identification of unknown products.

For the quantitative analysis, the Beer-Lambert law directly relates spectral features to the concentration:

$$A(\tilde{\nu}) = \epsilon_{mol}(\tilde{\nu}) \cdot l \cdot c_{mol} \tag{2.25}$$

where A is the absorbance, ϵ is the attenuation coefficient specific to each molecule and wavenumber $\tilde{\nu}$, l is the length of the optical path traveled by the IR beam and c is the concentration of the absorbing species in the gas. This relationship is obviously valid only for bands where a single species composing the gas mixtures is absorbing, and is not valid for overlapping band. The spectrum is a function of the wavenumber $\tilde{\nu}$, which is expressed in cm^{-1}.

In this work, FTIR spectroscopy is a complementary tool with respect to the μ-GC, in order to detect and quantify the gas molecules that cannot be measured with the other instrument, mainly H_2O and formaldehyde (H_2CO). Furthermore, the absortpion spectra are used to check the presence of other possible products that we are not able to recognize through the μ-GC, e.g. the ethylene oxide (C_2H_4O), due to the lack of standards for the calibration. The instrument used is a Bruker Equinox 55, with a 200 cm cell where the effluent gas flows at a pressure of 985 mbar. The used resolution is 1 cm^{-1}.

The instrument works connected to the OPUS software. It provides the absorbance spectrum as

$$A = -\log_{10} T. \tag{2.26}$$

T is the transmittance, given by

$$T = \frac{I}{I_0} \tag{2.27}$$

where I_0 is the intensity if the reference beam and I is that of the beam after the interaction with the analyte.

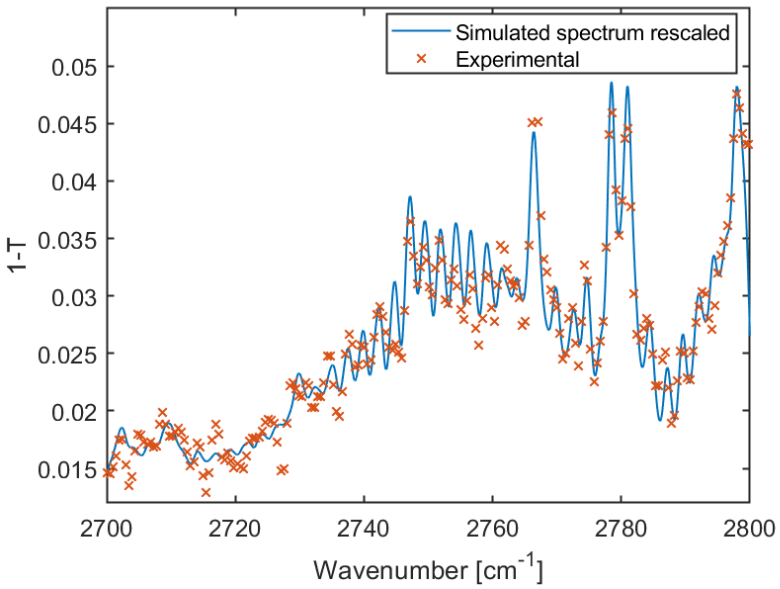

Figure 2.7: Example of a fit of H_2CO absorption spectrum.

For the quantification, the obtained experimental spectra must be compared with reference spectra, which can be generated through the Spectral Calc website (`https://www.spectralcalc.com/`) that provide simulated spectra from a gas cell. The generated spectra are based on HITRAN2020 (high-resolution transmission molecular absorption), a spectroscopic database containing detailed information on molecular absorption lines and cross-sections for various gases [67]. Spectral

Calc produces a simulated transmittance spectrum T_{sc} taking into account the user's input parameters: length of the optical path, pressure, temperature and an expected concentration c_{sc} of the observed molecular species in the gas sample. The spectrum from Spectral Calc is convoluted with a gaussian with σ=0.5 cm^{-1} to obtain a width of 2σ corresponding to our resolution of 1 cm^{-1}. The simulated absorption spectrum expressed as

$$1 - T_{sc} = 1 - 10^{-A_{sc}} = 1 - 10^{-(\epsilon l c_{sc})} \tag{2.28}$$

corresponding to the expected concentration c_{sc}, is used to fit the experimental spectrum

$$1 - T_{exp} = 1 - 10^{-A_{exp}} = 1 - 10^{-(\epsilon l c)} \tag{2.29}$$

through the fitting parameter d=c/c_{sc} used as

$$1 - 10^{-(A_{sc} \cdot d)} = 1 - 10^{-A_{exp}}. \tag{2.30}$$

The real concentration c of the molecular species in the gas sample is obtained by $d \cdot c_{sc}$.

The concentration of H_2O is obtained by the band from 3960 to 4000 cm^{-1} and that of H_2CO from 2700 to 2800 cm^{-1}. The choice of the bands for the fit is crucial to avoid spectral regions where the bands are saturated or overlap with other molecules, due to the presence of many different molecular species absorbing in the investigated bandwidth. An example of the fitting of H_2CO experimental and simulated spectra is shown in figure 2.7.

2.2.7 Optical emission spectroscopy

To assess if ethylene added after the cathode enters the discharge zone, optical emission spectroscopy has been used to check the presence of Hα emission line (656.28 nm) in the plasma in some of the C_2H_4 inlet configurations. Indeed, since hydrogen atoms can only come from ethylene and not from the CO_2 plasma, the presence of this emission line in the spectra would be a clear sign of the ability of C_2H_4 added in the post-discharge to climb back inside the reactor despite the flow in the opposite direction.

A spectrometer Avantes AvaSpec-3648 has been used for this purpose, with a spectral range from 600.081 to 816.517 nm and 0.071 nm resolution. The end of an optical fiber with a collimator has been placed in front of the reactor and the collected emitted light is sent to the spectrometer.

The need for this optical emission check arose later during the measurements and it was not taken into account during the experimental design, so the setup was not optimized for this kind of measurement. Each time the reactor had to be opened to change the ethylene inlet tube, the relative position with respect to the collimator could not be perfectly restored, affecting the intensity of the collected light. Hence, this information has to be treated just qualitatively: although a relative intensity of

the Hα peak can be taken into account with a proper normalization of the spectrum, we are meanly interested in the boolean information of presence or absence of hydrogen in the plasma mixture.

2.2.8 Parameters of the sets of measurements

The goal of this work is to asses the effect of the addition of ethylene in different configurations with respect to the case of simple CO_2 splitting, hence other parameters, e.g. the SEI, have been kept constant.

To continuously check the benchmark and avoid drifts in the reactor behaviour due to the use and the aging of the materials, a measurement of simple CO_2 splitting without ethylene have been performed before and after every measurement with C_2H_4.

Two main different sets of measurements have been performed. In the first series, the ethylene is added under the cathode with the simple concentric tube described in section 2.2.2 that was shifted up and down from 1 to 10 mm from the cathode. In these measurements, the CO_2 flow was 100 sccm and 10 sccm of ethylene were added. The pulse repetition frequency was 1 kHz and the average SEI resulted in 173±4 kJ/mol. The same settings for flows and frequency have been used for a measurement with C_2H_4 addition directly in the reactor together with CO_2.

To further avoid ethylene entrance in the discharge zone, the second set of measurements has been done with the C_2H_4 inlet tubes with the downward slits. Both CO_2 and C_2H_4 flows have been doubled in order to increase the pressure gradient and disfavor the ethylene entrance in the reactor. Therefore, also the pulsing frequencies has been doubled and brought to 2 kHz, in order to roughly maintain the same SEI as the previous set and allow a comparison among the two data sets. However, the measured mean SEI resulted slightly lower: 164±2 kJ/mol.

The same working point of 200 sccm of CO_2 and 2 kHz pulsing frequency has been used for measurements with ethylene addition directly in the reactor together with CO_2. The C_2H_4 flows has been varied from 0.3 to 20 sccm.

2.3 Results

2.3.1 C_2H_4 addition under the cathode

As mentioned in section 2.2.8, the first series of measurement has been performed choosing a working point of 100 sccm CO_2 and 1 kHz pulsing frequency and adding 10 sccm C_2H_4 under the cathode with the simple tube, i.e. with an upward flow. The ethylene tube has been shifted up and down to distances of 1, 3, 5, 7 and 10 mm from the cathode, in order to map the life of the plasma products in the afterglow.

Figure 2.8 shows the CO_2 conversion as a function of the C_2H_4 inlet depth for this set of measurements. The C_{CO_2} values are compared with the benchmark, i.e. the CO_2 conversion in the case of simple CO_2 splitting in absence of ethylene, denoted with its statistic error by the green area, resulting $C_{CO_2} = 8.4 \pm 0.6\%$. The obtained CO_2 conversion values are much higher than the benchmark when C_2H_4 is added at just 1 mm from the cathode, and decreases towards the reference value for decreasing depth, until reaching even lower values for the deepest ethylene addition at 10 mm.

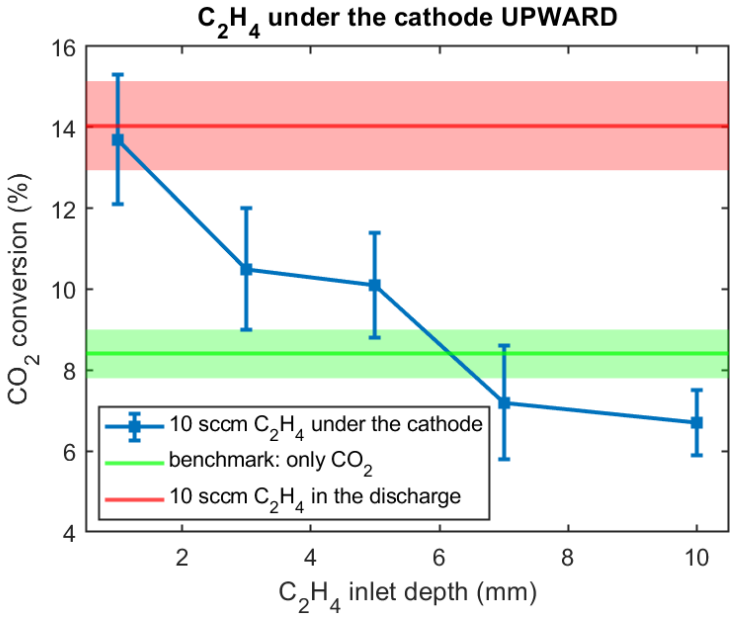

Figure 2.8: CO_2 conversion vs C_2H_4 inlet depth in the case of 1 kHz pulsing frequency, 100 sccm CO_2 and 10 sccm C_2H_4 added under the cathode with upward flow. The green area represents the CO_2 conversion without ethylene addition and its uncertainty, while the red area denotes the case of C_2H_4 added directly in the reactor in mixed feed with CO_2.

The products molar fractions are shown in figure 2.9. One of the main results is that the produced O_2 decreases of almost one order of magnitude when C_2H_4 is added closer to the reactor. Simultaneously, CO production increases, and so does also H_2. Shifting the ethylene inlet closer to the cathode, the hydrocarbons (CH_4, C_2H_6, C_2H_2 and C_3H_8) appear among the products and increase their molar fraction. On the other hand, H_2O and formaldehyde (H_2CO) molar ratios increase when ethylene is added deeper under the cathode. Ethylene oxyde has never been found among the products in the FTIR spectra.

Hence, the first doubt arose: is ethylene entering the reactor counterflow despite the pressure gradient in the system? Two diametrically opposite attempts have been tried to clarify this:

- adding ethylene directly in the reactor together with CO_2, in order to have an upper limit benchmark corresponding to the case of 100% of added ethylene in the discharge, maintaining the same flows and SEI (173±4 kJ/mol);
- further avoiding ethylene entrance in the reactor by both changing its inlet flow directions and increase the pressure gradient: the simple tube has been substituted with the tubes with downward slits shown in figure 2.4 and both the CO_2 and C_2H_4 flows have been doubled.

The CO_2 conversion in the cases of ethylene added in the discharge in mixed feed with CO_2 resulted in $C_{CO_2} = 14.0 \pm 1.1\%$ and is depicted by the red area in figure 2.8. It is similar to the case of ethylene added 1 mm below the cathode, suggesting that in the latter configuration ethylene could almost completely enter the discharge zone.

The graph in figure 2.10 illustrates the results of CO_2 conversion when 20 sccm of ethylene are added under the cathode in a 2 kHz discharge with 200 sccm of CO_2, using the tubes with the downward slits. As mentioned in section 2.2.8, also the pulsing frequency has been varied in order to roughly keep the same SEI as the previous series, which now resulted 164±2 kJ/mol, slightly lower than the former case. The benchmark C_{CO_2} is also somewhat smaller (6.6±0.6%), probably due to a higher heating caused by the increased pulsing frequency.

Here the CO_2 conversion is never much higher than the benchmark, and it decreases to values lower than the only CO_2 case for 3 and 5 mm inlet depth, then increasing again towards the benchmark value when the inlet configuration does not allow ethylene to significantly interact with the plasma or its products. The initial part of this curve, i.e. the points closer to the cathode, is similar to the final one (farthest part from the discharge) of the previous set of measurement with upward ethylene stream, suggesting that the downward inlet stream has the same effect of shifting down the upward stream. This non-monotonic behaviour of the CO_2 conversion as a function of the ethylene inlet depth, with values varying from higher to lower with respect to the benchmark, is unexpected and intriguing.

The ethylene conversion $C_{C_2H_4}$ is shown in figure 2.11 for both upward and downward configurations. The corresponding $C_{C_2H_4}$ for the case of ethylene addi-

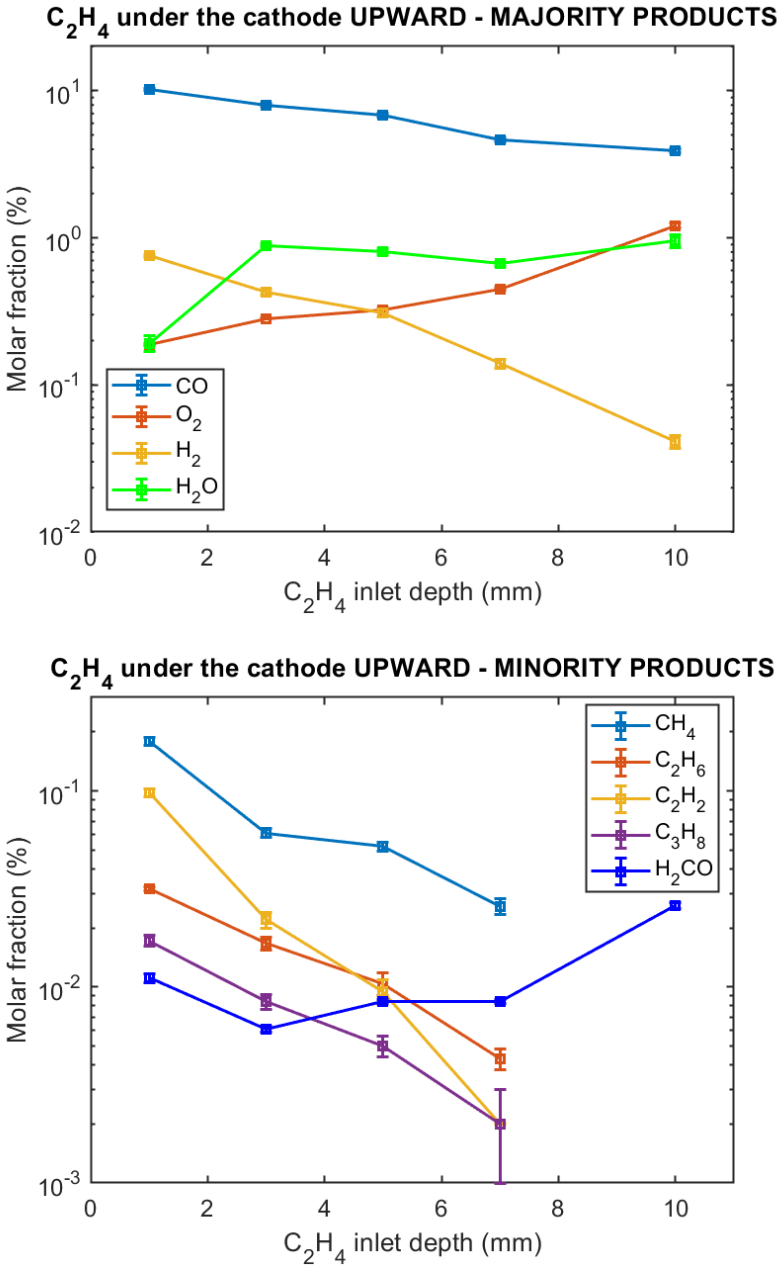

Figure 2.9: Majority and minority products molar fractions for ethylene addition under the cathode upward vs C_2H_4 inlet depth.

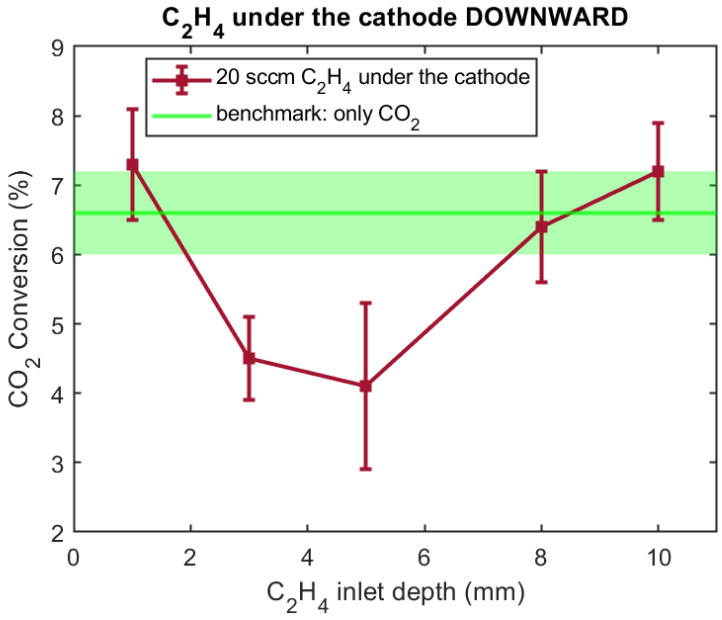

Figure 2.10: CO_2 conversion vs C_2H_4 inlet depth in the case of 2 kHz pulsing frequency, 200 sccm CO_2 and 20 sccm C_2H_4 added under the cathode with downward flow. The green area represents the CO_2 conversion without ethylene addition and its uncertainty.

tion directly in the reactor together with CO_2 is also represented in the graph by the red area. $C_{C_2H_4}$ increases as ethylene is added closer to the cathode, and $\sim 50\%$ is converted when it is added with upward stream 1 mm below the cathode. The downward flow drastically reduces its conversion with respect to the upward case. The farthest ethylene addition downward results in a almost null $C_{C_2H_4}$. When it is added directly in the discharge, ethylene conversion is much higher, with a value of 63.6±0.9 %. It is important to remember that the two sets of measurements also refer to different ethylene flows (10 and 20 sccm respectively), CO_2 flows (100 sccm and 200 sccm respectively) and pulsing frequencies (1 kHz and 2 kHz respectively), although the resulting SEI is similar and the gas mix ratios are the same.

The products of the process with ethylene added downward are presented in the graphs of fig. 2.12. For C_2H_4 addition far from the discharge zone the products are typically those of the simple CO_2 plasma without ethylene addition: for inlet depths of 8 and 10 mm, CO and O_2 tend to the proportion 2:1 as in the pure CO_2 case, while all the other products tend to decrease or completely disappear. Adding ethylene closer to the discharge, CO production firstly decreases, consistently with the lower CO_2 conversion, while for 1 mm inlet depth it increases to values higher than the CO_2 conversion, since it is produced not only from the dissociation of CO_2 but also from C atoms from ethylene. At the same time, O_2 monotonically

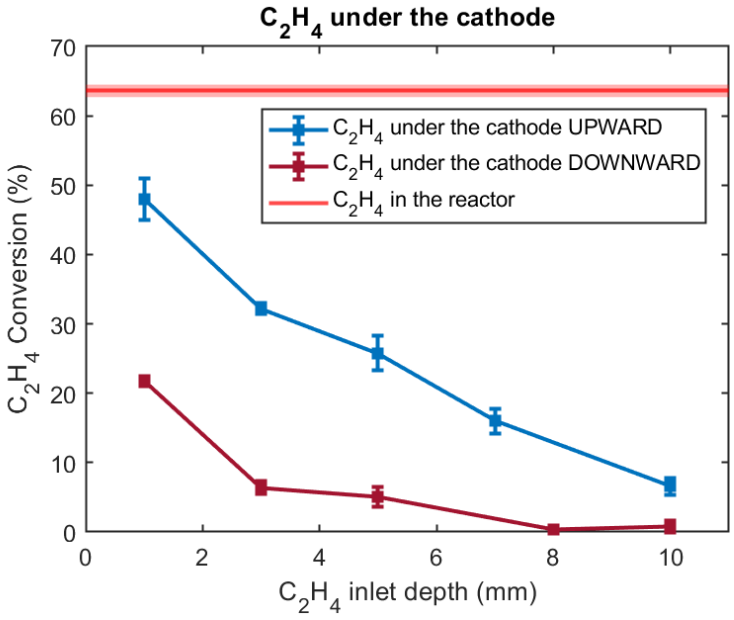

Figure 2.11: C_2H_4 conversion vs C_2H_4 inlet depth under the reactor, with both upward and downward stream. The red area denotes the case of C_2H_4 added directly in the reactor in mixed feed with CO_2.

decreases when C_2H_4 inlet depth decreases, reaching values one order of magnitude lower. The graphs of fig. 2.12 can be qualitatively seen as an extension of those of fig. 2.9 since the ethylene addition downward under the cathode is comparable to a deeper addition upward. Hydrogen and the hydrocarbons (CH_4, C_2H_6, C_2H_2 and C_3H_8) production increases when ethylene is added closer to the cathode or more abundantly in the reactor, although their molar fractions are very small, typically between $\sim 1\%$ and few tens of ppm. Instead, H_2CO molar fraction initially increases for increasing inlet depth, while it also decreases and then disappear for the farthest ethylene addition configurations. Again, no traces of C_2H_4O have been found in the FTIR spectra.

As already mentioned, the effect of adding ethylene under the cathode with a downward stream seams just the same as the upward addition but just shifted down, until the case of the downward addition at 10 mm depth where the presence of ethylene does not affect the process, the C_2H_4 conversion tends to ~ 0 and the products are just those of the simple CO_2 dissociation process.

The doubt persists whether the observed effects are due to processes involving C_2H_4 happening in the plasma or in the region under the cathode where ethylene is injected. To definitely understand whether ethylene is able to enter the discharge zone in the configurations, emission spectra have been acquired from the discharge, in order to check the presence of hydrogen in the plasma, an atom that can only originate from ethylene.

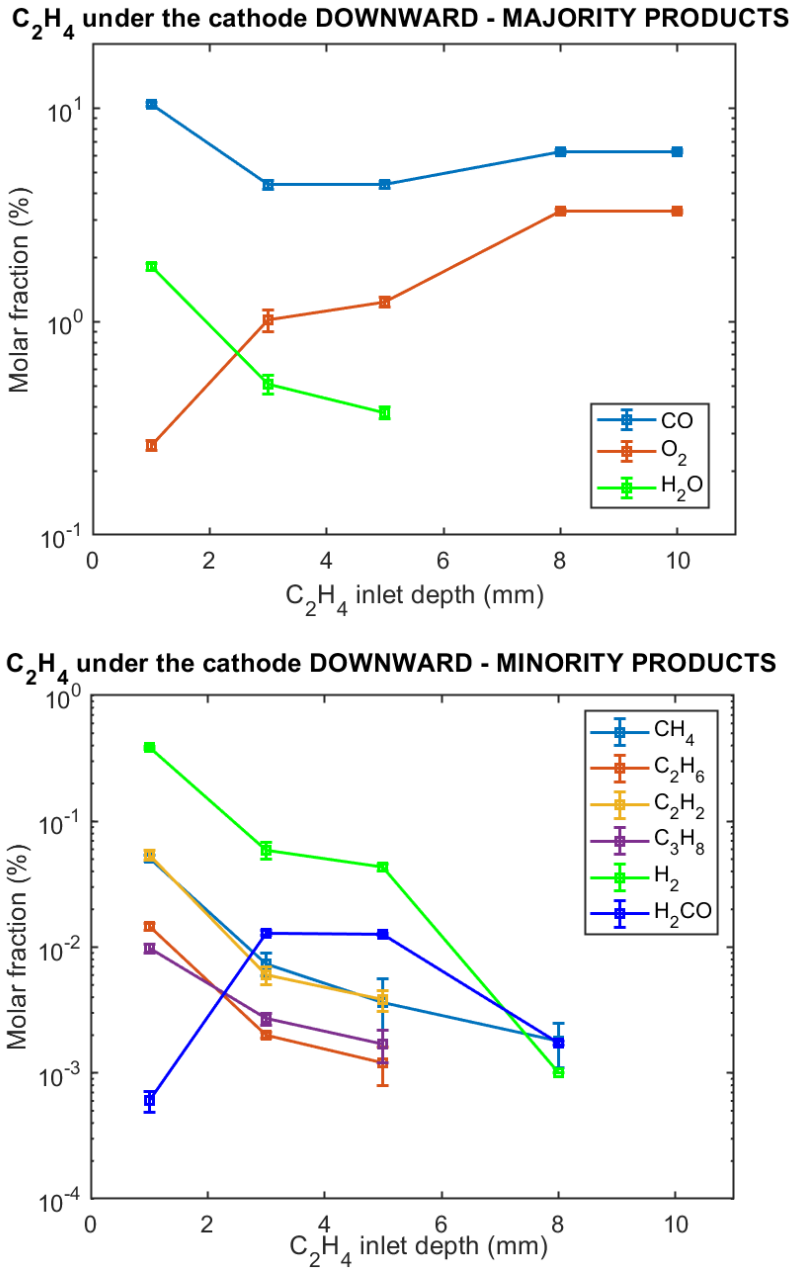

Figure 2.12: Majority and minority products molar fractions for ethylene addition under the cathode downward vs C_2H_4 inlet depth.

2.3.2 Optical emission

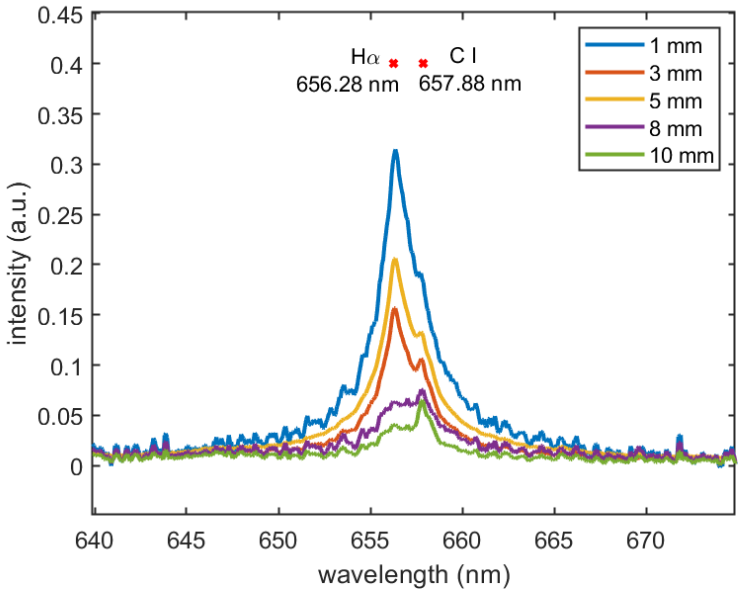

Figure 2.13: Emission spectra of the Hα line for different ethylene addition distances under the cathode.

Figure 2.13 shows emission spectra for 20 sccm C_2H_4 added downward behind the cathode in a discharge with 200 sccm CO_2 and a pulsig frequency f_p=2 kHz. The Hα line at 656.28 nm partially overlap with the 657.88 nm emission of C I.

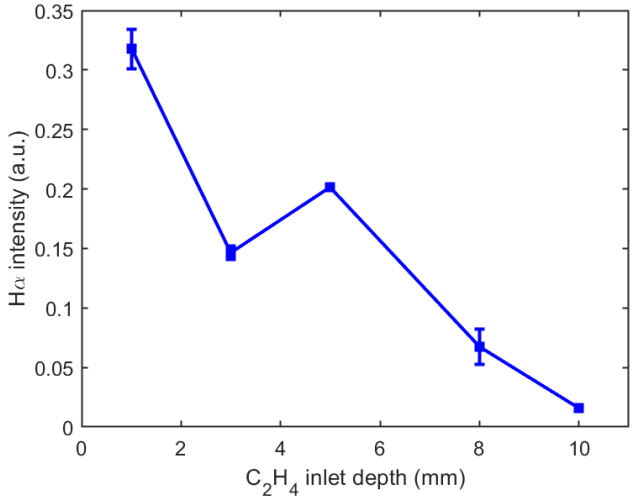

Figure 2.14: Hα emission intensity vs C_2H_4 inlet depth for downward stream.

The intensity of the Hα line is plotted versus the ethylene injection depth in figure 2.14. It decreases for deeper ethylene addition. The local minimum at 3 mm can be explained by the non complete reproducibility of the relative position between the reactor and the optical fiber as mentioned in section 2.2.7. However, the important information obtained from this measurement is that, even for the configuration of deepest ethylene addition, traces of hydrogen are detected in plasma, meaning that part of the injected C_2H_4 enters the reactor counterflow, despite the pressure gradient given by the flows.

Following these findings, we want to investigate the effect of ethylene addition directly in the reactor, in co-feed with CO_2, and reduce the C_2H_4 until almost negligible values relative to the CO_2 stream feed.

2.3.3 C_2H_4 directly in the reactor

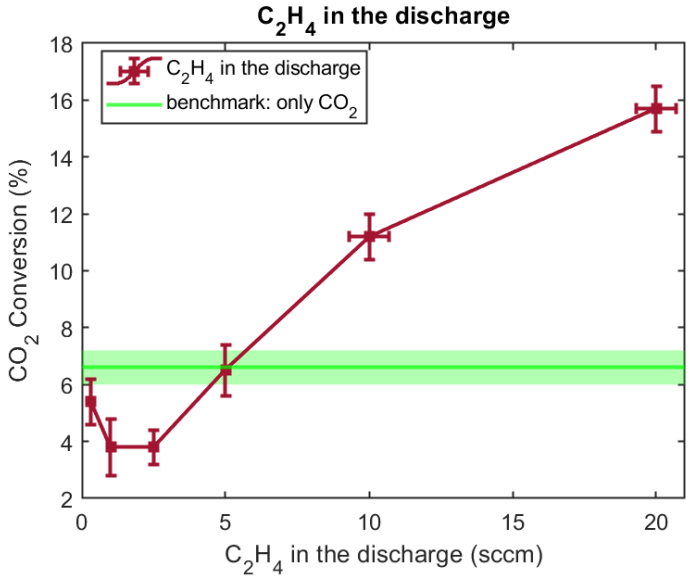

Figure 2.15: CO_2 conversion vs C_2H_4 flow added directly in the reactor, together with 200 sccm CO_2 with a pulsing frequency of 2 kHz.

In this set of measurements, the same CO_2 flow and pulsing frequency of the previous set have been kept, i.e. 200 sccm and 2 kHz, respectively. The C_2H_4 flow has been varied from 20 sccm (the same flow used for injection under the cathode) to 0.3 sccm, corresponding to 15 ppm with respect to the CO_2 flow. In figure 2.15 the results for CO_2 conversion are reported as a function of C_2H_4 flow. The benchmark value is given by the same measurements as for the series of ethylene added downward under the cathode, since the used CO_2 flows and pulsing frequency are the same. For high ethylene flows the CO_2 conversion is again much higher

than the benchmark value. It decreases for decreasing C_2H_4 flows until values much lower than the benchmark and raises again towards the only CO_2 reference when the amount of ethylene in the mixture is almost negligible with respect to the CO_2 one.

These measurements confirm a non-monotonic behaviour of the CO_2 conversion as function of both ethylene flow in the discharge or ethylene inlet depth, sweeping from values higher ($\sim$ twice) to lower ($\sim$ half) with respect to the case of CO_2 splitting in absence of C_2H_4.

The ethylene conversion is shown in figure 2.16. The measurement with 100 sccm of CO_2, 10 sccm C_2H_4 and $f_p = 1$ kHz is also reported in the plot. When it is added directly in the discharge, ethylene conversion is higher than when added under the cathode, and it increases for decreasing fluxes, since the plasma is able to convert almost completely the small amounts of C_2H_4. The mixtures 10 C_2H_4 - 100 CO_2 and 20 C_2H_4 - 200 CO_2, with the same reactants ratio at the same SEI, give quite similar ethylene conversions.

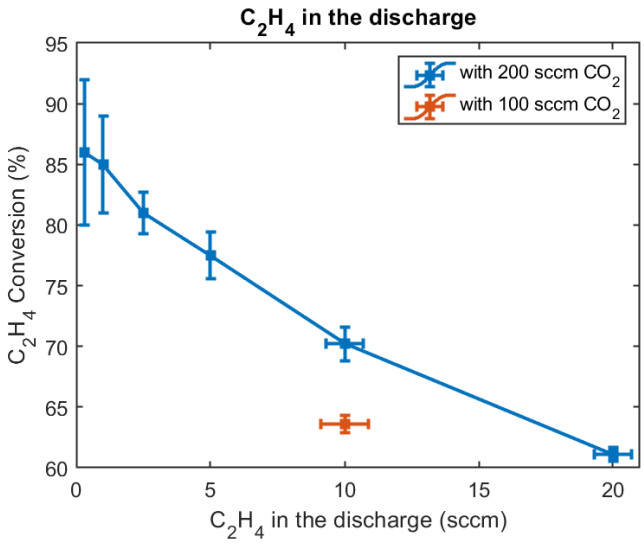

Figure 2.16: C_2H_4 conversion vs C_2H_4 flow added directly in the reactor.

The molar fractions of all the products for ethylene addition directly in the reactor are plotted in the graphs of figure 2.17. We can observe that in the conditions closer to that of pure CO_2 splitting in absence of ethylene, i.e. those where C_2H_4 is added in small quantities in the reactor, the products are typically those of the CO_2 plasma. Indeed, for lowest ethylene flow, CO and O_2 tend to the proportion 2:1 as in the pure CO_2 case and the molar fraction of all the other products tend to decrease or completely disappear. Hydrogen and the hydrocarbons (CH_4, C_2H_6, C_2H_2 and C_3H_8) production increases when ethylene is more abundant, although their molar fractions are very small, typically between $\sim 1\%$ and few tens of ppm.

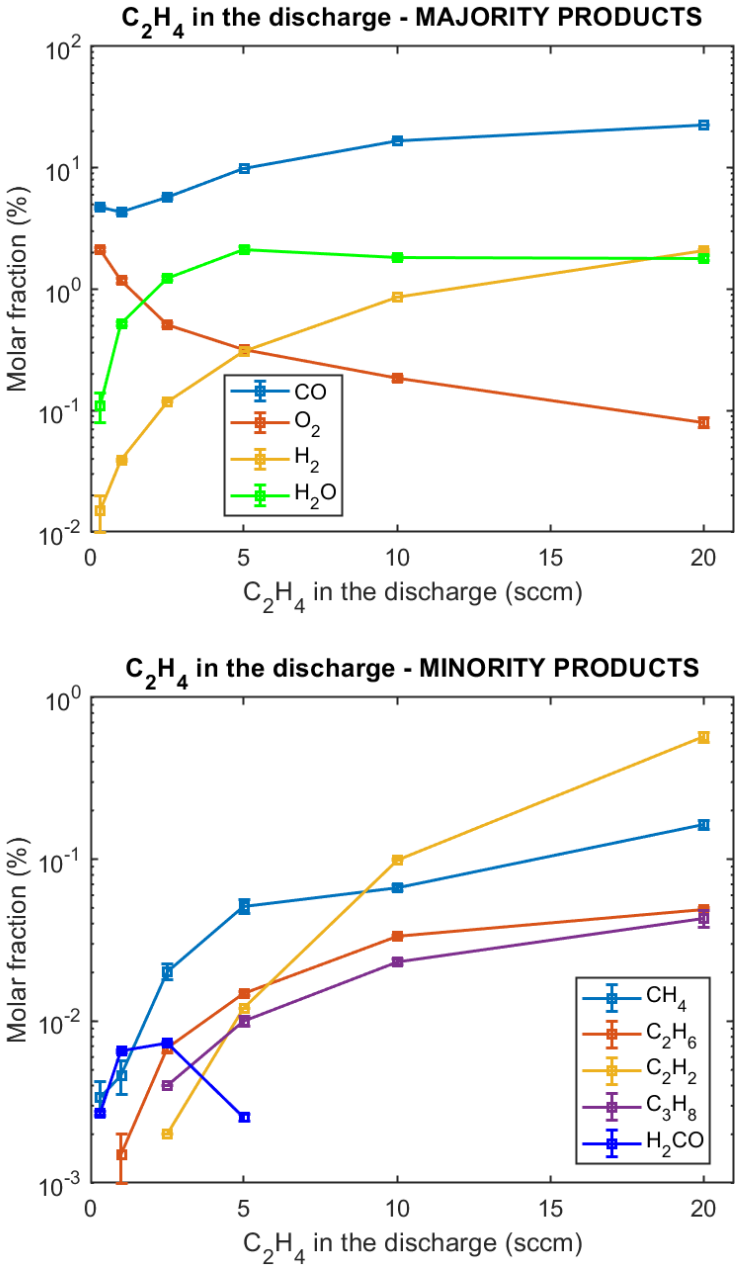

Figure 2.17: Products molar fractions for ethylene addition directly in the reactor vs C_2H_4 flow.

It can be observed that, among the hydrocarbons, C_2H_2 has the most steepest dependence on the ethylene flow, with variations of many orders of magnitude. The same can be noticed for ethylene injection under the cathode upward (see fig. 2.9). On the other hand, H_2CO and H_2O increase when less ethylene is present in the discharge or close to it, and then decrease when C_2H_4 concentration is too low or it is added too far from the discharge.

2.3.4 Selectivities

The most remarkable results for the selectivities are shown in the following graphs, while the others are reported in appendix A.

The graphs of figure 2.18 shows the selectivities of O on both CO (S^O_{CO}) and O_2 ($S^O_{O_2}$) in the three different sets of measurements. O_2 production is strongly inhibited when ethylene is introduced close to the reactor or in high flows in co-feed with CO_2, while the oxygen atoms predominantly participate in the formation of CO. When increasing the C_2H_4 injection distance or decreasing its flow in the reactor, S^O_{CO} and $S^O_{O_2}$ progressively tend to the levels of classic CO_2 dissociation.

The selectivities of C on the hydrocarbons (CH_4, C_2H_6, C_2H_2 and C_3H_8) are reported in the graph of 2.19. All their selectivities increase for ethylene injection closer to the cathode and higher flow in the reactor in mixed-feed with CO_2. Acetylene (C_2H_2) is the product with stronger dependence from the C_2H_4 addition configuration and flow. A similar behaviour is observed for H selectivities on C_2H_6, C_2H_2 and C_3H_8 (see fig. A.4 in appendix A), while $S^H_{CH_4}$ (fig. A.5) is not monotonic and less dependent on ethylene injection configuration.

$S^H_{H_2}$ also decreases for deeper C_2H_4 addition and C_2H_4 flow in the reactor, as shown in the graphs of figure 2.20.

Conversely, $S^H_{H_2CO}$ (fig. 2.21) tends to increase when ethylene is less abundant in the plasma, i.e. for lower streams in the reactor or farther injection from the discharge zone. Then it decreases for the farthest C_2H_4 addition under the cathode downwards, but still increases for the lowest ethylene flow in the reactor. Indeed, although H_2CO molar fraction decreases for 0.3 sccm of C_2H_4 (cf. fig. 2.17), $C_{C_2H_4}$ is high (cf. fig. 2.16) and the majority of the hydrocarbons are no more produced, so H_2CO is one of the few products containing H in this configuration. On the other hand, $S^O_{H_2CO}$ (fig. A.1) and $S^C_{H_2CO}$ (fig. A.3), with similar behaviour to $S^H_{H_2CO}$, finally decrease for low ethylene flow in the reactor, because C and O atoms, much more abundant in the mixture than H atoms, primarily go in the main products, i.e. CO and O_2.

Finally, $S^H_{H_2O}$ (fig. 2.22) also increases for deeper ethylene addition and lower streams, followed by a decrease towards values ~ 0 for too far or too low ethylene flows. $S^O_{H_2O}$ shown in figure A.2 in appendix A has a similar behaviour. For ethylene addition under the cathode downward, H_2O production and selectivities decrease for increasing distance from the reactor, meaning that the resulting reduced entrance of C_2H_4 in the plasma zone inhibits the H_2O formation processes.

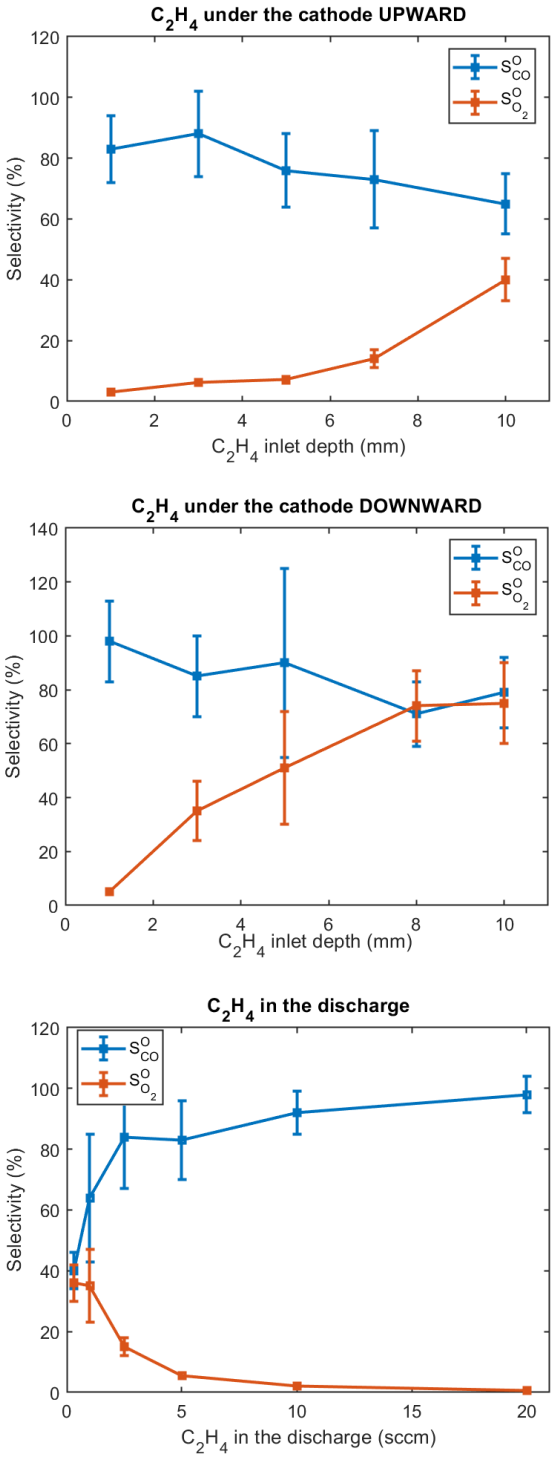

Figure 2.18: Selectivities of O on CO and O_2 in the different ethylene addition configurations.

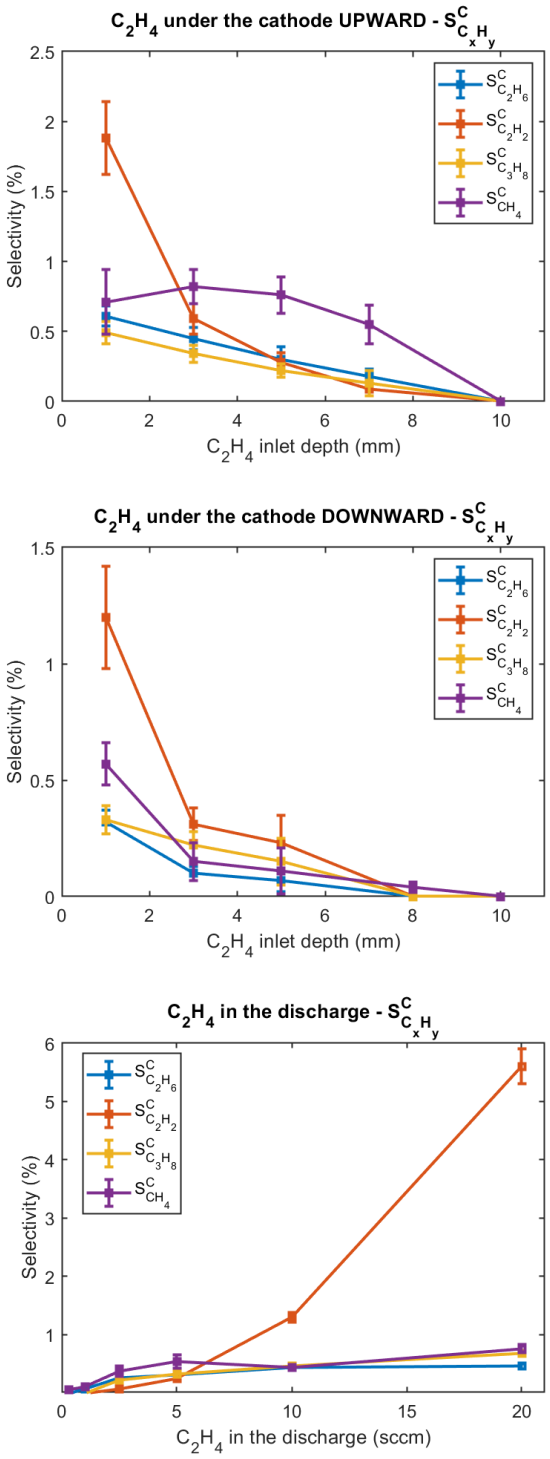

Figure 2.19: Selectivities of C on C_2H_6, C_2H_2, C_3H_8 and CH_4 in the different ethylene addition configurations.

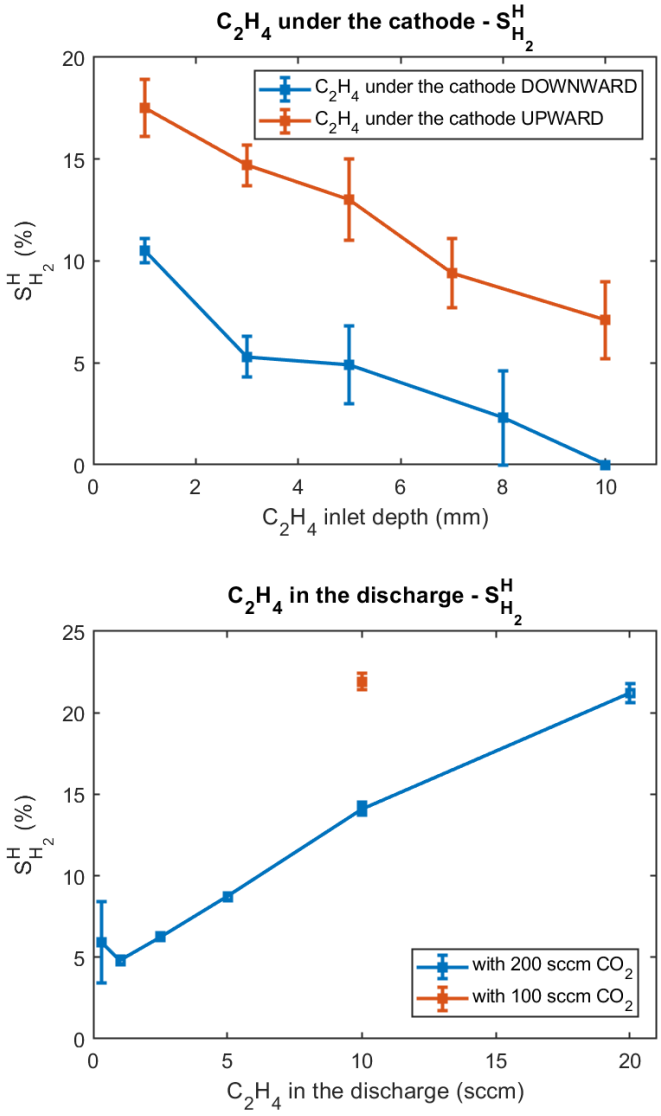

Figure 2.20: $S^{H}_{H_2}$ in the different ethylene addition configurations.

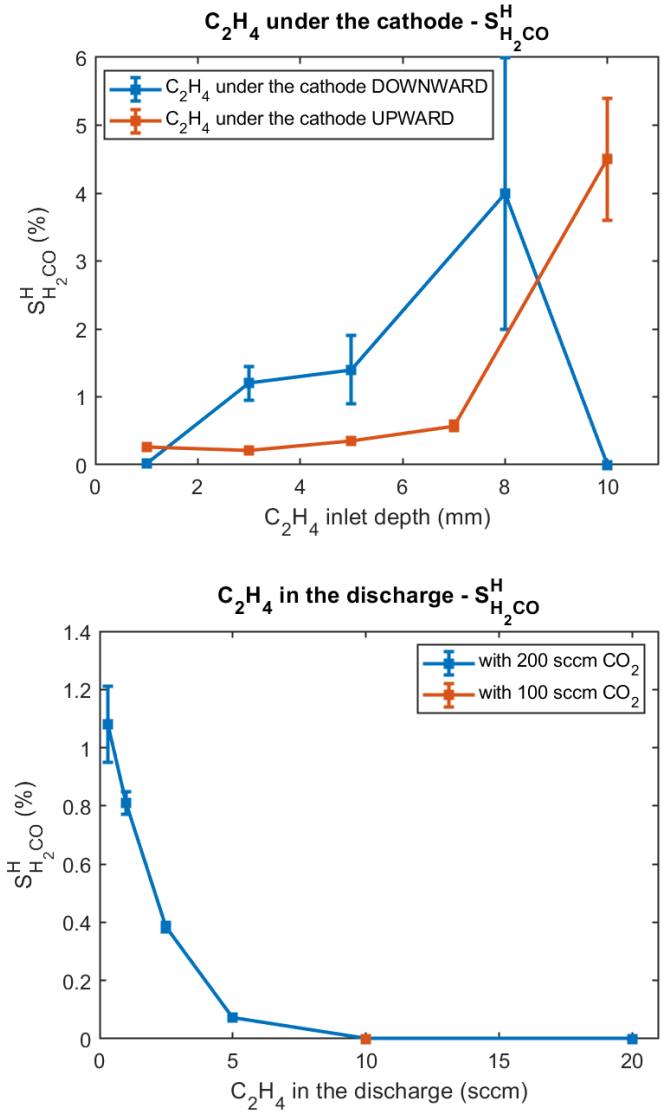

Figure 2.21: $S^{H}_{H_2CO}$ in the different ethylene addition configurations.

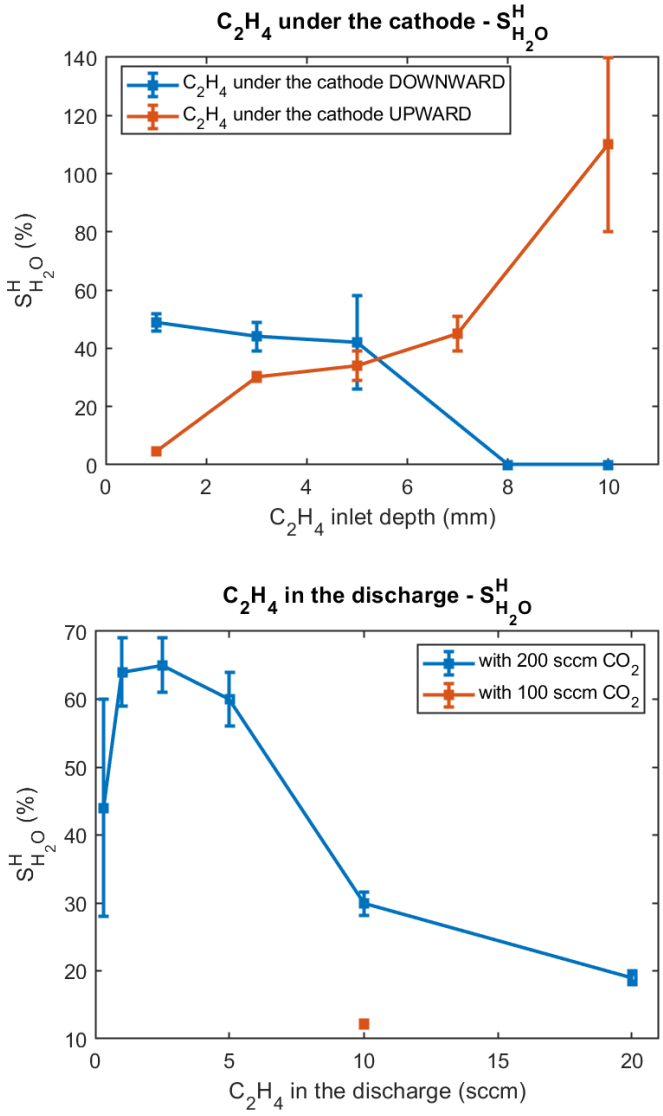

Figure 2.22: $S^{H}_{H_2O}$ in the different ethylene addition configurations.

2.3.5 Balances

The balances of C, O and H are reported in figure 2.23 for the different configurations of ethylene addition.

In some measurements, the C and O balance result >100%. This is probably due to a slight overestimation of CO and O_2 molar fractions from the calibration of the μGC.

On the other hand, a lack of H is evident in the majority of the measurements,

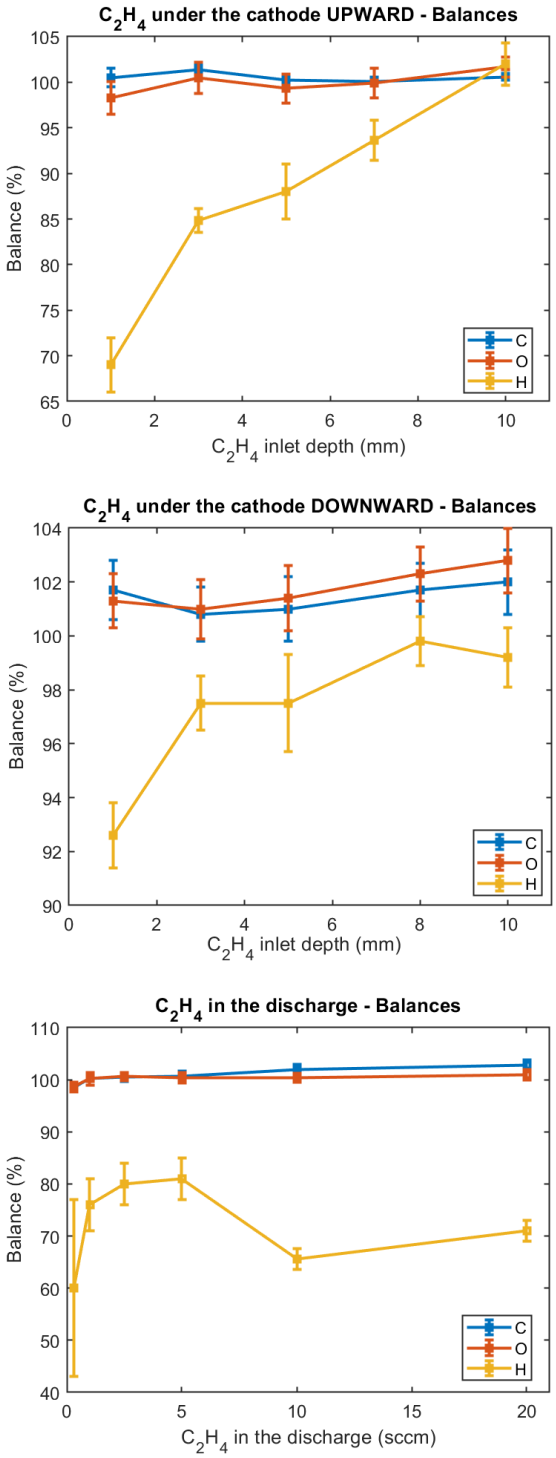

Figure 2.23: Balances of C, O and H in the different ethylene addition configurations.

accentuated for configurations of ethylene abundance. It is probably due to the deposition of hydrocarbon powders and to the condensation of some H_2O on the paper filter placed downstream the reactor, that indeed have been noticed after some measurements with high ethylene stream in the reactor or addition close to the cathode. Since the amount of H atoms coming from the streams of reactants is less than C and O, the lack of these latter species corresponding to the formation of solid or liquid products together with H would be less evident and could be compensated by the above mentioned overestimation of CO and O_2 in the μGC measurements.

2.4 Similar cases in literature

A similar behaviour to the observed non-monotonic CO_2 conversion varying the ethylene addition has been found in a recent work from Baratte et al. [68]. They performed in-situ FTIR spectroscopy in a glow discharge in CO_2 and CH_4 varying the CO_2:CH_4 mixing ratio between 100:0 and 60:40, and simulated the results by modeling. They observed a peak in the CO_2 concentration at the 92:8 CO_2:CH_4 mixture ratio and deepened the examination of the phenomenon by means of a model to understand the underlying chemical mechanisms at play (see fig. 2.24).

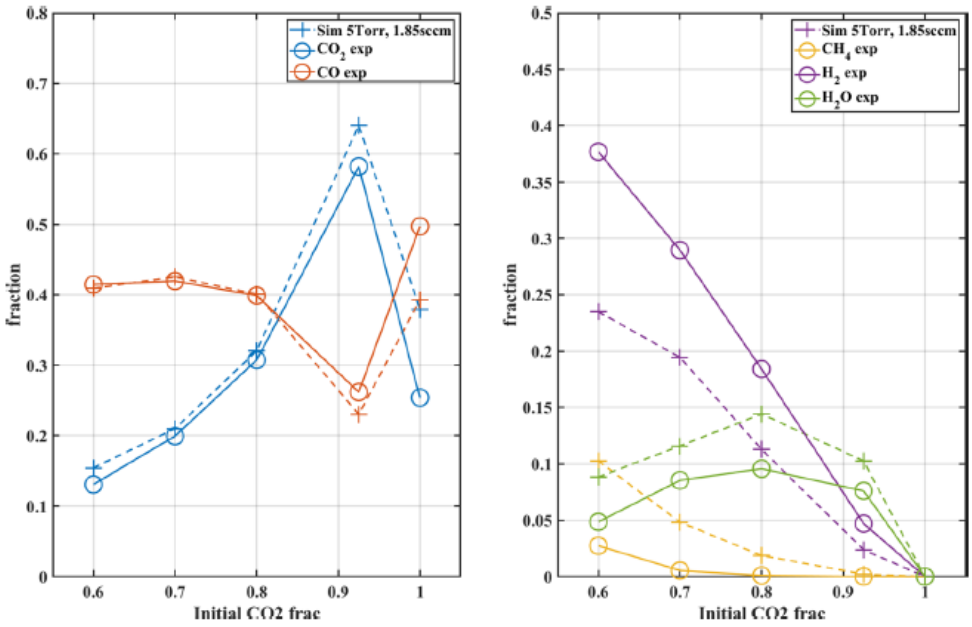

Figure 2.24: Simulation (dashed line) and experiment (plain line) of main species fraction for CO_2:CH_4 mixture variation. Figure reported from [68].

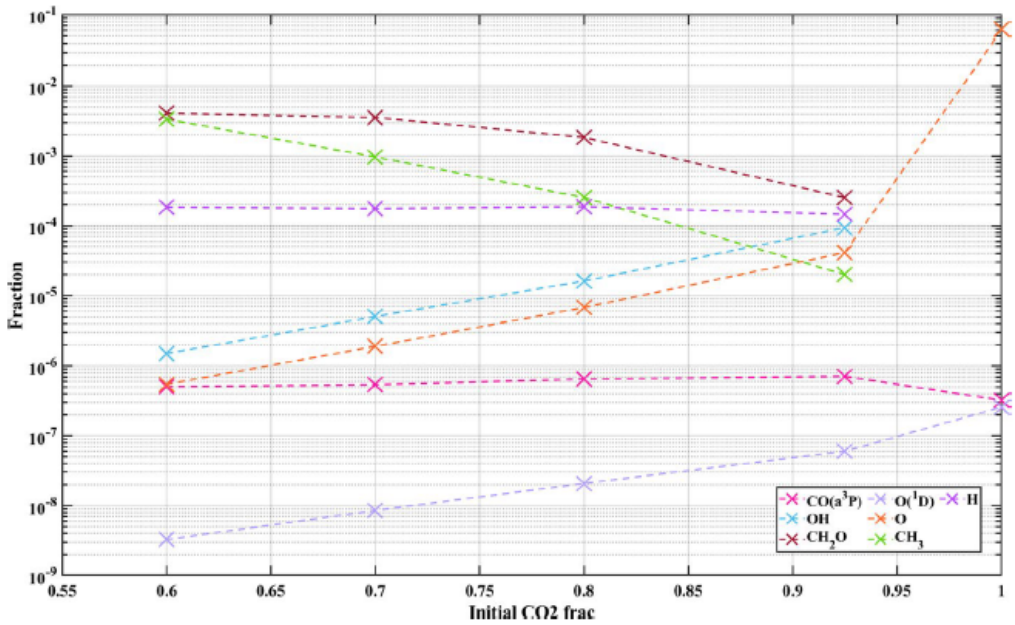

Figure 2.25: Evolution of the simulated fractions of minor species with initial CO_2:CH_4 ratio. Figure reported from [68].

CO_2 is mainly dissociated by electron impact reactions, while interactions with $CO(a^3\Pi)$ species contribute to further dissociation. When CH_4 is present, CH_2 radicals react with CO_2 to form H_2CO and CO.

However, a critical back-reaction between CO and OH proves to be the key to understanding the non-monotonic behavior observed in the system.

$$CO + OH \rightarrow CO_2 + H \tag{2.31}$$

When CH_4 is first introduced into the system, it creates a source of hydrogen atoms. These hydrogen atoms participate in various reactions, leading to the formation of OH radicals. At the specific mixture ratio of 92:8, the system achieves the highest concentration of OH radicals. This creates ideal conditions for the back-reaction between CO and OH, maximizing CO_2 reformation at this particular ratio.

As the CH_4 content increases beyond this optimal ratio, the delicate balance begins to shift. The availability of oxygen atoms for OH formation decreases (see fig. 2.25), leading to a decrease in the back-reaction 2.31, explaining the subsequent drop in CO_2 concentration at higher CH_4 ratios.

Changing other parameters in their plasma and models, they observed that this behavior persists across different pressures and flow rates, suggesting it is an intrinsic characteristic of the chemical system rather than an artifact of specific operating conditions.

They also observe a maximum in H_2O production similar to ours, for the 80:20 CO_2:CH_4 mixing ratio. Conversely, in their work the H_2CO monotonically increases for increasing methane.

According to their model, among the H_2O formation mechanisms, the pathway

$$H_2CO + OH \rightarrow H_2O + HCO \tag{2.32}$$

is of particular interest due to its non-monotonic behaviour, which shows a maximum at the 80:20 CO_2:CH_4 mixing ratio. This peak arises from the opposing trends in OH and H_2CO concentrations: OH density decreases with increasing CH_4 content, while H_2CO concentration shows an inverse relationship (see fig. 2.25).

The comparison of our results with those of this work suggests that similar processes could happen in our plasma when C_2H_4 is added in different quantities and configurations.

2.5 Conclusions and future perspectives

The main limitation to CO_2 dissociation is related to the back-reactions that recombine CO with oxygen. This work explores novel approaches to utilize reactive oxygen species, potentially transforming a limitation into an efficiency enhancement opportunity. Indeed, rather than viewing atomic oxygen as an unwanted byproduct, it represents a highly reactive radical species with potential applications.

Inspired by the work of Xu et al. [56], who obtained an enhancement in CO_2 conversion in RF plasma jets through simultaneous alkene epoxidation with the discharge-generated atomic oxygen, we attempt the same approach in our NRP discharge. We introduced C_2H_4 in the post-discharge to facilitate interaction with plasma products while maintaining their reactivity, without direct plasma exposure. The target product, ethylene oxide (C_2H_4O), represents a valuable industrial chemical with widespread applications, across plastics manufacturing and healthcare sectors.

Systematic variation of ethylene injection distances was implemented to characterize plasma-generated radical lifetimes. Although ethylene oxide formation was not detected, significant effects on CO_2 conversion were observed, with a non-monotonic behaviour and values from much higher to much lower with respect to the CO_2 conversion obtained in the same conditions without ethylene addition.

To investigate potential ethylene contamination in the discharge zone, optical emission spectroscopy was employed to detect the Hα line, an indicators of hydrogen presence in the plasma from C_2H_4. Spectral analysis revealed persistent hydrogen traces across all injection configurations, suggesting that the NRP discharge-induced pressure wave may overcome pressure gradients designed to prevent upstream ethylene migration. This observation has significant implications for fluid dynamics understanding and reactor design optimization in NRP systems.

Complementary experiments involving direct CO_2-C_2H_4 mixed feed streams, with ethylene concentrations up to 10% of CO_2 flow, demonstrated effects analogous to varied-distance post-discharge addition.

Similar phenomena were reported in a recent work by Baratte et al. [68] in CO_2-CH_4 glow discharge systems varying mixing ratios, where CO_2 conversion exhibited a non-monotonic behaviour with methane addition. Their modeling suggested that the back-reaction

$$CO + OH \rightarrow CO_2 + H \tag{2.33}$$

is enhanced for low CH_4 initial concentration, due to a maximum in OH production.

The possibility of analogous mechanisms in our system warrants further investigation through spectroscopy and modeling. Since OH radical could have a key role in the processes, Laser Induced Fluorescence (LIF) spectroscopy could be used to detect its presence in the plasma with high temporal and spatial resolution. Experiments of LIF spectroscopy on OH could be performed in CO_2-C_2H_4 plasma with varying ethylene flow both in our NRP discharge and in glow discharges similar to the one of [68], where both spectroscopy and modeling are easier thanks to the uniformity of the plasma [20].

Chapter 3

Back Current Shunts

In plasma processes, accurately estimating electrical characteristics such as voltage, current, and the energy deposited is crucial. These parameters are necessary for correctly evaluating energy efficiency, which is essential for comparing results with other experiments or methodologies. When the excitation voltage applied to the reactor is composed of pulses of time duration on the order of 10 ns or lower, the measurement of the voltage drop across the plasma reactor becomes not trivial. We will discuss the issues related to commercial probes and have a look to alternative methods with a special focus on Back Current Shunts (BCS). The implementation of this technique, its characterization and applicability to our kind of discharge is then discussed.

3.1 The energy calculation issue

Measuring electrical characteristic of a high voltage signal can become challenging when the pulse duration is in the order of few nanoseconds. In the frequency domain, fast rising or trailing edges correspond to high frequencies and short wavelengths comparable to the physical size of the system. Hence, the lumped circuit approximation is not valid: the whole system behaves like a transmission line and when an impedance mismatch occurs (in the plasma, electrodes, generator or cables), pulse energy is reflected back and forth [55].

The properties of the pulses generated by the Megaimpulse NPG-18/3500 are:

- 18 kV max voltage on matched load
- 40 kV max voltage on open load
- FWHM < 10 ns
- rise time < 4 ns

This means that the signal has frequency components up to ~ 100 MHz.

The most common method to calculate the energy deposited into the plasma is measuring time-resolved voltage and current signals using high-voltage probes and current transformers, respectively, and integrate their product according to

$$E_{pulse} = \int V(t) \cdot I(t + \tau)dt \tag{3.1}$$

where τ is a spurious delay due to several factors: different length of the cables, spacing between voltage and current probes, amplification stage of the oscilloscope and compensation circuit of the HV probe. It is important to correctly take into account this delay when the energy of the pulse is calculated: since the timescale of the pulses is in the order of nanoseconds, a minimal shift of one signal with respect to the other has a huge effect on their product. The calculation of τ is illustrated in section 3.5.

To measure nanosecond HV pulses, a probe should have:

- a wide bandwidth (i.e. low parasitic capacitance);
- a high maximum voltage input (i.e. high input resistance and adequate isolation).

These are requirements that cannot be completely fulfilled at the same time: an adequate isolation asks for bulky dimensions, while a low parasitic capacitance request small dimensions. Thus, a compromise is necessary.

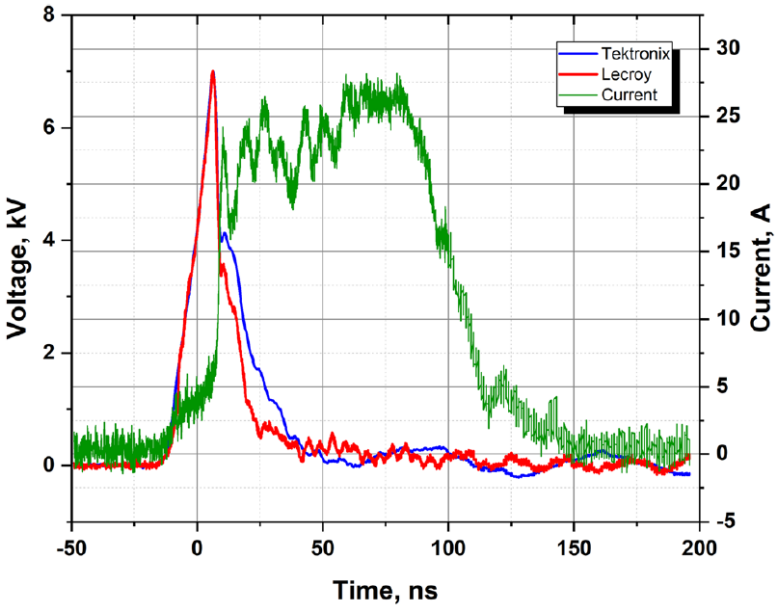

Figure 3.1: Comparison of a NRP voltage signal measured by the probes Tektronix P6015A and LeCroy PP066. The current signal is also displayed. Figure reported from [55].

The most suitable commercially available high-voltage probe is the Tektronik P6015A. It has a maximum voltage input of 40 kV and a bandwidth of 75 MHz, with an input resistance of 100 MΩ and a parasitic capacitance ~ 3 pF. The main effect of this not-negligible parasitic capacitance is evident during the discharge's breakdown, when the voltage between the two electrodes rapidly drops [55]. The probe is not able to follow this drop rate, so it overestimates the voltage in this critical instant when the current rapidly increases and the majority of the energy is deposited in the plasma. This is shown in figure 3.1, where the voltage measurement in a NRP discharge performed with the Tektronix P6015A is compared to that of a LeCroy PP066, a probe with wider bandwidth but lower maximum input voltage. Hence, the pulse energy calculated using equation (3.1) will be overestimated. Furthermore, the parasitic capacitance sinks a spurious current in the system that, due to the huge $\frac{dV}{dt}$, is comparable to the discharge current.

Current probes are less problematic since usually current transformers have nominal bandwidths of hundreds of MHz. The one that we use is a current transformer Magnelab CT-C1.0-BNC with a band from 200 Hz to 500 MHz, large enough for our purposes.

3.2 Alternative methods

Commercial HV probes have intrinsic characteristics that do not allow high frequency measurements. For high voltage and high frequency pulses, researchers often have to develop their own devices, tailored on their own systems [69]. Among the most used custom probes to measure voltage and current, D-dots and B-dots are fast capacitive and inductive sensor, respectively.

A D-dot, also called V-dot, is a capacitive voltage sensor which is capacitively coupled to the HV electrode. The voltage created by the displacement current is measured and, with a proper transfer function and calibration, the voltage signal is reconstructed. This type of devices can be customized and adapted to different kinds of measurements. For instance, they can be placed in the high-voltage source [70], at the reactor HV electrode [34], or in the middle of the transmission line, assembling it in the coaxial cable, with just small modifications of the cable's outer mesh [69, 71]. The sensor is connected to an oscilloscope through another coaxial cable. An explicative drawing of a D-dot assembled on the transmission line and the equivalent circuit is shown in figure 3.2, where V_{Ddot} is the voltage from the D-dot sensor, V_{HV} is the voltage on the inner conductor, Z_{cable} is the impedance of the cable connecting the device to oscilloscope, C_{Ddot} is the capacitance from the D-dot sensor electrode to the inner conductor and C_{par} is the parasitic capacitance from the D-dot sensor electrode to ground. The resulting transfer function is:

$$H_{Ddot}(j\omega) = \frac{V_{Ddot}}{V_{HV}} = \frac{j\omega Z_{cable} C_{Ddot}}{j\omega Z_{cable}(C_{Ddot} + C_{par}) + 1} \tag{3.2}$$

Similarly, a B-dot is a small loop which is coupled to part of the magnetic

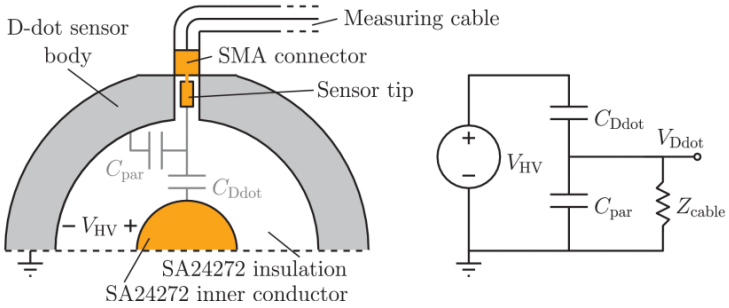

Figure 3.2: A cut-away drawning of a D-dot sensor and its equivalent circuit. Figure reported from [69].

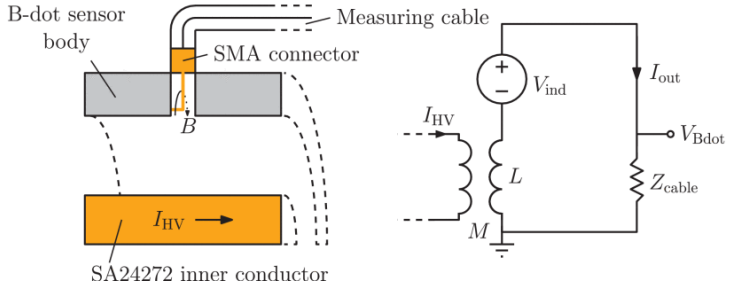

Figure 3.3: A cut-away drawning of a B-dot sensor and its equivalent circuit. Figure reported from [69].

field generated by the pulse as it passes the sensor position [69]. Its scheme and equivalent circuit are shown in figure 3.3, where V_{Bdot} is the voltage from the B-dot sensor, I_{HV} is the current through the inner conductor, V_{ind} is the induced voltage along the B-dot electrode, I_{out} is the current in the B-dot sensor electrode, Z_{cable} is the impedance of the measuring cable, L is the inductance of the B-dot sensor electrode, and M is the mutual inductance between the B-dot sensor electrode and the conductors of the SA24272 cable. The transfer function is:

$$H_{Bdot}(j\omega) = \frac{V_{Bdot}}{I_{HV}} = \frac{j\omega M}{j\omega \frac{L}{Z_{cable}} + 1} \tag{3.3}$$

The same principle but with multiple loops sensor is exploited by the Rogowski coils, which have a similar transfer function as B-dots [70].

These devices are usually much cheaper than commercial probes and can be more accurate. They are also adaptable to fit possible size constraints of a specific system [70]. On the other hand, their calibration can be difficult and in some cases can require extensive modeling because no other sensors with similar properties are available for a comparison. Furthermore, due to their frequency dependent transfer function, they require complicated data postprocessing in the frequency domain and their operation is often limited to a certain regime. Another disadvantage is that they are not able to measure DC [55].

Another technique used in the nanosecond discharge community is the Back Current Shunt (BCS) technique, which allows reaching wide bandwidth while keeping the data processing in the time domain. This method is already used by different research groups [72–74].

3.3 The Back Current Shunts technique

We have seen that HV probes measure in a single point close to the load, perturbing the system [55]. An alternative approach can be pursued by determining the voltage away from the plasma reactor, in the middle of the transmission line (generally a coaxial cable) that connects the electrodes to the nanosecond power supply. The advantage is that we can measure the signal in points where the voltage is lower, so the use of HV probes can be avoided and larger bandwidth can be obtained.

Let us quickly remind the main properties of transmission lines and coaxial cables, which becomes significant in high frequencies and pulsed power applications, when the wavelength is comparable or shorter than the length of the line, i.e. when the lumped-circuit approximation is not more valid and the wave nature of the signal must be taken into account. In a coaxial cable, the current flowing in the outer conductor is equal in magnitude but opposite in direction to the current in the inner conductor, a phenomenon arising from the principle of charge conservation and the cable's cylindrical symmetry. This current distribution maintains the transverse electromagnetic mode of signal propagation, confining the electromagnetic fields within the cable and ensuring minimal radiation losses, thus preserving signal integrity and providing effective electromagnetic shielding. The characteristic impedance of a cable Z_{cable} is the impedance seen by the propagating wave, determined by the physical parameters of the transmission line (e.g. diameters, material properties). It represents the ratio of voltage to current in the wave. Any time a wave encounters a change in impedance as it travels along a transmission line, part of it is reflected back towards the source, to satisfy the boundary conditions at the interface. The amount of reflection is quantified by the reflection coefficient K, which depends on the impedance mismatch:

$$K = \frac{Z_2 - Z_1}{Z_2 + Z_1} \tag{3.4}$$

where Z_1 is the impedance of the line the wave is traveling in and Z_2 is the impedance it encounters. These reflections are unwanted in the majority of applications, since they can cause issues in measurements and signal integrity. However, they are essentially impossible to be removed in pulsed plasmas, since a plasma reactor will hardly be matched to the line impedance. The back current shunts (BCS) technique exploits this reflections and the transmission lines' properties for the measurement of energy deposited in the plasma.

Back current shunts are built by making a small gap in the outer conducting braid of a coaxial cable and replacing it with resistive elements, as shown in figure

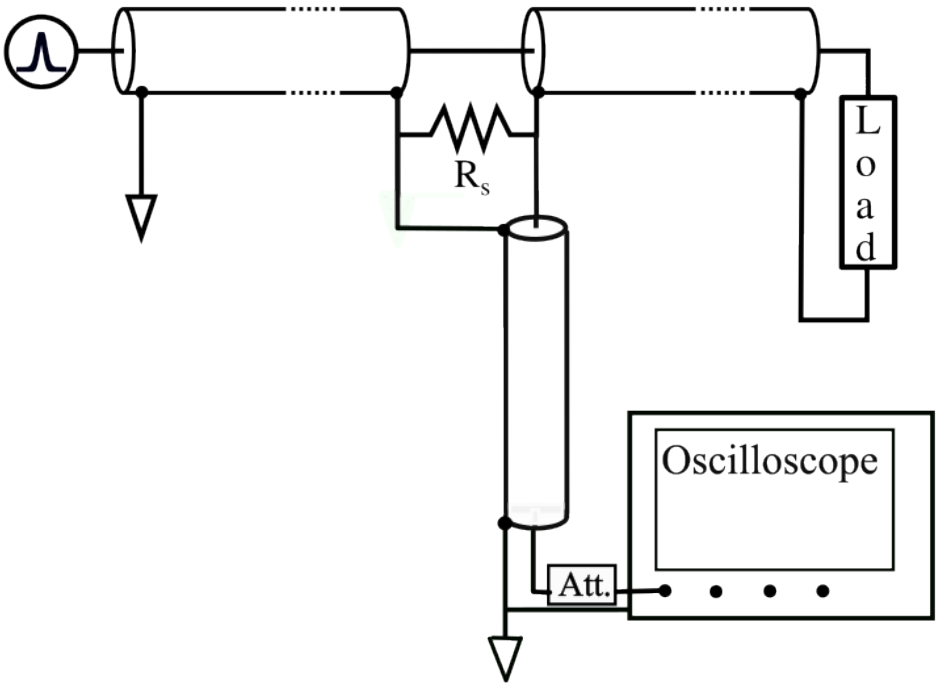

Figure 3.4: BCS circuit scheme.

3.4. The voltage drop across the shunt is measured through a second coaxial cable connected to the oscilloscope, grounded on the side of the generator in order to avoid ground loop and to have a positive signal when a positive peak travels from the generator to the load. When the high voltage pulse propagates in the cable, the current flowing in the shielding of the cable is equal to the current I in the central wire, but with opposite direction. The voltage drop V_{BCS} on the BCS of resistance R_s will be

$$V_{BCS} = I \cdot R_s \tag{3.5}$$

Since the voltage V_{HV} between the central wire and the shielding of a cable of impedance Z_{cable} can be calculated as

$$V_{HV} = I \cdot Z_{cable} \tag{3.6}$$

the measured voltage signal V_{BCS} is proportional to that in the central wire reduced by a factor R_s/Z_{cable}:

$$V_{BCS} = V_{HV} \frac{R_s}{Z_{cable}} \tag{3.7}$$

Measuring the voltage drop across the shunt, we intercept the incident electric pulse followed by its reflections at the load and the generator due to impedance

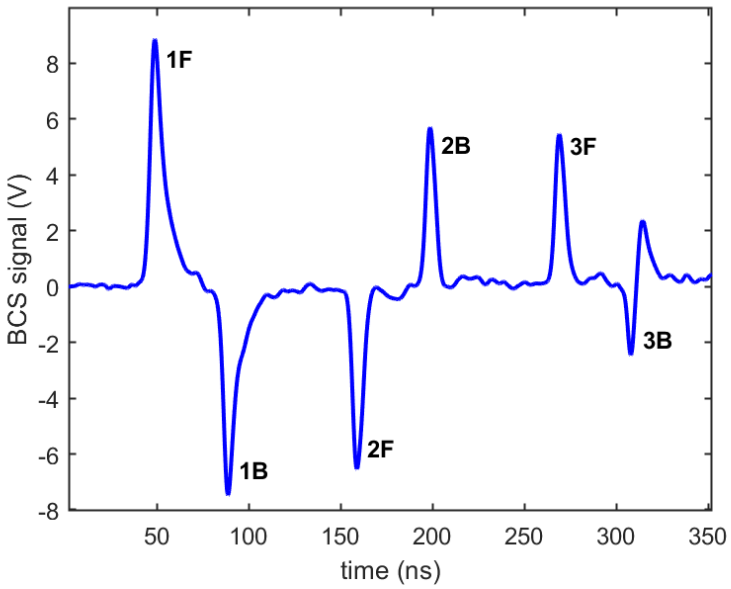

Figure 3.5: Example of BCS singal for a NP discharge. 1F is the 1st forward pulse, 1B is the 1st backward pulse, 2F is the 2nd forward pulse, and so on.

mismatches. The reflection coefficient at the load of impedance Z_L will be

$$K_L = \frac{Z_L - Z_{cable}}{Z_L + Z_{cable}} \tag{3.8}$$

The extreme cases are:

- $Z_L = 0$ and $K_L = -1$, i.e. the signal is completely reflected with opposite polarity;
- $Z_L = \infty$ and $K_L = 1$, i.e. the signal is completely reflected with the same polarity.

The same happens when the reflections travel back to the generator. Our generator behaves like a short circuit after the pulse is generated, so the signal will be completely reflected with inverse polarity. Consecutive pulses with the same sign in the BCS signals actually have different polarities since they move in the opposite direction.

As an example, a BCS signal from a nanosecond discharge in a pin-to-pin plasma cell in air at atmospheric pressure is shown in figure 3.5:

- **1F**: The first positive peak travels from the generator to the reactor. The current on the external mesh is negative, but the BCS is grounded on the side of the generator so V_{BCS} is positive.

- **1B**: The pulse arrives at the reactor, which initially has an impedance much larger than Z_{cable}. The signal is partially reflected toward the generator with the same polarity, but since it travels in opposite direction we see a negative peak in the BCS signal.
- **2F**: The pulse reaches the generator where it is completely reflected with inverse polarity and starts again to travel toward the reactor, producing another negative peak in the BCS signal.
- **2B**: Again, at the reactor the pulse is partially reflected with same polarity and reaches the BCS where a positive peak is registered.
- **3F**: The pulse is again reflected at the generator and travels towards the reactor with positive polarity, so we have same situation as 1F.
- **3B**: At this reflection we notice a change of polarity in the middle of the peak, which denotes a net change in the impedance of the plasma due to the successive pulses, switching from higher than Z_{cable} to lower.

To be able to distinguish the incoming and the reflected pulses in the BCS signal, the time that the signal needs to travel twice the distance L between the BCS and the load must be larger than the width T of the pulse itself. So the length of the cable must satisfy

$$L > \frac{c_{el}T}{2} \tag{3.9}$$

where c_{el} is the velocity of the propagation of the electromagnetic signal in the cable.

$$E_{pulse} = \int \frac{V_{HV}^2(t)}{Z_{cable}} dt \tag{3.10}$$

The difference between the energy of the incident and reflected pulses in the transmission line is equal to the energy deposited in the plasma. Further reflections at the generator must be also taken into account, until they give negligible contribution:

$$E_{deposited} = E_{1,in} - E_{1,ref} + E_{2,in} - E_{2,ref} + ... \tag{3.11}$$

In the calculation of the energy of the pulse it is also important to take into account the attenuation of the cable: the pulse that arrives at the load will be slightly attenuated with respect to when it has been detected by the BCS, while the reflected one that travels back towards the generator was slightly bigger when it left the load area. Since we are interested in what happens at the load, when we perform this calculation we must multiply the incident pulse for the attenuation of the cable and divide the reflected one by the same amount.

3.4 Choice of components and calibration

The resistors' type and characteristics play a crucial role in the measurement. Their properties strongly influence the resulting bandwidth of the device. At high frequencies, the impedance of the resistors is no longer just resistive: parasitic capacitance and inductance start dominating the BCS's response. Hence, the chosen resistors must have very low stray capacitance and inductance. The resulting shunt resistance must be small compared to the HV cable impedance, while the construction itself should keep the cylindrical symmetry and must not significantly disturb the electromagnetic field distribution in the cable. Good practice is to use as many resistors as possible to fill all the free space in the cable ground mesh. Furthermore, the use of many resistors in parallel also extremely reduces the probability that all of them would be damaged simultaneously, leaving the cable's outer shielding open [55].

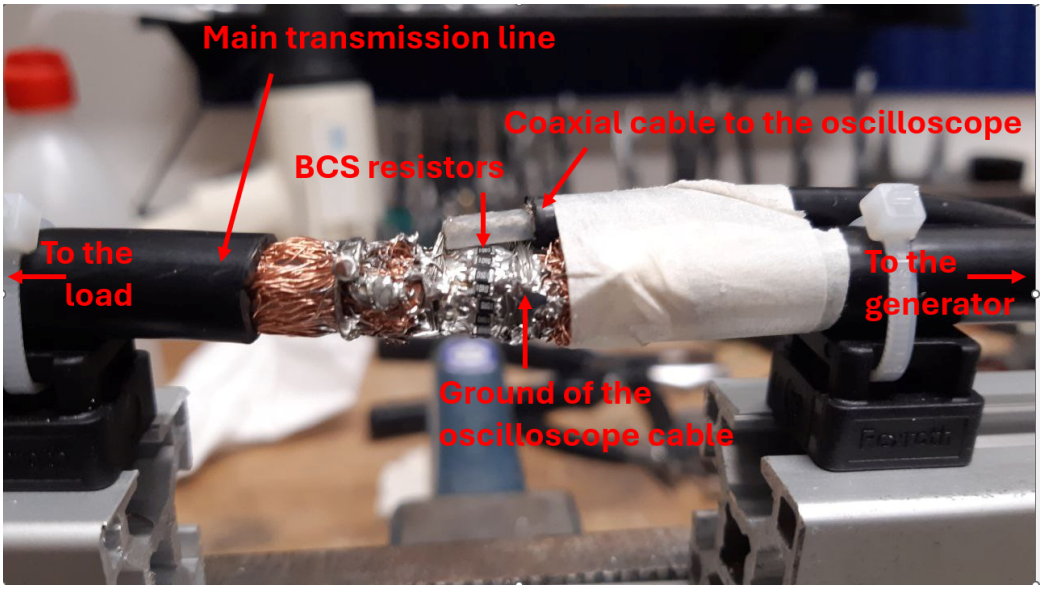

Figure 3.6: Picture of the back current shunt assembled on a coaxial cable.

The used BCS has been built in the middle of a 8 m RG11 cable (Z_{cable}= 75 Ω) using 18 thick film SMD resistors of 10 Ω (YAGEO AC0805FR-0710RL) soldered in parallel, resulting in R_s=0.56 Ω. The 4 m cable between the BCS and the load satisfy eq. 3.9 considering our pulse width T=10 ns and the velocity of propagation in the RG11 which is 66% of the velocity of light. Although a lower value of resistance would have been preferable in order to obtain a lower R_s/Z_{cable} ratio (i.e. higher attenuation) and to perturb less the transmission line, stray capacitance and inductance increase with decreasing resistance value, so 10 Ω resistors have been an acceptable compromise to have a flat behaviour up to the desired frequencies. The physical size of the resistors also plays a role, with

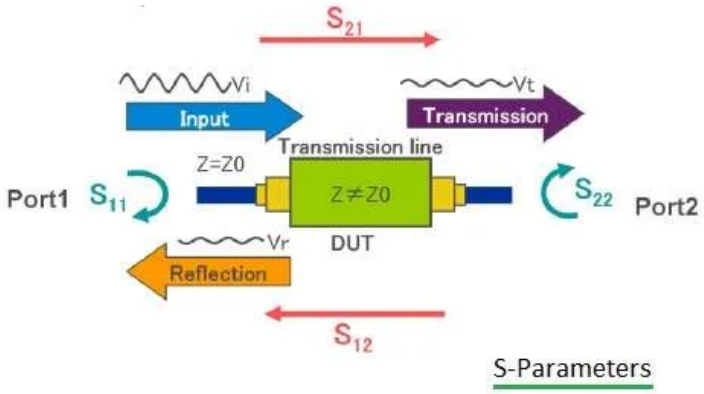

Figure 3.7: Schematic representation of S-parameters on a Device Under Test (DUT) with input connected to port 1 and output connected to port 2. Figure reported from [75].

stray capacitance and inductance increasing with increasing size. They have been chosen as small as possible (with the limit of being manually manageable) also to be able to solder many of them in parallel around the cable, keeping the cylindrical symmetry and obtaining a lower R_s. The ends of the shunt have been connected with a RG58 coaxial cable to acquire the signal through the BCS. The obtained BCS is shown in figure 3.6.

The BCS has been calibrated using a vector network analyzer (VNA) Rohde & Schwarz Vector Analyzer ZPV with Tuner 0.3-2000 MHz ZPV-E3 and a signal generator Agilent 8648C 9kHz-3200MHz.

VNAs are instruments useful for characterizing high-frequency electronic devices and systems. These analyzers measure both the magnitude and phase of signals, providing comprehensive data on the scattering parameters (S-parameters) of a Device Under Test (DUT).

S-parameters describe how RF waves propagate through a multi-port network. They are typically represented as a matrix (S-matrix), which, for a two-port network is, defined as:

$$\mathbf{S} = \begin{bmatrix} S_{11} & S_{12} \\ S_{21} & S_{22} \end{bmatrix} \tag{3.12}$$

where:

- S_{11} is the input port voltage reflection coefficient
- S_{12} is the reverse voltage gain
- S_{21} is the forward voltage gain
- S_{22} is the output port voltage reflection coefficient

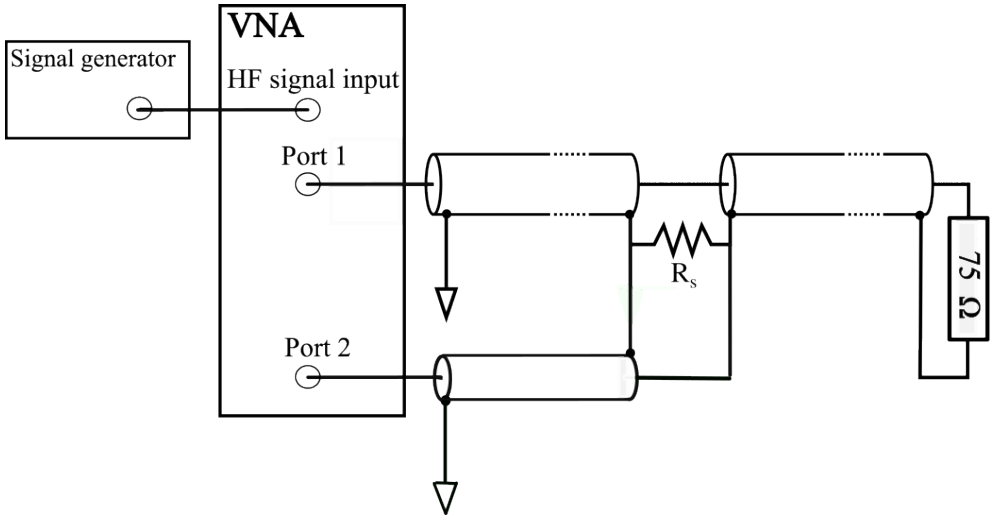

Figure 3.8: Scheme of BCS calibration with VNA.

This is schematically represented in figure 3.7. Each S-parameter is a complex number, representing both magnitude and phase:

$$S_{ij} = |S_{ij}|e^{j\theta_{ij}} \tag{3.13}$$

where $|S_{ij}|$ is the magnitude and θ_{ij} is the phase angle.

The equations that relate the incident (a) and reflected (b) waves at each port (1 and 2) to the S-matrix (S) are given by:

$$\begin{bmatrix} b_1 \\ b_2 \end{bmatrix} = \begin{bmatrix} S_{11} & S_{12} \\ S_{21} & S_{22} \end{bmatrix} \begin{bmatrix} a_1 \\ a_2 \end{bmatrix} \tag{3.14}$$

S-parameters are frequency-dependent: frequency in the VNA is swept across a range of interest to record the variations of the S-parameters. In our instrument, the frequency is manually changed from the signal generator. The signal generator provides a continuous sinusoidal wave with a known amplitude at a known frequency. The VNA transmits this input signal to the input port of the DUT and measures the transmitted and reflected signals at each port, comparing them with the input signal and providing the respective S-parameters.

To calibrate our BCS, the cable where it is assembled is connected to port 1 of the VNA and its end is closed with an 75 Ω resistor. The RG58 cable from the end of the BCS is connected to port 2 (see fig. 3.8). The S-parameter we are interested in for the calibration is S_{21}. The frequency has been varied from 700 Hz to 1 GHz and the measured attenuation has been recorded. The frequency response of our BCS is shown in figure 3.9. It is almost flat up to 100 MHZ, with a value of ∼-41 dB, then it starts decreasing and reaches the band limit (-3 dB) around 500 MHz. The found BCS attenuation slightly differs from the expected one described by eq.

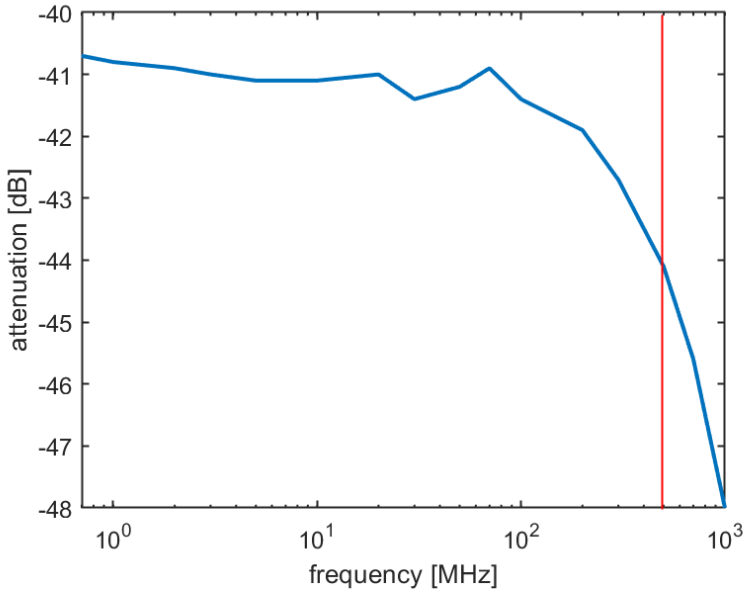

Figure 3.9: Back current shunt's attenuation. The red line marks the -3 dB level.

3.7: indeed $R_s/Z_{cable} = 0.0075$ corresponds to -42.5 dB. This is probably due to not perfect soldering, which results in an enhancement of R_s especially for high frequency signals.

Finally, to test our BCS on HV pulses, further adjustments have been needed. Megaimpulse NP generators have a special type of coaxial connector for the HV output. The company furnishes 3 m long 75 Ω cables (RK-75 type) with the proper connector and recommends to use the generator only with this cables. We had to face the impossibility to buy the same kind of cable in Europe or to assemble the connector to other cables for safety reasons. RG11 is the most similar cable to the RK-75, with the same geometry and impeadance. We performed a junction between the previously calibrated BCS cable (8 m RG11) and a 3 m RK-75 with its proper connector. Thus, the resulting HV cable is 11 m long, with the BCS at 7 m from the NPG and 4 m from the load.

In the following sections, the BCS ends are connected to the 1 MΩ input of the oscilloscope (Teledyne Lecroy HDO 9104 1GHz High Definition Oscilloscope 40 GS/s) through the RG58 cable and 50 Ω BNC attenuators of A_{att}= 26 dB, as shown in figure 3.4. The total attenuation between the signal on the oscilloscope and the HV pulse travelling in the inner conductor of the transmission line is hence given by the attenuation of the BCS of A_{BCS}=41 dB and that of the attenuators A_{att}:

$$V_{HV} = V_{BCS} \cdot 10^{(A_{BCS}+A_{att})/20} \tag{3.15}$$

3.5 Characterization

To obtain an energy measurement from the BCS signal and compare it with that obtained from conventional probes, further characterization of the system with the HV nanosecond pulses is needed. Two different kind of measurements in different configurations are necessary to find some parameters that describe the behaviour of the HV pulses travelling through the cable and the reactor. Useful suggestions for these procedures have been found in [76] and [77].

3.5.1 Short-circuit: cable attenuation

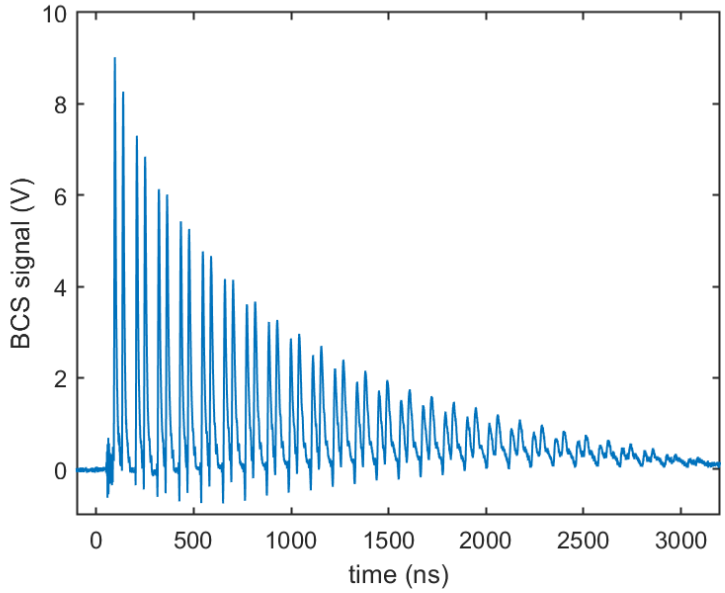

Figure 3.10: BCS signal with 0 load.

First of all we need to know the attenuation of the cable. This has been done by short-circuiting the end of the cable instead of placing the plasma reactor. This means that the impedance of the load is $Z_L = 0$, resulting in a reflection coefficient $K_L = -1$ from equation 3.8, i.e. the pulse reflects completely with opposite polarity but, since it travels in the opposite directions in the transmission line, in the BCS signal (figure 3.10) the reflected pulse will have the same polarity of the incoming one. Since is reasonable to assume that no energy is dissipated in the load, in the signal we can observe many reflections until it gets completely attenuated. From the 6^{th} pair we can observe that the reflected pulses are even higher than the incoming ones: this is due to the fact that high frequencies are more attenuated than low ones, causing dispersion in the voltage signal and broadening of the peaks, so at a certain point the incoming and reflected pulses will not be completely separated

and they add up. This does not affect our measurement since only the first pair is taken into account for the calculation.

The ratio of the amplitudes of the first reflected and the first incoming pulses corresponds to the square of the cable attenuation (k_c) between the BCS and the load, because the HV pulse travels twice that length in both directions between the two detections in the BCS.

$$k_c = \sqrt{\frac{V_{1,ref}}{V_{1,in}}} \tag{3.16}$$

We obtain k_c=0.957±0.007 or -0.38±0.06 dB.

3.5.2 Discharge inhibition

Other important parameters must be calculated through measurements with the inhibition of the discharge. The plasma reactor has been connected at the end of the line and filled with Freon-13 (chlorotrifluoromethane $CClF_3$), a very stable molecule which does not allow the plasma ignition in the configuration of our reactor, which is the same used in the previous chapter for measurements with C_2H_4 (see section 2.2.1).

First of all, in this configuration we can establish the time delay between the incident and the reflected pulses (that will be twice the time for the propagation from the BCS to the load) by superimposing the rising edges of the two pulses. This is essential to reconstruct the voltage signal at the load from the sum of the incident and reflected pulses. We obtain a delay d= 40.75±0.05 ns.

This configuration where the discharge does not take place and no energy is dissipated in the plasma is also useful to account for other losses that happen in the reactor. Ideally, we could think at the reactor filled with freon as a capacitor, with only an imaginary impedance that should just introduce a phase shift, with no energy dissipation, and we could expect all the energy of the forward pulse being reflected back. Actually, other losses can take place at the load due to many factors, e.g. coronas and resistive effects along the reactor materials and the probes, when they are connected. However, since this energy is not dissipated in the plasma, we need to quantify it and take it into account when we perform the energy measurement during the discharge.

These energy losses are strongly affected by the presence of the probes attached at the load. For this reason, three different kinds of measurements have been taken:

- **configuration 1:** simultaneous acquisitions of BCS signal, HV probe and current probe signals;
- **configuration 2:** HV probe has been removed from the system, only BCS and current probe signals are acquired;

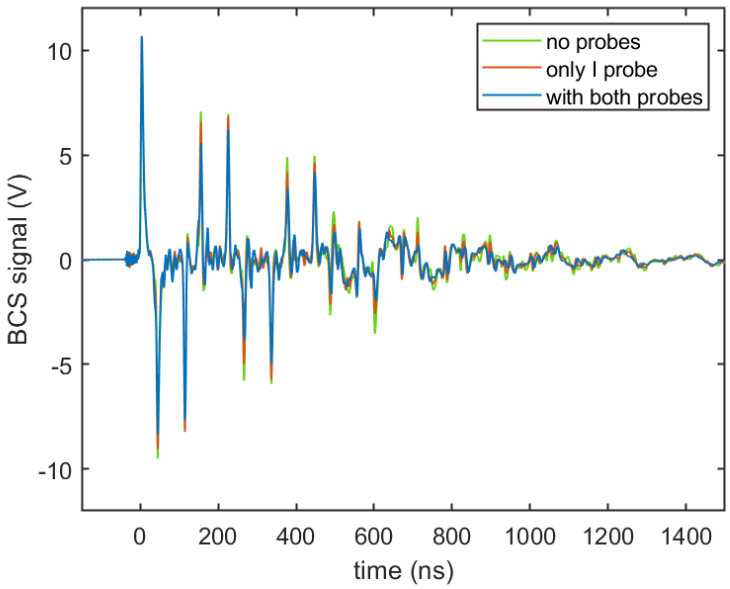

Figure 3.11: BCS signals with freon.

- **configuration 3:** also the current probe has been removed, only BCS signal is acquired.

Figure 3.11 show the resulting BCS signal in the three configurations, and figure 3.12 is a zoom on the first pair. While the incoming pulse is not affected from what happens at the load and is always very similar, the reflections have different shapes in the three cases, with the maximum voltage increasing as we remove the probes. This means that the presence of the probes at the load results in an increase of energy loss.

This is evident also from figure 3.13, that shows a comparison of the first incoming and first reflected pulse in the three configurations. Here the pulses have already been corrected by the cable attenuation coefficient k_c to represent their values at the load.

To take into account the energy loss, we introduce the parameter R_F as the ratio of the energy of the reflected ($E^F_{1,ref}$) and incoming ($E^F_{1,in}$) pulse with discharge inhibition:

$$R_F = \frac{E^F_{1,ref}}{E^F_{1,in}} \tag{3.17}$$

This parameter will then be used to correct the energy of the reflected pulses in the measurements with the discharge to account for a portion of "missing" energy that is actually not dissipated in the discharge but in other ways.

In the three different configurations, the results for R_F are respectively:

- $R_{F1} = 0.837 \pm 0.013$;

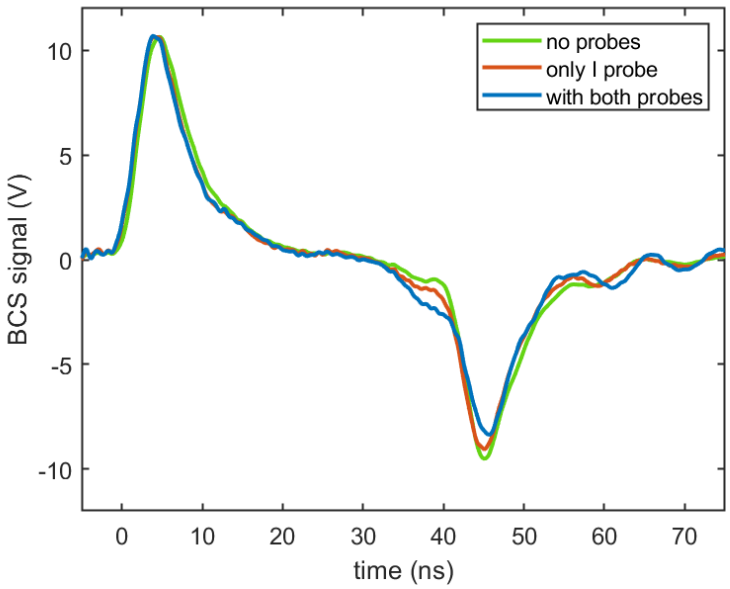

Figure 3.12: First pair of incoming and reflected pulses with freon in the three different configurations

- $R_{F2} = 0.909 \pm 0.014$;
- $R_{F3} = 0.955 \pm 0.014$;

These values are calculated on the first pair of incoming and reflected pulses because it is the one that gives the most significant contribution to the deposited energy. The stated error is statistical among the collected samples. However, for the successive pairs, the error on R_F increases drastically, especially for the case of configuration 1 where the loss is bigger. The next table shows the relative errors for the second and third pairs. Anyway, as will be shown in section 3.7, the contribution to the total energy of the second and third pulses is much lower than the first one, so the errors are still acceptable.

Pair #	R_{F1} error	R_{F2} error	R_{F3} error
2	14%	8%	5%
3	27%	21%	12%

Probes characterization

The measurement with Freon with both the probes connected is also useful to calculate the time shift τ between the voltage and current probes, necessary to

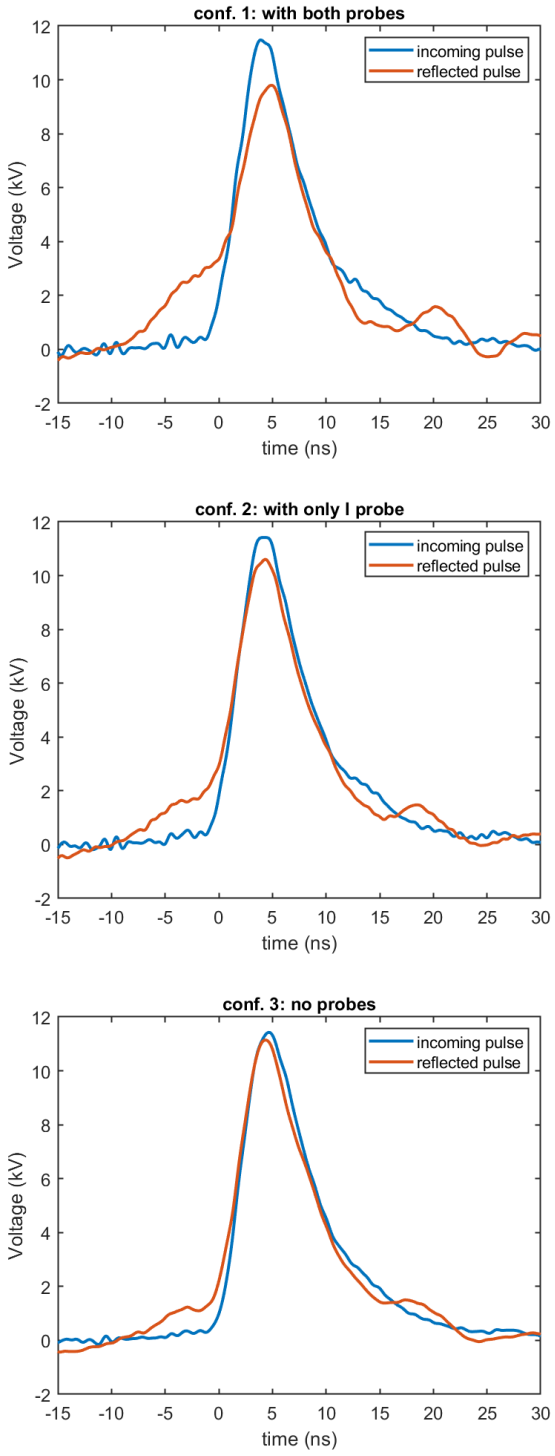

Figure 3.13: Comparison of incoming and reflected pulse in the three configurations with discharge inhibition.

calculate the energy using the probes method (eq. 3.1). If the load is completely imaginary, the equation

$$I(t+\tau) = C\frac{dV}{dt} \tag{3.18}$$

must be valid. From the fit of I(t) and $\frac{dV}{dt}$, the values of τ=3.89±0.03 ns and C=6.4±0.1 pF have been obtained. This value of C is the total capacitance of the load, given by the reactor itself and the probes. The HV probe has a parasitic capacitance of ∼3 pF and contributes to almost 50% of the resulting C value. The current probe also contributes to the load capacitance, although to a lesser extent.

3.6 Deposited energy measurements

Finally, measurements of the discharge at atmospheric pressure, with a flow of 150 sccm of N_2 have been performed, again in the same three different configurations as the ones with freon.

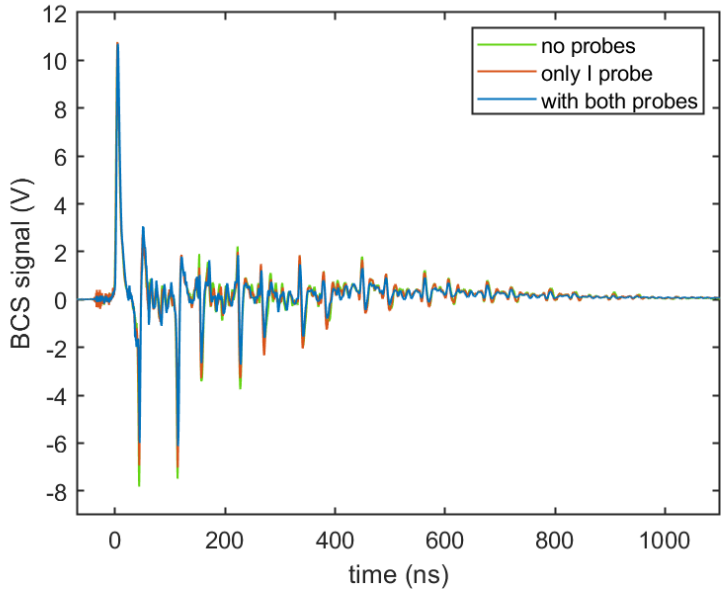

Figure 3.14: BCS signal with the discharge in the three different configurations.

Figure 3.14 shows the three BCS signals, while figure 3.15 is a zoom on the first pair of pulses. Again, while the first incoming pulse is always the same, from the first reflection it is evident the effect of a different load impedance. There is also a clear difference between the reflections in figure 3.15 and the ones in figure 3.12 of the measurements with discharge inhibition. While in fig. 3.12 the pulse is reflected almost completely with a very similar shape, in figure 3.15 there is a change of sign

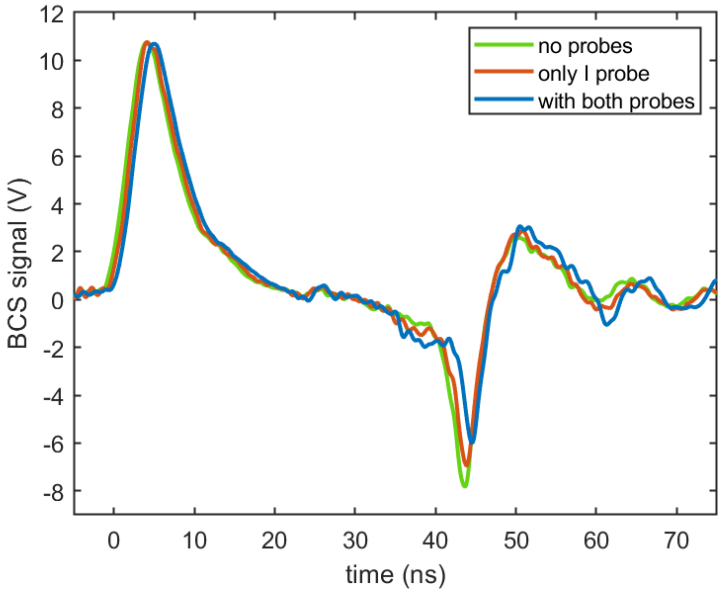

Figure 3.15: Zoom on the first pair of pulses

in the reflected pulse: it shows a sudden change in the load impedance, that rapidly goes from $\gg$ to $\ll$ than 75 Ω, corresponding to the discharge breakdown.

To calculate the energy from the BCS signal, it must be re-scaled taking into account the BCS attenuation and the BNC attenuators, and multiplied or divided by the cable attenuation k_c depending if the pulse is incident or reflected, respectively. Then the energy of each pulse in the transmission line is calculated from equation 3.10. Furthermore, the energy loss given by the factor R_F must be taken into account. We do it by dividing the energy of the reflected pulses by R_F. This corresponds to a larger reflected energy that would be measured in the ideal case of no losses apart from the energy deposited in the discharge. Finally, the deposited energy for each pair of pulses is obtained by subtracting the energy of the reflected pulse from the energy of the incident one. The procedure is summarized by the following equation:

$$\begin{aligned} E_{i,deposited} = \frac{1}{Z_{cable}} \int_{t_{iF}-a}^{t_{iF}+b} (V_{BCS,iF}(t) \cdot 10^{A/20} \cdot k_c)^2 dt + \\ - \frac{1}{R_F} \frac{1}{Z_{cable}} \int_{t_{iB}-a}^{t_{iB}+b} \left(\frac{V_{BCS,iB}(t) \cdot 10^{A/20}}{k_c} \right)^2 dt \end{aligned} \tag{3.19}$$

where

- the integration ranges are defined by the times corresponding to the maximum of a forward (t_{iF}) or backward t_{iB} peak in the BCS signal, respectively, and a=10 ns and b=20 ns, the range limits used for the integration;

- $A = A_{BCS} + A_{att}$ is the total attenuation in dB.

The voltage signal at the HV electrode can be reconstructed from the BCS signal by the sum of the incident and reflected pulses and it is shown in the three configurations in figure 3.16 together with the signal measured from the HV probe. The peak is higher for the configurations with lower capacitance at the load. The reconstructed HV signal from the BCS signal with both probes connected should in principle be the same as the one from the HV probe, since the measurements are simultaneous. However, the signal from the probe has a lower maximum value and shows the same effect described in [55] that overestimates the voltage in the falling edge during the breakdown.

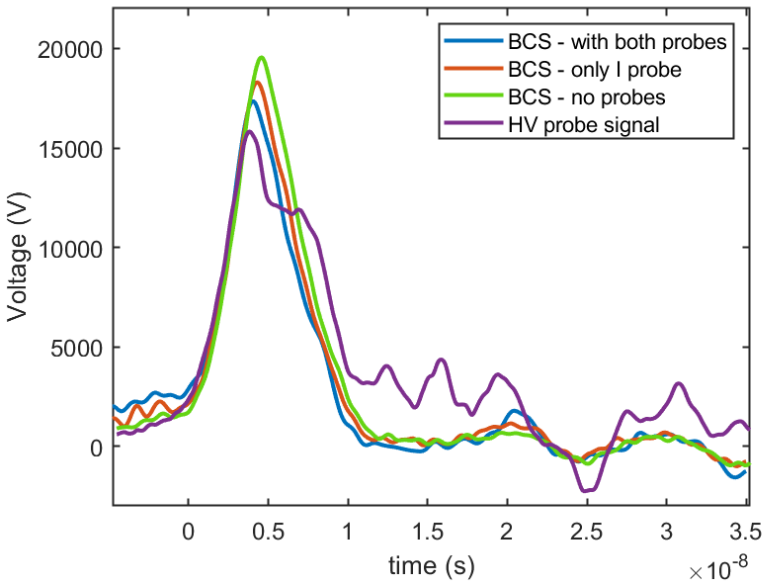

Figure 3.16: Comparison of reconstructed HV signals from the BCS measurements and signal from the HV probe.

Figure 3.17 shows signals from the HV and current probes acquired simultaneously with the BCS signal in configuration 1. From their product, the instantaneous power and the respective cumulative energy shown in figure 3.18 are obtained. The greatest amount of energy is deposited during the first pulse. It is important to remind that here each pulse corresponds to a pair of incident and reflected pulses in the BCS signal.

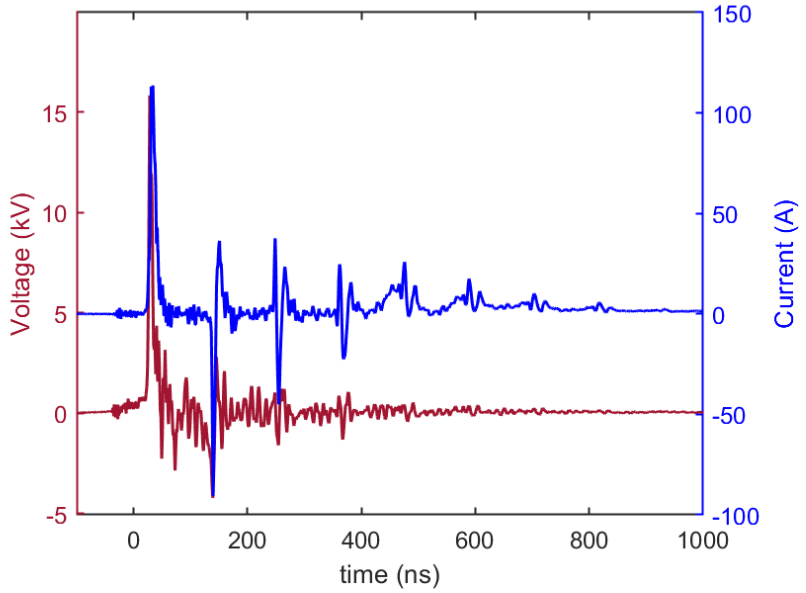

Figure 3.17: Signals from HV probe and current probe, acquired simultaneously.

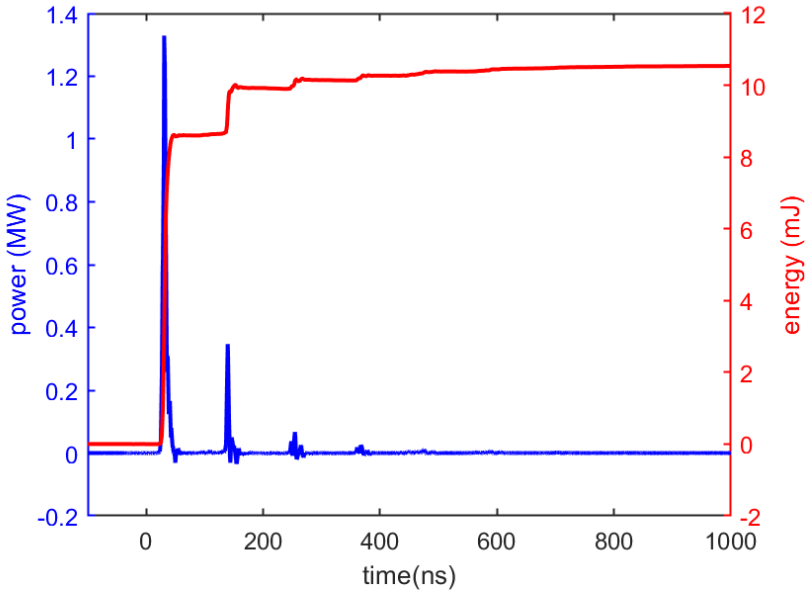

Figure 3.18: Power obtained from voltage and current signals and cumulative energy.

3.7 Results and discussion

The following table shows the energy deposited by each pulse that reaches the plasma reactor, i.e. each pulse from the probes and each couple of pulses from the BCS signals, in each configuration. We stop at the 3rd pulse because, after that, signals from different reflections start to overlap and, anyway, their contribution to the deposited energy is much smaller (as can be seen from figure 3.18) and it is comparable to the statistical error.

Pulse #	Probes	BCS (conf. 1)	BCS (conf. 2)	BCS (conf. 3)
1	8.6±0.3 mJ	6.1±0.1 mJ	5.9±0.1 mJ	5.6±0.1 mJ
2	1.3±0.15 mJ	1.2±0.2 mJ	1.32±0.12 mJ	1.48±0.09 mJ
3	0.2±0.07 mJ	0.23±0.07 mJ	0.26±0.06 mJ	0.46±0.08 mJ
Tot.	10.1±0.5 mJ	7.5±0.4 mJ	7.5±0.3 mJ	7.5±0.3 mJ

The different measurements with the BCS method provide quite similar energy results, suggesting that the assumptions made to take into account the losses are reasonable. They are also compatible with the values of energy from the probes for the 2nd and 3rd reflections. On the other hand, the energy calculated with probes for the first pulse is much higher than the values obtained with BCS, due to overestimation of the voltage during the first breakdown. The fact that the energy of the reflected pulses is not affected by the low bandwidth of the HV probe could be explained by the broadening of the pulse due to the cable attenuation. The total deposited energy (up to the 3rd reflection) is then overestimated by the probes measurement of $\sim 36\%$. This overestimation is even higher than the one estimated by Khomenko et al. of 25% [55].

It is important to point out that the behaviour of this kind of discharge is quite unpredictable and poorly reproducible: two discharges triggered and acquired in the same conditions could behave differently and their signals could have different properties, e.g. completely different shapes of the reflections depending on when the breakdown occurs. For this reason, each single sample used for these calculations has been checked to ensure that the behaviour of the discharge was the same. As can be seen in figures 3.11 and 3.14, the difference in the BCS signals among the different configurations is almost entirely in the amplitude of some reflections, meaning that the behaviour of the discharge was similar. Nevertheless, if we compare the energy calculated with the BCS when the probes were not connected and the energy calculated with the probes, we must remind that they are not measuring the same discharge. On the one hand, it helps to check what is the effect of the presence of the probes on the system. On the other hand, we can state that small differences in the calculation of the dissipated energy between the different BCS configurations can be mainly due to fluctuations in the behaviour of the discharge and are not relevant.

3.8 Conclusions

We can now safely state that the calculation of the energy deposited in our nanosecond pulsed discharges using HV probes Tektronic P6015A is not accurate, but it is significantly overestimated with respect to the one measured by means of the BCS technique (∼36% higher). This is due to a different dissipated energy in the system, probably due to the connection of the HV probe itself to the load, which becomes a non-negligible part of the load modifying the resulting impedance. This overestimation of the energy deposited in the plasma is translated into a remarkable underestimation of the processes efficiency. This means that the stated efficiencies in the works of our group, e.g. [29, 30], would actually be even higher.

While the BCS technique represents a potential alternative to probe measurements, its implementation with Megaimpulse NP generators is currently limited by the unavailability of electrical components necessary for developing fully and safely compatible cables.

However, one should carefully evaluate the practical convenience of a systematic use of this technique for deposited energy calculation in plasma processing. On one hand, these custom made device are more accurate and much cheaper than commercial probes. On the other hand, it forces to use long transmission lines between the HV source and the reactor, introducing an attenuation in the signal, that can be crucial for this type of plasma, and the issue of the management of this long HV cable in the experimental setup. As an example, the cable attenuation is detrimental if we are interested in the engineering of a system and in the all-around efficiency of a process, i.e. not considering only the efficiency of the plasma process but also the efficiency at the generator or at the wall-plug. Furthermore, the post processing analysis is more complicated than the one with I and V probes and it does not allow an instantaneous visualization at the oscilloscope of the whole current and voltage signals at the load with all their reflections, losing important information on the electrical characterization of the discharge.

Therefore, the BCS technique could be useful in the case we are studying a plasma process whose efficiency must be compared with other works and the 30% error in estimation of the deposited energy is not acceptable. Otherwise, if this accuracy is not strictly necessary, it can be more convenient and practical to use the commercial probes, keeping in mind that the calculated deposited energy will be overestimated, leading to an underestimation of the efficiency, and therefore of the performances of the process.

Chapter 4

Conclusions and outlooks

This thesis explores two topics focused on enhancing our understanding of Nanosecond Repetitive Pulse (NRP) discharges for CO_2 valorization and improving the overall efficiency of the process.

The research on adding ethylene to CO_2 discharge effluent arise from the established issue that back reactions limit CO_2 dissociation in the plasma. Various methods have been investigated to reduce recombination of carbon monoxide to carbon dioxide. These approaches primarily involve rapidly cooling the plasma in the afterglow or capturing oxygen before it can recombine with CO. However, it is essential to recognize that atomic oxygen is a highly reactive and energetic radical that can be utilized instead of dismissed as an undesirable by-product.

This study has investigated novel ways to harness reactive oxygen species, potentially turning a limitation into an opportunity for improved process efficiency. By doing so, we aim to mitigate the challenges posed by back reactions and open new routes for CO_2 valorization techniques. Xu et al. [56] enhanced CO_2 conversion in a RF plasma jet by simultaneous epoxidation of alkenes using the atomic oxigen produced in the discharge.

We use the same approach for our NRP discharge in CO_2 by introducing C_2H_4 immediately after the discharge. This might allows C_2H_4 to interact with the plasma reactive products without being present in the plasma. The epoxidation of ethylene potentially yields ethylene oxide (C_2H_4O), a valuable chemical widely used in countless applications, from plastics synthesis to healthcare.

Ethylene has been added post-discharge at various distances to map the lifetime of the radicals generated by the plasma. Despite several attempts to optimize the ethylene injection in the post-discharge region, ethylene oxide has not been detected. However, intriguing results have been found regarding the effect of C_2H_4 addition on CO_2 conversion. When ethylene is added closer to the discharge, the conversion of CO_2 significantly increases compared to the benchmark scenario where only CO_2 is used. However, as the distance from the reactor increases, the conversion decreases to levels lower than the reference. Eventually, when ethylene

is added at a sufficient distance that no longer influences the CO_2 dissociation processes, the conversion returns to the benchmark values.

To determine whether the observed effects result from ethylene contamination in the discharge zone, optical emission spectroscopy has been used to detect the presence of the Hα line, since hydrogen can only originate from C_2H_4. The spectra showed that traces of hydrogen are consistently present in the plasma, even in the most distant ethylene addition configurations. One possibility is that the shock wave generated by the nanosecond discharge overcomes the pressure gradients caused by the reactant flow, leading to gas mixing between the discharge and post-discharge zone. This phenomenon blurs the boundary between the inside and outside of the discharge reactor. This observation has important implications for understanding fluid dynamics and reactor design in NRP discharge systems.

A set of measurements was conducted with ethylene added directly to the reactor in a mixed feed with CO_2, varying the C_2H_4 flow up to 10% of the CO_2 flow. The results indicate behaviours similar to those observed when ethylene is applied at various distances post-discharge.

Baratte et al. [68] have found a similar result for a glow discharge in CO_2 and CH_4, where they varied the initial mixing ratio between the two species. They found that the fraction of CO_2 in the discharge outflow peaks at a specific initial mixture ratio of CO_2 to CH_4, where the dissociation is less effective. Through modelling, they attributed this phenomenon to a higher rate of the back reaction

$$CO + OH \rightarrow CO_2 + H \tag{4.1}$$

for that particular reactant mixture. If a similar occurrence is possible in our case, it should be investigated in future studies by means of spectroscopy experiments and modeling.

The work on back current shunts (BCS) has confirmed the significant limitations in the conventional method of measuring energy deposition in NRP discharges using the commercially available high-voltage probes, which substantially overestimates the energy compared to measurements obtained through the BCS method. While the BCS technique offers a promising alternative, using significantly lower-cost components compared to commercial probes, its implementation faces challenges, and the practical application in plasma processing requires careful consideration. This technique necessitates long transmission lines between the high-voltage source and the reactor, leading to signal attenuation that can negatively impact the overall efficiency of the process. Additionally, this technique involves a more complex post-processing analysis than HV and I probes and cannot visualize current and voltage signals at the load in real-time. We chose not to use the BCS technique for the measurements involving ethylene addition. This decision was made because the SEI remained constant. Additionally, since this is an initial investigation, obtaining an exact efficiency parameter for comparing the results with others was not necessary.

Further development of this technique can focus on optimizing the balance between measurement accuracy and signal attenuation across cable length.

Appendix A

Selectivity graphs

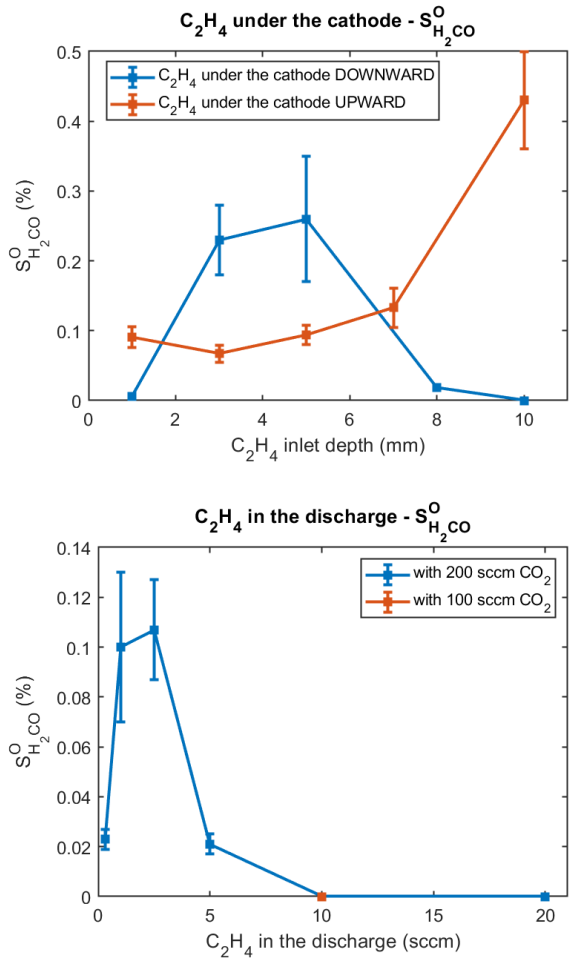

Figure A.1: $S^{O}_{H_2CO}$ in the different ethylene addition configurations.

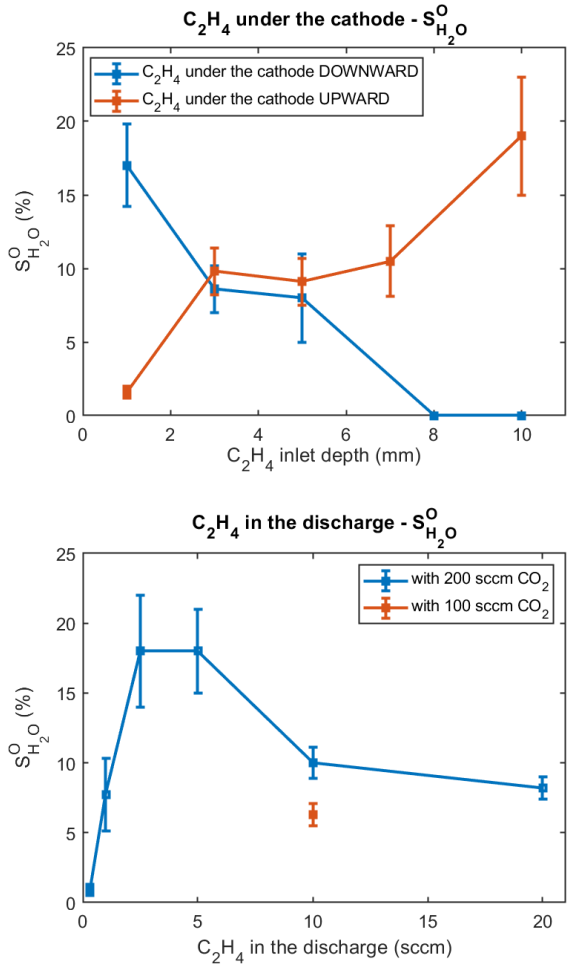

Figure A.2: $S^{O}_{H_2O}$ in the different ethylene addition configurations.

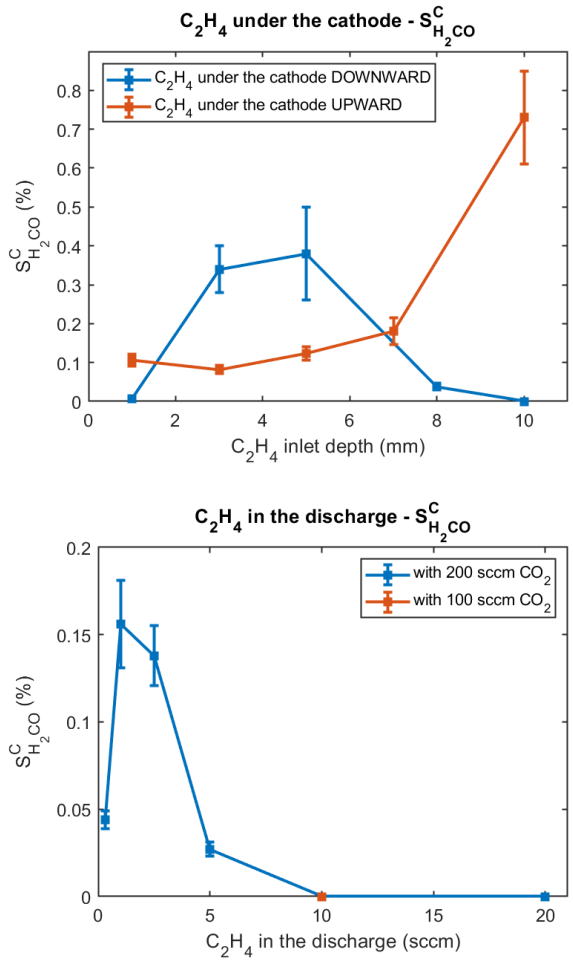

Figure A.3: $S^{C}_{H_2CO}$ in the different ethylene addition configurations.

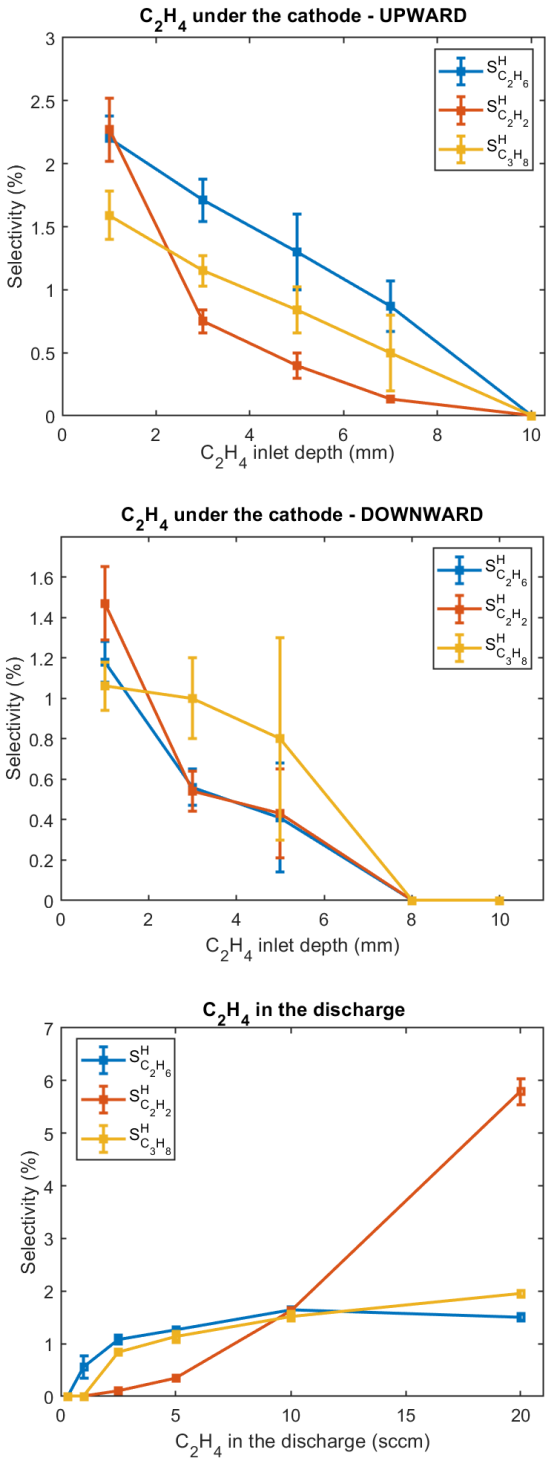

Figure A.4: Selectivities of H on C_2H_6, C_2H_2 and C_3H_8 in the different ethylene addition configurations.

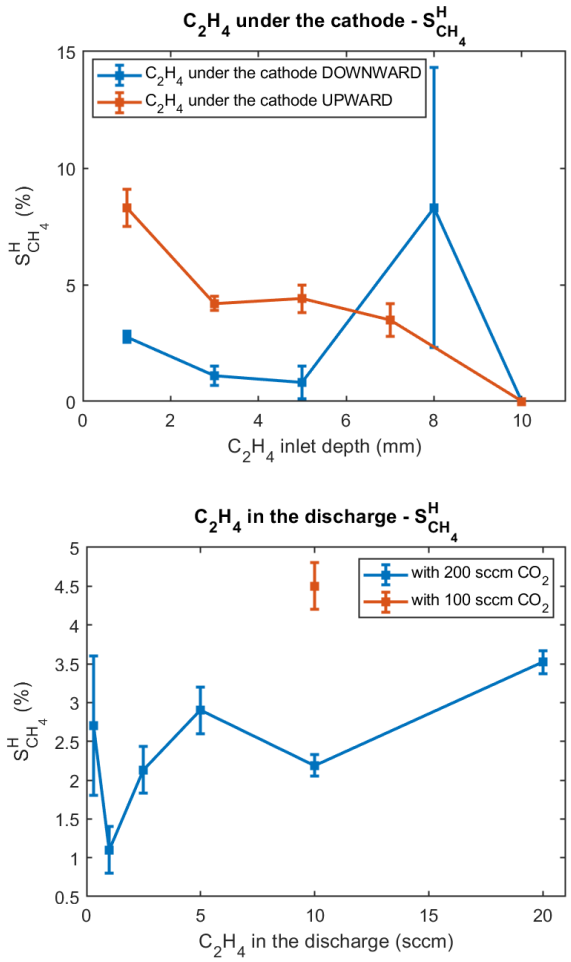

Figure A.5: $S^{H}_{CH_4}$ in the different ethylene addition configurations.

Bibliography

[1] https://climate.nasa.gov/vital-signs/carbon-dioxide/?intent=121

[2] Edenhofer O., Pichs-Madruga R., Sokona Y., Farahani E., Kadner S., Seyboth K., Adler A., Baum I., Brunner S., Eickemeier P., Kriemann, B. Savolainen J., Schlömer S., von Stechow C., Zwickel T. and Minx J.C., "IPCC2014: Climate Change 2014: Mitigation of Climate Change. Contribution of Working Group III to the Fifth Assessment Report of the Intergovernmental Panel on Climate Change," tech. rep., Cambridge University Press, Cambridge, United Kingdom and New York, NY, USA, 2014.

[3] https://skepticalscience.com/co2-residence-time.htm

[4] R. L. Jaffe and W. Taylor, "The Physics of Energy", 2018.

[5] Energy Institute, Statistical Review of World Energy, 2024.

[6] G. A. Olah, G. K. S. Prakash, and A. Goeppert, "Anthropogenic Chemical Carbon Cycle for a Sustainable Future", Journal of The American Chemical Society, vol. 133, pp. 12881–12898, 2011.

[7] https://www.carbonrecycling.is/, "Carbon Recycling International"

[8] F. Taccogna and G. Dilecce, "Non-equilibrium in low-temperature plasmas", The European Physical Journal D70 (2016). DOI:10.1140/epjd/e2016-70474-0

[9] Ramses Snoeckx and Annemie Bogaerts, "Plasma technology – a novel solution for CO_2 conversion?", Chem. Soc. Rev., 2017, 46, 5805, DOI: 10.1039/c6cs00066e

[10] O. Biondo, C. Fromentin, T. Silva, V. Guerra, G. van Rooij and A. Bogaerts, "Insights into the limitations to vibrational excitation of CO_2: validation of a kinetic model with pulsed glow discharge experiments", Plasma Sources Sci. Technol. 31 (2022) 074003, https://doi.org/10.1088/1361-6595/ac8019.

[11] A. Berthelot and A. Bogaerts, "Modeling of CO_2 Splitting in a Microwave Plasma: How to Improve the Conversion and Energy Efficiency", The Journal of Physical Chemistry C 2017 121 (15), 8236-8251, DOI: 10.1021/acs.jpcc.6b12840

[12] S. Paulussen, B. Verheyde, X. Tu, C. D. Bie, T. Martens, D. Petrovic, A. Bogaerts, and B. Sels. "Conversion of carbon dioxide to value-added chemicals in atmospheric pressure dielectric barrier discharges". In: Plasma Sources Science and Technology 19 (2010), p. 034015. issn: 0963-0252. doi: 10.1088/0963-0252/19/3/034015.

[13] A. Ozkan, A. Bogaerts, and F. Reniers. "Routes to increase the conversion and the energy efficiency in the splitting of CO_2 by a dielectric barrier discharge". In: Journal of Physics D: Applied Physics 50 (2017), p. 084004. issn: 0022-3727. doi: 10 . 1088 / 1361 - 6463/aa562c.

[14] T. Silva, N. Britun, T. Godfroid, and R. Snyders. "Optical characterization of a microwave pulsed discharge used for dissociation of CO_2". In: Plasma Sources Science and Technology 23 (2014), p. 025009. issn: 0963-0252. doi: 10.1088/0963-0252/23/2/025009.

[15] G. J. van Rooij, D. C. M. van den Bekerom, N. den Harder, T. Minea, G. Berden, W. A. Bongers, R. Engeln, M. F. Graswinckel, E. Zoethout, and M. C. M. van de Sanden. "Taming microwave plasma to beat thermodynamics in CO_2 dissociation". In: Faraday Discussions 183 (2015), pp. 233–248. issn: 1359-6640. doi: 10.1039/c5fd00045a.

[16] A. Indarto, D. R. Yang, J.-W. Choi, H. Lee, and H. K. Song. "Gliding arc plasma processing of CO_2 conversion". In: Journal of Hazardous Materials 146 (2007), pp. 309–315. issn: 0304-3894. doi: 10.1016/j.jhazmat.2006.12.023.

[17] M. Ramakers, J. A. Medrano, G. Trenchev, F. Gallucci, and A. Bogaerts. "Revealing the arc dynamics in a gliding arc plasmatron: a better insight to improve CO_2 conversion". In: Plasma Sources Science and Technology 26 (2017), p. 125002. issn: 1361-6595. doi: 10.1088/1361-6595/aa9531.

[18] L. F. Spencer and A. D. Gallimore. "Efficiency of CO_2 Dissociation in a Radio-Frequency Discharge". In: Plasma Chemistry and Plasma Processing 31 (2011), pp. 79–89. issn: 0272-4324. doi: 10.1007/s11090-010-9273-0.

[19] M. S. Moss, K. Yanallah, R. W. K. Allen, and F. Pontiga. "An investigation of CO_2 splitting using nanosecond pulsed corona discharge: effect of argon addition on CO_2 conversion and energy efficiency". In: Plasma Sources Science and Technology 26 (2017), p. 035009. issn: 1361-6595. doi: 10.1088/1361-6595/aa5b1d.

[20] M. Budde, L. M. Martini, M. Ceppelli, S. Quercetti, and R. Engeln. "Absolute OH density measurements in a CO_2–H_2O glow discharge by laser-induced fluorescence spectroscopy". In: Plasma Sources Science and Technology 31.5 (2022), p. 055002. doi: 10.1088/1361-6595/ac5ecc.

[21] Y. Du, T. V. Tsankov, D. Luggenhölscher, and U. Czarnetzki, "Time evolution of CO_2 ro-vibrational excitation in a nanosecond discharge measured with laser absorption spectroscopy", In: Journal of Applied Physics 54 365201 (2021), doi:10.1088/1361-6463/ac03e7

[22] G. Dilecce, L. M. Martini, P. Tosi, M. Scotoni and S. De Benedictis, "Laser induced fluorescence in atmospheric pressure discharges", Plasma Sources Sci. Technol. 24 (2015) 034007, doi:10.1088/0963-0252/24/3/034007.

[23] L. M. Martini, N. Gatti, G. Dilecce, M. Scotoni, and P. Tosi, "Laser induced fluorescence in nanosecond repetitively pulsed discharges for CO_2 conversion", Plasma Phys. Control. Fusion 60 (2018) 014016, https://doi.org/10.1088/1361-6587/aa8bed

[24] L. M. Martini, S. Lovascio, G. Dilecce, and P. Tosi, "Time-Resolved CO_2 Dissociation in a Nanosecond Pulsed Discharge", Plasma Chem Plasma Process (2018) 38:707–718, https://doi.org/10.1007/s11090-018-9893-3

[25] S. Heijkers, L. M. Martini, G. Dilecce, P. Tosi and A. Bogaerts, "Nanosecond Pulsed Discharge for CO_2 Conversion: Kinetic Modeling To Elucidate the Chemistry and Improve the Performance", J. Phys. Chem. C 2019, 123, 12104–12116, DOI: 10.1021/acs.jpcc.9b01543

[26] S. Tao, S. Guangsheng, Y. Ping, W. Jue, Y. Weiqun, S. Yaohong, and Z. Shichang, "An experimental investigation of repetitive nanosecond-pulse breakdown in air", J. Phys. D: Appl. Phys. 39 (2006) 2192–2197, doi:10.1088/0022-3727/39/10/030

[27] Z. Zhao and J. Li, "Repetitively pulsed gas discharges: memory effect and discharge mode transition", High Volt., 2020, Vol. 5 Iss. 5, pp. 569-582

[28] T. Huiskamp, "Nanosecond pulsed streamer discharges Part I: Generation, source-plasma interaction and energy-efficiency optimization", Plasma Sources Sci. Technol. 29 (2020) 023002 (47pp), https://doi.org/10.1088/1361-6595/ab53c5

[29] C. Montesano, S. Quercetti, L.M. Martini, G. Dilecce., and P. Tosi, "The effect of different pulse patterns on the plasma reduction of CO_2 for a nanosecond discharge". Journal of CO_2 Utilization 39, 101157 (2020), https://doi.org/10.1016/j.jcou.2020.101157

[30] C. Montesano, M. Faedda., L.M. Martini, G. Dilecce, and P. Tosi, "CH4 reforming with CO_2 in a nanosecond pulsed discharge. The importance of the pulse sequence". Journal of CO_2 Utilization 49, 101556 (2021), https://doi.org/10.1016/j.jcou.2021.101556

[31] L. M. Martini, G. Dilecce, P. Tosi, "Chapter 1: Non-equilibrium Plasmas in Gases at Atmospheric Pressure", Plasma Applications in Gases, Liquids and Solids, pp. 1-55 (2023) https://doi.org/10.1142/9789811275937_0001

[32] M. Ceppelli, T.P.W. Salden, L.M. Martini, G. Dilecce, and P. Tosi, "Time-resolved optical emission spectroscopy in CO_2 nanosecond pulsed discharges", Plasma Sources Sci. Technol. 30 (2021) 115010 (15pp), https://doi.org/10.1088/1361-6595/ac2411

[33] C. Montesano, T.P.W. Salden, L.M. Martini, G. Dilecce, and P. Tosi, "CO_2 Reduction by Nanosecond-Plasma Discharges: Revealing the Dissociation's Time Scale and the Importance of Pulse Sequence", J. Phys. Chem. C 2023, 127, 10045-10050, https://doi.org/10.1021/acs.jpcc.3c02547

[34] A. Post, M. Budde, S.C.L. Vervloedt, R. Engeln, and T. Huiskamp, "Nanosecond repetitively pulsed plasmas with MHz bursts for CO_2 dissociation", J. Phys. D: Appl. Phys. 57 (2024) 305203 (16pp), https://doi.org/10.1088/1361-6463/ad40bc

[35] C. Richards , E. Jans , D. Mignogna, and I.V. Adamovich, "Time-resolved CO_2, CO, and N2 vibrational population measurements in Ns pulse discharge plasmas", Plasma Sources Sci. Technol. 31 (2022) 094011 (14pp), https://doi.org/10.1088/1361-6595/ac8f6d

[36] M.S. Bak, S.K. Im, and M. Cappelli, "Nanosecond-Pulsed Discharge Plasma Splitting of Carbon Dioxide", IEEE TRANSACTIONS ON PLASMA SCIENCE, VOL. 43, NO. 4, APRIL 2015.

[37] T. Yong, H. Zhong, E. Pannier, C. Laux, and M.A. Cappelli, "High-pressure CO_2 dissociation with nanosecond pulsed discharges", Plasma Sources Sci. Technol. 32 (2023) 115012 (17pp), https://doi.org/10.1088/1361-6595/ad066e

[38] A.S. Morillo-Candas, C. Drag, J-P Booth, T.C. Dias, V. Guerra, and O. Guaitella, "Oxygen atom kinetics in CO_2 plasmas ignited in a DC glow discharge", Plasma Sources Sci. Technol. 28 (2019) 075010 (21pp), https://doi.org/10.1088/1361-6595/ab2b84

[39] A.S Morillo-Candas, B.L.M. Klarenaar, C. Amoedo, V. Guerra, and O. Guaitella, "Effect of oxygen atoms on the vibrational kinetics of CO_2 and CO revealed by the use of a large surface area material", J. Phys. D: Appl. Phys. 54 (2021) 095208 (18pp), https://doi.org/10.1088/1361-6463/abc992

[40] A.F. Silva, A.S. Morillo-Candás, A. Tejero-del-Caz, L.L. Alves, V. Guerra, and O. Guaitella, "A reaction mechanism for vibrationally-cold low-pressure CO_2 plasmas", Plasma Sources Sci. Technol. 29 (2021) 125020 (16pp) https://doi.org/10.1088/1361-6595/abc818

[41] T. Silva, A.S. Morillo-Candás, V. Guerra, and O. Guaitella, "Modeling the time evolution of the dissociation fraction in low-pressure CO_2 plasmas", Journal of CO_2 Utilization 53 (2021) 101719, https://doi.org/10.1016/j.jcou.2021.101719

[42] C. Fromentin, T. Silva, T.C. Dias, A.S. Morillo-Candas, O. Biondo, O. Guaitella, and V. Guerra, "Study of vibrational kinetics of CO_2 and CO in CO_2–O_2 plasmas under non-equilibrium conditions", Plasma Sources Sci. Technol. 32 (2023) 024001 (26pp), https://doi.org/10.1088/1361-6595/acb665

[43] L.D. Pietanza, G. Colonna, and M. Capitelli, "Self-Consistent State-to-State Kinetic Modeling of CO_2 Cold Plasmas: Insights on the Role of Electronically Excited States", Plasma Chemistry and Plasma Processing (2024) 44:1431–1468, https://doi.org/10.1007/s11090-023-10407-x

[44] A.S. Morillo-Candas, V. Guerra, and O. Guitella, "Time Evolution of the Dissociation Fraction in rf CO_2 Plasmas: Impact and Nature of Back-Reaction Mechanisms", J. Phys. Chem. C 2020, 124, 17459-17475, https://dx.doi.org/10.1021/acs.jpcc.0c03354

[45] L.D. Pietanza, G. Colonna, and M. Capitelli, "Activation of vibrational-induced CO_2 dissociation in cold non-equilibrium plasma", Plasma Phys. Control. Fusion 65 (2023) 044004 (10pp), https://doi.org/10.1088/1361-6587/acb843

[46] S. Heijkers, L. M. Martini, G. Dilecce, P. Tosi and A. Bogaerts, "Supporting Information: Nanosecond Pulsed Discharge for CO_2 Conversion: Kinetic Modelling to Elucidate the Chemistry and Improve the Performance"

[47] A. Hecimovic, F.A. D'Isa, E. Carbone, and U. Fantz, "Enhancement of CO_2 conversion in microwave plasmas using a nozzle in the effluent", Journal of CO_2 Utilization 57 (2022) 101870, https://doi.org/10.1016/j.jcou.2021.101870

[48] S.V. Alphen, A. Hecimovic, C.K. Kiefer, U. Fantz, R. Snyders, and A. Bogaerts, "Modelling post-plasma quenching nozzles for improving the performance of CO_2 microwave plasmas", Chemical Engineering Journal 462 (2023) 142217, https://doi.org/10.1016/j.cej.2023.142217

[49] K. Wang, S. Ceulemans, H. Zhang, I. Tsonev, Y. Zhang, Y. Long, M. Fang, X. Li, J. Yan, and A. Bogaerts, "Inhibiting recombination to improve the performance of plasma-based CO_2 conversion", Chemical Engineering Journal 481 (2024) 148684, https://doi.org/10.1016/j.cej.2024.148684

[50] S. Mori and L.L. Tun, "Synergistic CO_2 conversion by hybridization of dielectric barrier discharge and solid oxide electrolyser cell", Plasma Process Polym. 2017;14: e1600153. https://doi.org/10.1002/ppap.201600153

[51] G. Chen, F. Buck, I. Kistner, M. Widenmeyer, T. Schiestel, A. Schulz, M. Walker, and A. Weidenkaff, "A novel plasma-assisted hollow fiber membrane concept for efficiently separating oxygen from CO in a CO_2 plasma", Chemical Engineering Journal 392 (2020) 123699, https://doi.org/10.1016/j.cej.2019.123699

[52] R. Antunes, K. Wiegers, A. Hecimovic, C.K. Kiefer, S. Buchberger, A. Meindl, T. Schiestel, A. Schulz, M. Walker, and U. Fantz, "Proof of Concept for O2 Removal with Multiple LCCF Membranes Accommodated in the Effluent of a CO_2 Plasma Torch", ACS Sustainable Chem. Eng. 2023, 11, 15984-15993, https://doi.org/10.1021/acssuschemeng.3c04862

[53] E. Delikonstantis, M. Scapinello, V. Singh, H. Poelman, C. Montesano, L.M. Martini, P. Tosi, G.B. Marin, K.M. Van Geem, V.V. Galvita, and G.D. Stefanidis, "Exceeding Equilibrium CO_2 Conversion by Plasma-Assisted Chemical Looping", ACS Energy Lett. 2022, 7, 1896-1902, https://doi.org/10.1021/acsenergylett.2c00632

[54] F.G. Girard-Sahun, O. Biondo, G. Trenchev, G. van Rooij, and A. Bogaerts, "Carbon bed post-plasma to enhance the CO_2 conversion and remove O2 from the product stream", Chemical Engineering Journal 442 (2022) 136268, https://doi.org/10.1016/j.cej.2022.136268

[55] Khomenko A., Podolsky V. and Wang X., "Different approaches of measuring high-voltage nanosecond pulses and power delivery in plasma systems", Electr Eng 103, 57–66 (2021). https://doi.org/10.1007/s00202-020-01058-8

[56] H. Xu, M. Shaban, S. Wang, A. Alkayal, D. Liu, M. G. Kong, F. Plasser, B. R. Buckley and F. Iza, "Oxygen harvesting from carbon dioxide: simultaneous epoxidation and CO formation", Chem. Sci., 2021,12, 13373-13378, https://doi.org/10.1039/D1SC04209B

[57] J. Gorzynski Smith," Synthetically Useful Reactions of Epoxides. Synthesis", 1984(8), 629–656. doi:10.1055/s-1984-30921

[58] Q. H. Xia, H. Q. Ge, C. P. Ye Z. M. Liu, K.-X. Su, "Advances in Homogeneous and Heterogeneous Catalytic Asymmetric Epoxidation", Chem. Rev. 2005, 105, 5, 1603–1662, https://doi.org/10.1021/cr0406458

[59] S. Rebsdat and D. Mayer, "Ethylene Oxide", In Ullmann's Encyclopedia of Industrial Chemistry. Weinheim, Germany: Wiley-VCH Verlag GmbH & Co. KGaA. DOI: 10.1002/14356007.a10_117

[60] Aresta M., Karimi I., Kawi S., "An Economy Based on Carbon Dioxide and Water", Springer (2019).

[61] S. Chavadej, A. Tansuwan, and T. Sreethawong, "Ethylene Epoxidation over Alumina-Supported Silver Catalysts in Low-Temperature AC Corona Discharge", Plasma Chem Plasma Process (2008) 28:643–662, DOI 10.1007/s11090-008-9150-2

[62] T. Sreethawong,T. Suwannabart, and S. Chavadej, "Ethylene Epoxidation in Low-Temperature AC Dielectric Barrier Discharge: Effects of Oxygen-to-Ethylene Feed Molar Ratio and Operating Parameters", Plasma Chem Plasma Process (2008) 28:629–642, DOI 10.1007/s11090-008-9149-8

[63] T. Suttikul, C. Tongurai, H. Sekiguchi and S. Chavadej, "Ethylene Epoxidation in Cylindrical Dielectric Barrier Discharge: Effects of Separate Ethylene/Oxygen Feed", Plasma Chem Plasma Process (2012) 32:1169–1188, DOI 10.1007/s11090-012-9398-4

[64] T. Suttikul, S. Yaowapong-aree, H. Sekiguchi, S. Chavadej, J. Chavadej, "Improvement of ethylene epoxidation in low-temperature corona discharge by separate ethylene/oxygen feed", Chemical Engineering and Processing 70 (2013) 222– 232, http://dx.doi.org/10.1016/j.cep.2013.03.018

[65] T. Suttikul, S. Kodama, H. Sekiguchi and S. Chavadej, "Ethylene Epoxidation in an AC Dielectric Barrier Discharge Jet System", Plasma Chem Plasma Process (2014) 34:187–205, DOI 10.1007/s11090-013-9492-2

[66] T. Suttikul and S. Chavadej, "Ethylene Epoxidation in a Low-Temperature Parallel Plate Dielectric Barrier Discharge System: Effect of Oxygen Source", Ind. Eng. Chem. Res. 2017, 56, 12547-12555, DOI: 10.1021/acs.iecr.7b03469

[67] I. E. Gordon, L. S. Rothman, R. J. Hargreaves, R. Hashemi, E. V. Karlovets, F. M. Skinner, et al., "The HITRAN2020 molecular spectroscopic database", J. Quant. Spectrosc. Radiat. Transfer 277, 107949 (2022). doi: 10.1016/j.jqsrt.2021.107949

[68] E. Baratte, C. A. Garcia-Soto, T. Silva, V. Guerra, V. I. Parvulescu, and O. Guaitella, "CO_2/CH_4 glow discharge plasma. Part I: Experimental and numerical study of the reaction pathways", Plasma Chem Plasma Process 44, 1237–1286 (2024). https://doi.org/10.1007/s11090-023-10421-z

[69] T. Huiskamp, F. J. C. M. Beckers, E. J. M. van Heesch and A. J. M. Pemen, "B-Dot and D-Dot Sensors for (Sub)Nanosecond High-Voltage and High-Current Pulse Measurements", IEEE Sensors Journal, vol. 16, no. 10, pp. 3792-3801, May15, 2016, doi: 10.1109/JSEN.2016.2530841

[70] J. J. van Oorschot and T. Huiskamp, "Rogowski and D-Dot Sensors for Nanosecond High-Voltage and High-Current Pulse Measurements in Impedance-Matched Pulse Generators", IEEE Transactions

on Plasma Science, vol. 51, no. 4, pp. 1107-1116, April 2023, doi: 10.1109/TPS.2023.3259643.

[71] B. M. Novac, R. Xiao, T. Huiskamp, L. Pécastaing, M. Wang, P. Senior, A.ntoine S. de Ferron, A. J. M. Pemen, and M. Rivaletto, "Theoretical and Experimental Studies of Off-the-Shelf V-Dot Probes", IEEE Transactions on Plasma Science, vol. 46, no. 8, pp. 2985-2992, Aug. 2018, doi: 10.1109/TPS.2018.2854971

[72] Stepanyan SA, Starikovskiy AY, Popov NA, Starikovskaia SM, (2014) "A nanosecond surface dielectric barrier discharge in air at high pressures and different polarities of applied pulses: transition to filamentary mode", Plasma Sour Sci Technol 23(4):045003, DOI: 10.1088/0963-0252/23/4/045003

[73] C. Liu, A. Fridman and D. Dobrynin, "Uniformity analysis of nanosecond and sub-nanosecond pulsed DBD in atmospheric air", (2019) Plasma Res. Express 1 015007, DOI 10.1088/2516-1067/aaf067

[74] Grosse K, Held J, Kai M, von Keudell A (2019) Nanosecond plasmas in water: ignition, cavitation and plasma parameters. Plasma Sour Sci Technol 28(8):085003, DOI: 10.1088/1361-6595/ab26fc

[75] `https://www.test-and-measurement-world.com/Measurements/S-Parameter-measurements.html`

[76] Klochko A., 2014 Excited species chemistry in homogeneous nanosecond discharges with high specific energy deposition. Ph.D. thesis Ecole Polytechnique

[77] Lepikhin M. N., Fast energy relaxation in the afterglow of a nanosecond capillary discharge in nitrogen/oxygen mixtures. Ph.D. thesis Plasma Physics [physics.plasm-ph]. Université Paris Saclay (COmUE), 2017. English. NNT: 2017SACLX087. tel-01739847